Master Thesis Report

Numerical simulations for turbulent oil-water core-annular flow

Keval Ketanbhai Parikh

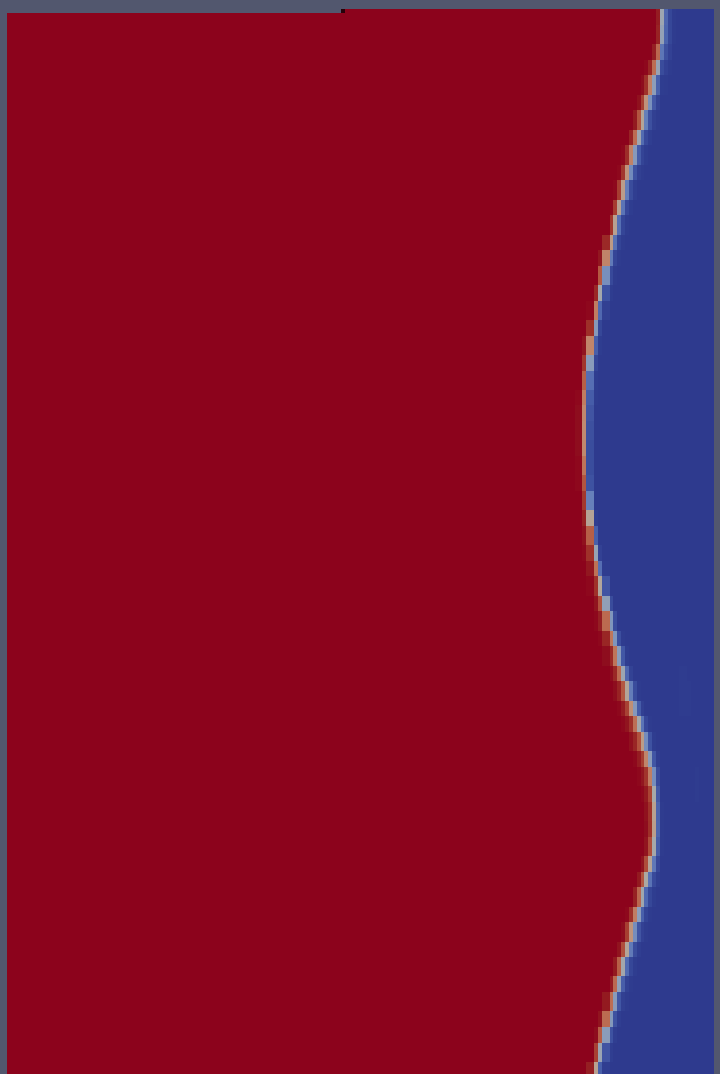

TU Delft

Numerical simulations for turbulent oil-water core-annular flow

by

Keval Ketanbhai Parikh
Student number: 4999614

in partial fulfillment of the requirements for the degree of

Master of Science
in Mechanical Engineering
Energy, Flow and Process Technology

at the Delft University of Technology,
to be defended publicly on Wednesday September 29, 2021 at 11:00 AM.

Supervisors:	Prof.dr.ir. R.A.W.M. Henkes Dr.ir. M.J.B.M. Pourquie
Committee:	Dr.ir. G.H. Keetels Prof.dr.ir. G. Ooms Haoyu Li

Faculty of Mechanical, Maritime and Materials Engineering (3mE)·Delft University of Technology

Acknowledgements

I have always been fascinated with fluid dynamics and I believe that mutiphase flow with turbulence is the pinnacle of flow physics. Hence, I am thankful that I got an opportunity to work in this field. It was an easy decision to study at TU Delft and it has not disappointed by providing me ample opportunities to learn about multiphase flows. Being excited about it, I started my journey of research with this thesis.

First of all I would like to thank my supervisor Prof.dr.ir. R.A.W.M. Henkes for his continued support and guidance throughout my thesis. He has kept me motivated to continue my work and his eye for detail has made sure that my work is of good quality. I would like to thank my co-supervisor Dr.ir. M.J.B.M. Pourquie for his help and support through the intricacies of my thesis. He has always patiently answered all of my questions. I would also like to thank Prof.dr.ir. G. Ooms and Haoyu Li for their inputs during the meetings. A special mention to Haoyu Li for her immediate help in solving the technical difficulties I faced during my simulations. I would also like to thank Dr.ir. G.H. Keetels for agreeing to be on my committee. Finally, I would like to thank the Delft university of technology in providing me with the opportunity and the resources to carry out my thesis.

I would like to thank my parents for always encouraging me to achieve my best. I would not have come this far without their support. I would like to express my gratitude to all my friends back in India who have listened to my rants about my thesis and also to all my friends in the Netherlands who are my family away from home. This would not have been possible without all of them.

Keval Ketanbhai Parikh
September 13, 2021

Abstract

The transportation of high viscosity oil is an ongoing research topic for quite some years because of its importance in industrial applications and the increasing energy requirements of the world population. The water lubricated oil core with a core-annular flow configuration is a viable option for the transport of high viscosity oil. It was observed that there are significant differences between the predictions from the RANS simulations and the experimental data for turbulent oil-water core-annular flow obtained in the flow loop in the lab at TU Delft. Thus, this study is performed to understand the difference between the RANS simulations and the experimental data. 1D and 2D OpenFOAM simulations for turbulent vertical core-annular flow are performed using the Launder-Sharma low-Re k-ε turbulence model. The pressure drop and the oil holdup are imposed while the total flow rate and the water-cut is obtained as the output from the simulations. The results from the OpenFOAM simulations are compared with the DNS data available in literature to understand the impact of the turbulence characteristics and the interfacial waves. Both 1D and 2D simulations were carried out. The 1D model does not include the interface waves. The 2D axisymmetric model is able to capture the travelling interface waves.

The 1D OpenFOAM simulations are carried out for five cases with different oil holdups and the results are compared with the asymptotic wall laws. It is concluded that the turbulence is sufficiently resolved by the 1D simulations. The 2D simulations are also performed for five different oil holdups. The 2D simulations are first validated by performing grid independence tests. The dependence of the simulation results on the streamwise domain length, presence of gravity and oil viscosity is also analysed. It was found that the streamwise domain length and the oil viscosity used does not have a significant influence on the prediction of the results. The comparison of the RANS simulations with the DNS data shows that the difference depends on the turbulence levels inside the simulation domain. The difference for the total flow rate between the 2D OpenFOAM simulations and the DNS data is found to be 10% for fully turbulent core-annular flow while the difference increases to 29% for core-annular flow with no turbulence. The friction factor for the 2D OpenFOAM simulations is found to be about 17% lower for fully turbulent flow while it is 39% lower than the DNS predictions for the simulation with no turbulence. The difference for the holdup ratio (when comparing 2D OpenFOAM simulations with respect to DNS) decreases first from 15% higher for the low oil holdup cases to 8% higher for simulation with oil holdup fraction 0.71 and then increases to 14% higher for the highest oil holdup case. It is also observed from the comparison of the mean streamwise velocities and the mean shear stresses that the turbulence level in the simulation domain impact the extent of the difference. The agreement in the wave characteristics between the 2D OpenFOAM simulations and the DNS data depends on the mixture of wavelengths present in the simulation domain. The RANS simulations predict a specific dominant wavelength while the DNS data gives a mixture of wavelengths for lower oil holdups. The dominance of a specific wavelength increases with increasing oil holdup for the DNS predictions.

Contents

1 Introduction

Nowadays there is an increasing focus on the development of renewable energy resources due to their environment friendliness and sustainability. But the scaling up of renewable resources to meet the overall energy requirements will take up considerable amount of time (decades). Thus, conventional fossil resources (like oil and gas) will continue to play a role in the energy mix in the next years, most likely with an increasing use of Carbon Capture and Storage (CCS). Oil is also expected to remain important as feed stock for the chemical industry (e.g. fabrication of plastics). On the longer term such products may also be generated fully synthetically, that is by converting water and CO_2 through electrical-chemical processes into hydrocarbon liquids and products.

The present Master Thesis focuses on the pipeline transport of a viscous liquid, like heavy oil. As the availability of light oil reservoirs will become less and less, the exploration of heavy oil reservoirs can be considered. The technology used for the production and transport of conventional (light) oils is not adequate or suitable for the production and transport of unconventional (heavy) oils. The major issue which arises when producing heavy oils is the larger pressure drop that occurs due to the oil flow. The pressure drop for flow in a pipe is directly proportional to the viscosity of the fluid and since the viscosity of heavy oils is significantly higher than that of conventional oils, the pumping cost is also higher. Thus, to reduce the pumping costs for the transport of high viscosity oils, different ideas need to be explored.

The lubricated transport of oil with water is considered a highly promising option for the transport of high viscosity oils. Joseph et al. [14] observed that, for a given pressure drop, this configuration transports oil at almost the same throughput as obtained during the flow of water alone and thus the pumping costs can be reduced to an economically viable level. As there are two phases present, oil and water, multiphase flow physics has to be applied. There are many different flow configurations that occur when two immiscible liquids flow together. The configuration of interest for the transport of heavy oil and for this thesis is known as core-annular flow. In this configuration, the low viscosity fluid, water, flows in the region of high shear which is along the wall, while the high viscosity fluid, oil, flows inside the core. This flow configuration is known as Perfect Core-Annular Flow (PCAF) if the interface between the oil and the water is smooth (i.e. no waves) and the oil core is concentric.

Joseph et al. [13] performed a linear stability analysis on a concentric interface between two fluids of different viscosities. They show that the interface is always unstable when the more viscous fluid is in the annulus while the interface can be stable when the more viscous fluid is in the core and the annulus is thin. Bai et al. [3] performed experiments for a vertical pipe to identify different flow regimes for oil-water flow. They classified the flow regimes into seven different types, namely: oil bubbles in water, slugs of oil in water, bamboo waves, corkscrew waves, disturbed core-annular flow, oil sticks to the wall and dispersions. The different flow patterns are shown in Figure 1.1. Their experiments show that it is difficult to obtain perfect core-annular flow in practice as there are waves present at the interface. These waves can grow in amplitude and the oil can stick to the wall which gives a larger pressure drop and also fouling, which is not desired. The experiments also suggest that there are certain flow conditions where the waves do not grow in amplitude and the core-annular flow is stable.

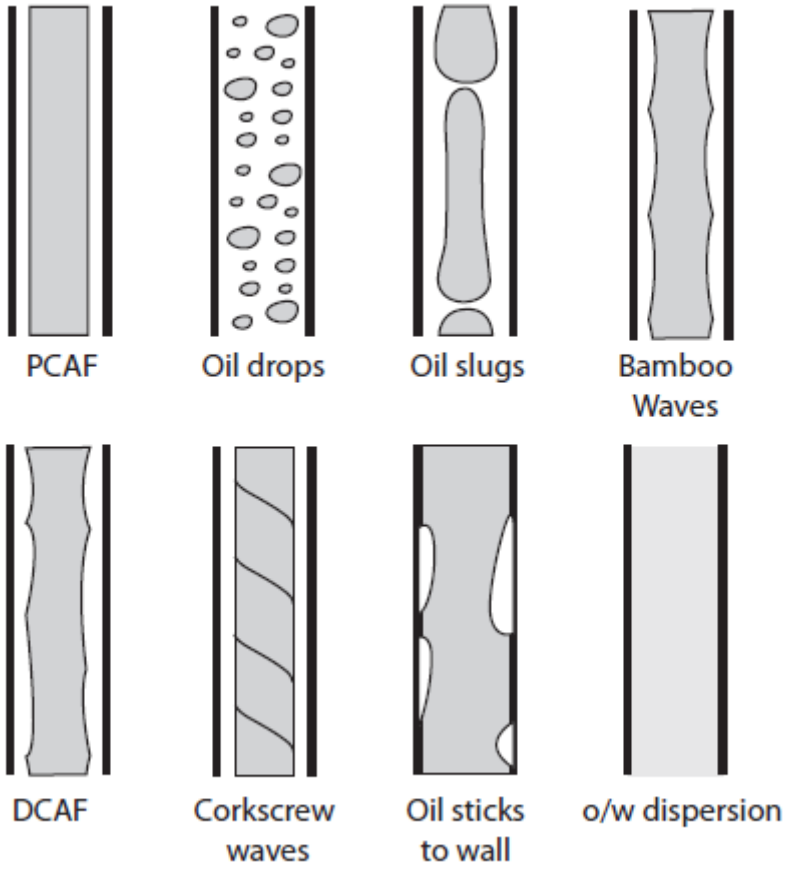

Figure 1.1: Different flow patterns observed in vertical oil-water flow. Figure taken from Beerens [5].

For core-annular flow in horizontal pipes, the density difference between the oil and the water plays an important role. Since the density of water is usually larger than the density of oil, the water tends to drop down due to gravity and there is an upward force on the oil core due to buoyancy. This could make the oil touch the surface of the pipe and then fouling occurs. But it has been observed that there is a downward force on the core due to the waves present at the interface which under certain conditions prevents the oil from touching the upper pipe wall but the core becomes eccentric instead of remaining concentric like in perfect core-annular flow. The throughput of core-annular flow with a wavy interface is lower than perfect core-annular flow but the presence of the waves is a necessary condition to ensure a stable core-annular flow arrangement in a horizontal pipe. There are two different theories which explain this phenomenon of downward force on the core as shown in Figure 1.2. Ooms et al. [23] explain this phenomenon with what they call the lubrication film model. They assumed the core to be solid since the oil is very viscous and hence the form of the interface does not change with time. They observed in the experiments that there was a ripple present at the interface so the core surface was assumed to be rippled in the shape of a sawtooth. They concluded that the downward force is the result of the pressure variations in the water film above the core during the flow and that the ripples are necessary for the downward counterbalancing force to be present. Joseph et al. [14] argued that the sawtooth waves are unstable and the waves should be smooth where they are sharp and steep where they are gentle. They mentioned that inertia is important to generate the counterbalancing force in this model, known as flying core model, as opposed to the lubricating film model where viscous forces dominate. Thus, the overall conclusion from both the theories was that there exists a downward counterbalancing force on the core which stabilises core-annular flow and that the waves at the interface indeed play an important role.

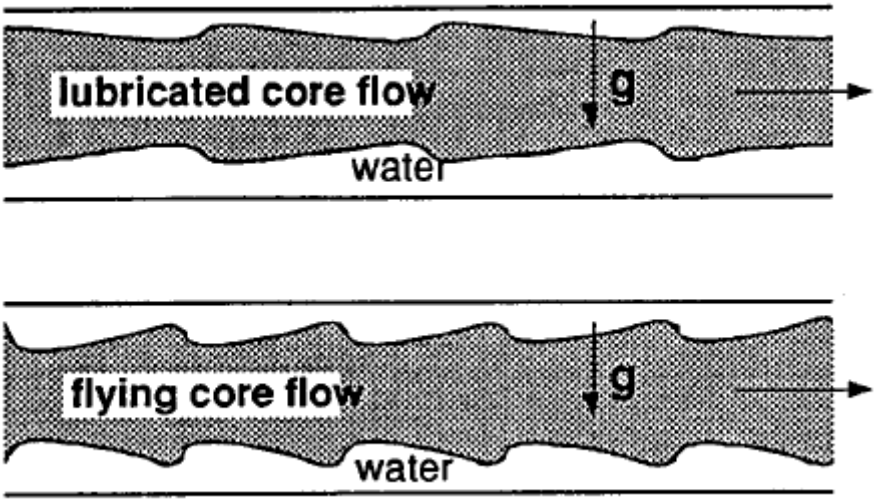

Figure 1.2: Description of the lubricated film model and flying core model to explain the downward force on the core. Figure taken from Joseph et al. [14].

Various efforts have been made to model core-annular flow and to study the conditions for which it is stable. Bai et al. [4] assumed the liquids to have the same density for horizontal pipe flow which makes the flow axisymmetric and they also assumed that the core was solid with standing waves at the interface. They found that the waves at the interface are not symmetric. Li and Renardy [19] have relaxed those assumptions by allowing for different densities for the two different liquids. They use the wave having the largest growth rate as the initial condition for the interface. They obtained stable core-annular flow with bamboo waves in their simulations. Experiments for vertical core-annular flows have been performed by Bai et al. [3]. They found that the holdup ratio remains constant as 1.39 for all flow conditions. The experiments also showed that there is a certain water flow rate for a given oil flow rate which gives minimum pressure drop and its value decreases with increasing oil flow rate. Experiments for horizontal core-annular flow have been carried out by Oliemans and Ooms [22]. They showed that the thickness of the water film in the pipe was not influenced by the water fractions that were used in their experiments. Thus, it has been showed with the help of experiments and theoretical models that core-annular flow can indeed be stable and it occurs for a wide range of oil properties and flow rates.

There are different pressure drop models available in literature for core-annular flow such as the ones given by Brauner [6] and Arney et al. [2] which can be used to predict the friction factor. A wide range of flow rates covering all the possible configurations like laminar core and laminar annulus, turbulent core and turbulent annulus and mixed flow regimes have been covered in the pressure drop model provided by Brauner [6]. A fully rough surface model for the friction factor is also provided to successfully mimic the conditions encountered in practice. Arney et al. [2] provided a friction factor model by combining the velocity profile of perfect core-annular flow and the Blasius friction factor. They take into account the skin friction caused by the lubricant shearing against the wall. The model did not account for the effects of wavy or eccentric core since it is based on perfect core-annular flow. Vanegas Prada and Bannwart [27] showed that perfect core-annular flow solution is not appropriate to get the friction factor values and it is thus important to model the effects of wavy core, turbulence in the annulus and the buoyancy on the friction factor. Ullmann and Brauner [26] have used the two-fluid model to derive the exact solution for the holdup and the pressure drop for laminar horizontal core-annular flow. This model was tested by them for laminar and turbulent core-annular flow experimental data and a good agreement was found. Thus, it is a convenient model to predict the pressure-drop for core-annular flows.

To understand the flow physics better and to make parametric studies, it is important to perform numerical simulations of core-annular flow. Ooms et al. [24] performed simulations for core-annular flow in a

horizontal pipe with a partly analytical and partly numerical approach which assumed the core to be solid. Beerens [5] has performed simulations for vertical and horizontal core-annular flow with a laminar annulus. He performed simulations for flows with a Reynolds number in the water annulus ($\frac{\rho_w V_w D}{\mu_w}$) less than 2000 and compared the numerical predictions with the experiments of Li and Renardy [19]. The predictions for the water hold up and the superficial oil velocities from the simulations are within 10 % of the data obtained from the experiments of Li and Renardy [19]. Since in industrial applications, the pipelines and the velocities are larger, the annulus is not always laminar. Thus, it is imperative to look at the turbulence characteristics in the annulus and the interface waves to study core-annular flows obtained in practice.

Usually for a turbulent flow it is not possible to solve the Navier-Stokes equations analytically. Hence numerical methods are employed which help in solving these equations. There are three major approaches for numerically solving the Navier-Stokes equations when turbulence is present. DNS is an approach in which all the scales of turbulence are resolved. This requires a very fine mesh and takes up a lot of computational time and memory. Large Eddy Simulations (LES) form another approach which filters the smallest scales and resolves it using different methods. This requires less computational effort than DNS but it is not yet extensively used for multiphase flows. The most used and discussed approach is through Reynolds averaging where the Navier-Stokes equations are time averaged to differentiate the mean and fluctuating quantities. The Reynolds Averaged Navier Stokes (RANS) equations require the least computational effort since they only take into account the mean quantities while averaging the fluctuating quantities to zero. The DNS approach solves the Navier-Stokes equations without any averaging and hence can be considered closer to the flow in practice though computational errors will always be present. But since it takes up a lot of computational expense, it is not efficient to use DNS to perform each and every simulation. But the DNS approach can be used as a standard to which the RANS approach can be compared and thus an understanding of the extent of accuracy of the RANS approach for core-annular flow can be obtained.

The turbulent perfect core-annular flow with eccentric core has been studied by Huang et al. [11]. The effect of eccentricity of the core on the friction factor and holdup were assessed. The numerical simulations were performed by using the low-Re k-ε turbulence model to model the turbulence in the water annulus. They observed that the friction factor increased with increase in eccentricity of the core. Ko et al. [16] used the shear stress transport (SST) k-ω model to model axisymmetric turbulent core-annular flow. They observed that the SST model gave more accurate results as compared to the original k-ω model. They also observed that the wavelength of the interfacial waves decreases with increasing Reynolds number while the pressure gradient increases with increasing Reynolds number. Ghosh et al. [8] performed time dependent 3D simulations for core-annular down-flow. They used the k-ε turbulence model and observed good agreements with the experiments. Shi et al. [25] used the SST k-ω model with turbulence damping to predict the flow structures inside horizontal core-annular flow. They used a medium viscosity ratio and found that the pressure drop and holdup were reasonably accurate in their simulations. They also considered different flow patterns for oil-water flows by changing the wall contact angle. They also examined the effects of using different turbulence models and found that the wave structure changes with changing turbulence models and the waves obtained in RANS simulations are smoother than those observed in the experiments.

Quite recently, Kim and Choi [15] have done Direct Numerical Simulations (DNS) for vertical turbulent core-annular flow. They perform simulations of five cases for different oil holdups keeping the friction Reynolds number constant. They have compared the predictions from the simulations with the data from the experiments done by Vanegas Prada and Bannwart [27] as they incorporate the same fluid properties for their simulations. The mean pressure gradients were measured by fixing the superficial oil and water velocities in the experiments done by Vangas Parada and Bannwart [27] but Kim and Choi [15] have specified a constant mean pressure gradient and oil holdup and they obtained the superficial oil and water velocities as the result of their simulation. This is done so as to utilise the advantage of periodic boundary conditions which enable the computational domain to be shorter. Kouris and Tsamopoulos [17] show that when using periodic boundary conditions it is not possible to prescribe both the volumes and the superficial velocities under a constant mean pressure gradient. Thus, only the volumes are specified in terms of oil holdup and the superficial velocities are obtained as the result.

1.1. Thesis research objective and tasks

Li et al. [18] have done 1D, 2D and 3D core-annular flow simulations using the Launder-Sharma low-Re k-ε model and compared these with lab experiments. They observe that there are significant differences between the simulation results and the lab experiments. The predicted pressure drop by the simulation is about 35% lower than the pressure drop measured in the experiments (for the same flowrate). The purpose of this thesis is to study the structure of the oil-water interfacial waves and the turbulence characteristics, through making a comparison with the predictions from the RANS approach and the existing DNS results from Kim and Choi [15] to help in understanding the difference observed by Li et al. [18]. The RANS simulations presented in this thesis are carried out using the open-source flow solver OpenFOAM. As the core levitates and becomes eccentric in horizontal core-annular flows, the flow does not remain axi-symmetric and it essentially becomes a 3D problem. The vertical core-annular flow can be treated as a 2D problem since the core is concentric and the flow can be assumed to be axi-symmetric. The advantage of carrying out simulations for the vertical pipe flow instead of the horizontal pipe flow is that 2D axi-symmetric simulations lead to much shorter computer times than the 3D simulations. The shorter computer time enables to carry out more parameter variations, which can also be helpful in understanding horizontal pipe flow. The objective of this thesis is to assess the accuracy of the RANS approach for core-annular flow, through making a detailed comparison of the RANS predictions with the DNS data presented by Kim and Choi [15]. The specific tasks required to reach this objective can be summarised below:

- Carry out 2D OpenFOAM simulations for one of the conditions for which DNS data from Kim and Choi [15] are available. Verify the numerical accuracy through grid refinement.
- Carry out 2D OpenFOAM simulations for all the other conditions for which DNS results from Kim and Choi [15] are available.
- Compare the 2D OpenFOAM and the DNS results from Kim and Choi [15] with 1D MATLAB results. The MATLAB model solves the 1D equations for core-annular flow using the low-Re k-ε model for turbulence. This MATLAB model has been demonstrated to accurately predict 1D core annular flows as also shown by Li et al. [18] and hence can be considered as the standard for 1D cases.
- Postprocess the results to find the structure (e.g. scaling) of the turbulent water annulus and the wave characteristics of the interfacial waves.
- Carry out a parameter study for 2D OpenFOAM simulations with the RANS approach (e.g. different lengths of the computational domain, different oil viscosity simulations).

2

Numerical methods

The governing equations in fluid dynamics are based on the principles of conservation of mass, momentum and energy. The energy will always be conserved for this particular problem of core-annular flow as it is assumed that the flow is isothermal. This assumption is valid since the flow velocity is large and there is not enough time for the heat to penetrate inside the pipe as observed from the experiments mentioned in [18]. The mass and momentum conservation equations, shown in equation 2.1 and 2.2 respectively, are known as the Navier-Stokes equations.

$$\frac{\partial u_i}{\partial x_i} = 0 \tag{2.1}$$

$$\frac{\partial u_i}{\partial t} + u_j \frac{\partial u_i}{\partial x_j} = -\frac{1}{\rho}\frac{\partial p}{\partial x_i} + \nu \frac{\partial^2 u_i}{\partial x_j^2} + g_i \tag{2.2}$$

The flow conditions are usually characterized by different dimensionless parameters obtained when the Navier-Stokes equations are non-dimensionalised. The importance of various terms in the governing equations can be determined from these dimensionless parameters. They can be linked to the physical phenomena taking place in the resulting flow. These dimensionless parameters frequently benefit the solution process when assumptions and approximations are required. Multiphase flows are usually characterized by the following dimensionless parameters:

- Reynolds number
$$Re = \frac{\rho V D}{\mu} \tag{2.3}$$
- Froude number
$$Fr = \frac{V^2}{gD} \tag{2.4}$$
- Weber number
$$We = \frac{\rho V^2 D}{\sigma} \tag{2.5}$$
- Eotvos number
$$Eo = \frac{\rho g D^2}{\sigma} \tag{2.6}$$

2.1. Interface tracking methods

There are two different liquids present in a core-annular flow whose densities and viscosities differ from each other. Also, the surface tension cannot be neglected due to the presence of an interface. Thus, the interface between the two liquids has to be tracked accurately. The interface tracking methods available in the literature and used in OpenFOAM are explained below.

Historically, two interface tracking methods have been used for multiphase flows. The Volume of Fluid (VOF)

method tracks the volume fraction in each cell to create the interface which ensures that the conservation of mass is guaranteed for this method. The Level Set (LS) method solves the transport equation for the signed-distance function to the interface. The advantage is that it resolves the interface sharply but the disadvantage is that it is not mass conserving. The advantages of both these methods are combined and incorporated in a method known as Coupled Volume of Fluid with Level Set (CLSVOF) method. These different methods are further explained in the following subsections.

2.1.1. Volume of Fluid method

The VOF method tracks the volume fraction, ψ, of the dispersed phase as defined in equation 2.7. Each fluid particle retains its phase value during its motion which makes the volume fraction, ψ, satisfy the conservation equation 2.8. Here, u is defined as the flow velocity and Fluid 1 refers to the dispersed phase which is oil while Fluid 2 refers to the carrier phase which is water for the specific problem of core-annular flow in this thesis.

$$\psi = \begin{cases} 0 & \text{Fluid 2} \\ 1 & \text{Fluid 1} \\ 0 < \psi < 1 & \text{Interface} \end{cases} \tag{2.7}$$

$$\frac{\partial \psi}{\partial t} + \nabla \cdot (u\psi) = 0 \tag{2.8}$$

The Navier-Stokes equations, 2.1 and 2.2, are solved simultaneously with the conservation equation 2.8. The density and viscosity for a particular cell is calculated as shown in equations 2.9 and 2.10 respectively.

$$\rho = \rho_1 \psi + \rho_2 (1 - \psi) \tag{2.9}$$

$$\mu = \mu_1 \psi + \mu_2 (1 - \psi) \tag{2.10}$$

The VOF method needs only one additional equation to be solved and thus is not computationally expensive. The solver in OpenFOAM uses the surface compression technique which solves the equation 2.11, where $u_r = u_1 - u_2$ represents the velocity along the interface between the two fluids. The third term from the left represents a mathematical contribution since the physical interface does not have a finite width. Hence, the VOF method considers the interface as having finite width because it defines the interface as distributed over the height of the cell which also results in the interface not remaining sharp. Thus, there is a need for local grid refinements where the interface is present.

$$\frac{\partial \psi}{\partial t} + \nabla \cdot (\psi u) + \nabla \cdot \left((1 - \psi) \psi u_r \right) = 0 \tag{2.11}$$

Since the geometric information about the interface is not directly calculated, the advection of the volume fraction and the calculation of surface tension force should be handled carefully so that the simulations are physically accurate. The advection of the volume fraction is done in two steps. The interface is reconstructed in each cell followed by the calculation of the flux of each fluid phase through each cell boundary using the reconstructed interface. The difficulty originates from the excessive diffusion while solving the advection equation. Thus, the discretization scheme chosen heavily influences this method as numerical diffusion depends on it. The Piecewise Linear Interface Reconstruction (PLIC) scheme is generally used to correctly compute the fluxes across cell faces by reconstruction of the interface within grid cells.

2.1.2. Level Set method

The interface between the two fluids is a material quantity, ϕ, which can be defined as shown in equation 2.12. This material quantity is used by the Level Set method to track the interface. The Level Set equation as shown in 2.13 is solved along with the Navier-Stokes equations, 2.1 and 2.2, The interface normal vector in this method is calculated as shown in equation 2.14.

$$\phi = \begin{cases} 0 & \text{Interface} \\ > 0 & \text{Fluid 1} \\ < 0 & \text{Fluid 2} \end{cases} \tag{2.12}$$

$$\frac{\partial \phi}{\partial t} + u \cdot \nabla \phi = 0 \tag{2.13}$$

$$\nabla_s \cdot n_{1\to 2} = \nabla \cdot \left(\frac{\nabla \phi}{|\nabla \phi|} \right) \tag{2.14}$$

The re-initialization of the level set is required after every time step since the level set method is not mass conserving and also ϕ is not a material quantity outside the interface. The advantage of the Level Set method is that there is a sharp interface representation.

2.1.3. Coupled Volume of Fluid with Level Set method

Albadawi et al. [1] combined the advantages of the VOF method and the LS method to get a new combined method known as Coupled Volume of Fluid with Level Set method (CLSVOF). The volume fraction from the VOF method is first utilised to solve the transport equation and then the level set function is used to calculate the re-initialization equation shown in equation 2.15 to improve the calculation of the curvature of the interface and the surface normal.

$$\frac{\partial \phi}{\partial \tau} = \text{Sign}\left(\phi_0\right)\left(1 - |\nabla \phi|\right) \tag{2.15}$$

$$\phi(x,0) = \phi_0(x) \tag{2.16}$$

where,

ϕ is the level set function,
τ is the artificial time, $\Delta\tau = 0.1\Delta x$,
Sign is the signum function,
ϕ_0 is the intial value of the level set function, $\phi_0 = (2\psi - 1)\Gamma$,
$\Gamma = 0.75\Delta x$.

The value of the interface thickness is defined as shown in equation 2.17 where ϵ_c is the coefficient of interface thickness which is an arbitrary parameter and determines the width of the delta function. The re-initialization equation is solved for $10\epsilon_c (= \epsilon/\Delta\tau)$ iterations. Yamamoto et al. [28] observed that a continuous distribution of the level set function is obtained when the re-initialization equation was solved in such a way. It was also observed that this approach improves the calculation of the curvature of the interface and the surface normal.

$$\epsilon = \epsilon_c \Delta x \tag{2.17}$$

The CLSVOF method uses the level set function as shown in equation 2.18, where the delta function is calculated as shown in equation 2.19.

$$\boldsymbol{F}_{\sigma,\phi} = \sigma k_\phi \delta_\phi \nabla \phi \tag{2.18}$$

$$\delta_\phi = \begin{cases} \frac{1}{2\epsilon}\left(1 + \cos\left(\frac{\pi\phi}{\epsilon}\right)\right) & |\psi| < \epsilon \\ 0 & \text{else.} \end{cases} \tag{2.19}$$

Here σ is the surface tension and k represents the curvature of the interface.

Yamamoto et al. [28] compared the VOF method and the CLSVOF method for a static and dynamic case of an isothermal liquid bubble and gas droplet. They examined different numerical grids and determined that the spurious current velocity at the interface is always less for the CLSVOF method as compared to the VOF method. The maximum and average spurious currents at the interface were less for the CLSVOF method as compared to the VOF method. The relative errors in the calculation of Laplace pressure and the pressure field are less when the CLSVOF method is used as compared to the VOF method. Thus, it is indicated that the CLSVOF method improves the pressure and velocity predictions along the interface and is thus used in this thesis as the interface tracking method.

2.2. Turbulence models

The Reynolds number based on the mean water height, as shown in equation 2.20, for the flow conditions encountered in this thesis is in the range of 1150-3550 which makes the flow turbulent in the water annulus.

Hence it is necessary to understand how the turbulence models work and choose a suitable turbulence model for the prescribed flow conditions.

$$\mathrm{Re}_c = \frac{u_{core}\left(R - H_{avg}\right)}{\nu_w} \tag{2.20}$$

Here u_{core} is the velocity of the core and H_{avg} is the mean radial location of the phase interface.

It is important to resolve the flow near the wall and understand the physics inside the boundary layer since the area near the wall is a high shear area. The available high-Re turbulence models when used with wall functions do not resolve the viscous sublayer ($y^+ < 5$) sufficiently. Thus, some modifications are done to these high-Re turbulence models such that they can be used down to the wall. These modified turbulence models are known as low-Re turbulence models.

2.2.1. Low-Re $k-\varepsilon$ models

When deriving low-Re turbulence models, the terms are modelled in such a way that the behaviour very near to the walls can be studied and require that the exact equations also behave in the same way. The exact k-equation near the wall is shown in equation 2.21 while the modelled equation is as shown in equation 2.22.

$$\frac{\partial \rho \bar{U} k}{\partial x} + \frac{\partial \rho \bar{V} k}{\partial y} = \underbrace{-\rho \overline{uv} \frac{\partial \bar{U}}{\partial y}}_{O(y^3)} - \frac{\partial \overline{pv}}{\partial y} \underbrace{- \frac{\partial}{\partial y}\left(\frac{1}{2}\overline{\rho v u_i u_i}\right)}_{O(y^3)} + \mu \frac{\partial^2 k}{\partial y^2} \underbrace{- \mu \overline{u_{i,j} u_{i,j}}}_{O(y^0)} \tag{2.21}$$

$$\frac{\partial \rho \bar{U} k}{\partial x} + \frac{\partial \rho \bar{V} k}{\partial y} = \underbrace{\mu_t \left(\frac{\partial \bar{U}}{\partial y}\right)^2}_{O(y^4)} + \underbrace{\frac{\partial}{\partial y}\left(\frac{\mu_t}{\sigma_k}\frac{\partial k}{\partial y}\right)}_{O(y^4)} + \mu \frac{\partial^2 k}{\partial y^2} \underbrace{- \rho \varepsilon}_{O(y^0)} \tag{2.22}$$

The pressure distribution term is neglected in these models as it is negligible close to the wall. When comparing the exact equation and the modelled equation, it is seen that the dissipation term behaves in the same way as it is $O\left(y^0\right)$ in both the equations. But the production and diffusion terms are of different orders in the exact equation and the modelled equation.The production term is $O\left(y^4\right)$ as shown in equation 2.23. This can be changed by using $c_\mu f_\mu$ instead of just c_μ where f_μ is a damping function such that $f_\mu = O\left(y^{-1}\right)$ when $y \to 0$ and $f_\mu \to 1$ when $y^+ > 50$.

$$\nu_t = c_\mu \rho \frac{k^2}{\varepsilon} = \frac{O\left(y^4\right)}{O\left(y^0\right)} = O\left(y^4\right) \tag{2.23}$$

A number of low-Re $k-\varepsilon$ models are available in the literature. These models either solve for a modified dissipation $\tilde{\varepsilon}$ or for the normal dissipation as the dependent variable. The modified dissipation is sometimes used to mitigate the need of a damping function. The damping functions and the extra source terms are different for different models.

2.2.1.1. Launder-Sharma low-Re $k-\varepsilon$ model

The equations used for the Launder-Sharma low-Re $k-\varepsilon$ model are as shown in equations 2.24-2.27. This model is based on the one given by Jones and Launder [12].

$$\frac{\partial \rho \bar{U} k}{\partial x} + \frac{\partial \rho \bar{V} k}{\partial y} = \frac{\partial}{\partial y}\left[\left(\mu + \frac{\mu_t}{\sigma_k}\right)\frac{\partial k}{\partial y}\right] + \mu_t \left(\frac{\partial \bar{U}}{\partial y}\right)^2 - \rho \varepsilon \tag{2.24}$$

$$\frac{\partial \rho \bar{U} \tilde{\varepsilon}}{\partial x} + \frac{\partial \rho \bar{V} \tilde{\varepsilon}}{\partial y} = \frac{\partial}{\partial y}\left[\left(\mu + \frac{\mu_t}{\sigma_\varepsilon}\right)\frac{\partial \tilde{\varepsilon}}{\partial y}\right] + c_{1\varepsilon} f_1 \frac{\tilde{\varepsilon}}{k} \mu_t \left(\frac{\partial \bar{U}}{\partial y}\right)^2 - c_{\varepsilon 2} f_2 \rho \frac{\varepsilon^2}{k} + E \tag{2.25}$$

$$\mu_t = c_\mu f_\mu \rho \frac{k^2}{\tilde{\varepsilon}} \tag{2.26}$$

$$\varepsilon = \tilde{\varepsilon} + D \tag{2.27}$$

The damping functions and the source terms that are used in this model are given in equations 2.28-2.33. The term E was added to include the experimental peak in k at around $y^+ \simeq 20$. The f_2 term mimics the final stage of decay behind a turbulence generating grid.

$$f_\mu = \exp\left(\frac{-3.4}{(1 + R_T/50)^2}\right) \tag{2.28}$$

$$f_1 = 1 \tag{2.29}$$

$$f_2 = 1 - 0.3\exp\left(-R_T^2\right) \tag{2.30}$$

$$D = 2\mu\left(\frac{\partial\sqrt{k}}{\partial y}\right)^2 \tag{2.31}$$

$$E = 2\mu\frac{\mu_t}{\rho}\left(\frac{\partial^2\bar{U}}{\partial y^2}\right)^2 \tag{2.32}$$

$$R_T = \frac{k^2}{\nu\tilde{\varepsilon}} \tag{2.33}$$

2.2.1.2. Boundary condition for ε and $\tilde{\varepsilon}$

The boundary condition for ε is rather complicated and so some of the models use $\tilde{\varepsilon}$ as the dependent variable. The viscous diffusion and the dissipation term are the largest in the modelled equation near the wall since they are of $O\left(y^0\right)$ such that the equation looks like as shown in equation 2.34.

$$0 = \mu\frac{\partial^2 k}{\partial y^2} - \rho\varepsilon \tag{2.34}$$

From equation 2.34, the boundary condition for ε can be obtained as shown in equation 2.35.

$$\varepsilon_{\text{wall}} = \nu\frac{\partial^2 k}{\partial y^2} \tag{2.35}$$

An alternative form of the boundary condition can be derived from equation 2.34. The exact form of the dissipation term close to the wall can be written as in equation 2.36.

$$\varepsilon = \nu\left\{\overline{\left(\frac{\partial u}{\partial y}\right)^2 + \left(\frac{\partial w}{\partial y}\right)^2}\right\} \tag{2.36}$$

Using Taylor expansion for ε and k, we get the equations as shown in 2.37 and 2.38 respectively.

$$\varepsilon = \nu\left(\overline{a_1^2} + \overline{c_1^2}\right) + \ldots \tag{2.37}$$

$$k = \frac{1}{2}\left(\overline{a_1^2} + \overline{c_1^2}\right)y^2 \ldots \tag{2.38}$$

Using equation 2.38, equation 2.39 is obtained which when compared with equation 2.37 gives the boundary condition for ε as shown in equation 2.40.

$$\left(\frac{\partial\sqrt{k}}{\partial y}\right)^2 = \frac{1}{2}\left(\overline{a_1^2} + \overline{c_1^2}\right)\ldots \tag{2.39}$$

$$\varepsilon_{\text{wall}} = 2\nu\left(\frac{\partial\sqrt{k}}{\partial y}\right)^2 \tag{2.40}$$

The equation for D in the low-Re Launder-Sharma model as shown in equation 2.31 is the same as obtained in equation 2.40 and thus using equation 2.27, a new boundary condition for the modified dissipation $\tilde{\varepsilon}$ is obtained which is as shown in equation 2.41.

$$\tilde{\varepsilon} = 0 \tag{2.41}$$

2.2.2. The low-Re $k-\omega$ model

The standard $k-\omega$ model can be used all the way to the wall without any additional modifications. The only thing that has to be handled specifically for near-wall treatment is the boundary conditions since

$$\omega = \frac{\varepsilon}{\beta^* k} = O\left(y^{-2}\right) \tag{2.42}$$

tends to infinity. As shown in section 2.2.1.2, the boundary condition for ω is derived in the same way as the boundary conditions for ε is derived. The ω-equation is as shown in equation 2.43 which when used near the wall reduces to the viscous diffusion term and the dissipation term as shown in equation 2.44.

$$\left(\rho \bar{U}_j \omega\right)_{,j} = \left[\left(\mu + \frac{\mu_t}{\sigma_\omega}\right)\omega_{,j}\right]_j + \frac{\omega}{k}\left(c_{\omega 1} P_k - c_{\omega 2}\rho k\omega\right) \tag{2.43}$$

$$0 = \mu\frac{\partial^2 \omega}{\partial y^2} - c_{\omega 2}\rho\omega^2 \tag{2.44}$$

Thus the boundary condition is as given in equation 2.45.

$$\omega = \frac{6\nu}{c_{\omega 2} y^2} \tag{2.45}$$

The ω-equation is not usually solved close to the wall. For $y^+ < 2.5$, ω is calculated from equation 2.45 and hence no boundary condition is actually needed.

2.2.3. Performance of low-Re turbulence models

The comparison of high-Re $k-\varepsilon$ and low-Re $k-\varepsilon$ turbulence models has been done in the past and it has been shown that for wall bounded flows, the low-Re $k-\varepsilon$ turbulence models perform better than the high-Re $k-\varepsilon$ models. Martinuzzi and Pollard [20] showed that for developing turbulent pipe flows, the low-Re $k-\varepsilon$ models provide better predictions than the Reynolds stress and algebraic stress models. Also for low-Re number flows, the low-Re $k-\varepsilon$ models were in better agreement with the experiments as compared to the high-Re $k-\varepsilon$ models.

Hrenya et al. [10] show that for a single-phase turbulent pipe flow, the Launder-Sharma $k-\varepsilon$ model performs reasonably well when compared to the experiments and DNS results. They also show that mean axial velocity for the pipe flow is predicted correctly while there is slight under prediction for the turbulent kinetic energy. Mathur and He [21] show that the Launder-Sharma $k-\varepsilon$ model has been accepted as a benchmark to model low-Re turbulent flows and has been used to model a variety of turbulent flows. Though the Launder-Sharma $k-\varepsilon$ model was initially developed to model swirling flows, it has been used for boundary layer flows and natural convection cavity flows as well. The Launder-Sharma model was in good agreement with the experiments for these kind of flows. The Launder-Sharma model was also in agreement with the experiments for mixed convection air flow in vertical pipes. Similar agreements were reported for mixed convection heat transfer to supercritical fluids in literature. This model is also shown to predict unsteady turbulent flows reasonably well. Transient response to heat transfer in a turbulent pipe has also been shown to be in good agreement with the experiments in the literature.

Mathur and He [21] compared different implementations of the Launder-Sharma $k-\varepsilon$ model. They compared the modelling while taking the normal dissipation and modified dissipation as the dependent variable. They observe that there is a notable difference between the values of ε and $\tilde{\varepsilon}$ near the wall. The modified dissipation term is used in the original model for numerical advantages. They observe that the predictions when using the modified dissipation term, as used in the original model, agree well with the literature. It closely produces the experimental and DNS results for steady and unsteady pipe flow. Thus, it has been shown that the original model proposed shows the best agreements with experiments and DNS results for a wide variety of flows as well as unsteady turbulent flows and hence will be used as the turbulence model in this thesis.

2.3. Discretization schemes and time step restrictions

The standard discretization schemes are used in this thesis which are second order backward implicit in time and second order for the advection terms of the momentum equations. The first order upwind schemes are

used for the advection of the turbulent kinetic energy and for advection of the turbulent dissipation rate. The PIMPLE algorithm with three corrector loops is used for the pressure-velocity coupling. The Preconditioned Bi-Conjugate Gradient (PBiCG) solver is the linear solver that is used for velocity components, turbulent kinetic energy and the turbulent dissipation rate while the linear solver used for pressure is Geometric agglomerated algebraic multigrid (GAMG) solver.

An adjustable time step is used for solving the RANS equations by the CLSVOF solver which is based on the maximum mean Courant number and the maximum interface Courant number. The mean Courant number for n degrees of freedom can be calculated as shown in equation 2.46, where Δx is the grid spacing. The interface Courant number only concerns the velocity of the interface normal to itself in surface cells.

$$Co = \Delta t \sum_{i=1}^{n} \frac{u_i}{\Delta x_i} \tag{2.46}$$

Deshpande et al. [7] provide a criterion for the time step based on their observations while simulating a 2D stationary droplet. They observe that both, accurate calculation of the curvature and discrete balance between the pressure gradient and the surface tension, are required in order to minimize the spurious currents at the interface. Thus, the explicit treatment of the surface tension places a condition on the time step given by equation 2.47.

$$\tau_\rho = \Delta t < \sqrt{\frac{\rho \Delta x^3}{\sigma}} \tag{2.47}$$

Another time step was also defined which included the effect of viscosity leading to a more generalized time step criterion. This time step is defined as shown in equation 2.48.

$$\tau_\mu = \frac{\mu \Delta x}{\sigma} \tag{2.48}$$

Deshpande et al. [7] did the same simulations with different coordinates to obtain the relation between the two time steps as defined in equations 2.47 and 2.48 respectively. A relation for the maximum time step, shown in equation 2.49, was obtained by differentiating between the stable and unstable cases for the simulations done. The analysis by Deshpande et al. [7] was carried out for the interFoam solver in OpenFOAM, based on the VOF method, but since the CLSVOF solver also employs the VOF method, the time step restrictions will be the same. Hence, the maximum mean Courant number and the maximum interface Courant number will be restricted to 0.01 for this thesis based on these observations.

$$\Delta t \leqslant \max\left(10\tau_\mu, 0.1\tau_\rho\right) \tag{2.49}$$

3

Geometry and Meshing

3.1. Flow geometry

A wedge shaped domain as shown in Figure 3.1 is used to carry out axisymmetric 2D calculations in OpenFOAM. The wedge is a 3D shape but the tangential direction is taken as a unit cell length, essentially making the domain 2D. The length of the domain is chosen such that the least amount of streamwise pipe section is simulated. The predictions of the simulations are independent of the streamwise domain length chosen. This will be demonstrated in Chapter 5.

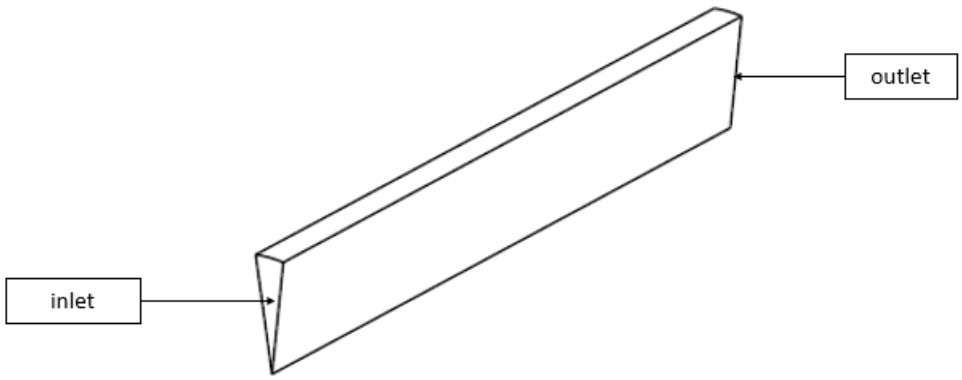

Figure 3.1: Wedge shaped flow domain used to carry out OpenFOAM simulations in this thesis.

3.2. Boundary conditions

The periodic boundary condition is applied to the computational domain which mitigates the need to simulate the whole length of the pipe. The periodic boundary condition is used when the geometry and the flow pattern are periodically repeated. Since the simulated core-annular flow will be fully developed and the pipe remains the same over its length, the geometry and the flow pattern will repeat and thus periodic boundary condition can be applied. The equations for the velocity components are shown in 3.1, assuming the length of the computational domain is L.

$$\begin{aligned} u(x) &= u(x+L) = u(x+2L) = \cdots \\ v(x) &= v(x+L) = v(x+2L) = \cdots \\ w(x) &= w(x+L) = w(x+2L) = \cdots \end{aligned} \tag{3.1}$$

The pressure does not remain periodic but the pressure drop is periodic and can be obtained as shown in equation 3.2.

$$\Delta p = p(x) - p(x+L) = p(x+L) - p(x+2L) = \cdots \tag{3.2}$$

When applying the periodic boundary condition, the flow across two opposite planes in the computational domain should be identical. The flow entering the computational domain through the inlet should be identical to the flow leaving the computational domain through the outlet. The inlet and outlet for the current computational domain are shown in Figure 3.1. This means that the total mass of the oil and the water inside the computational domain is fixed as there is no way mass can be added from one end without removing it from the other periodic end and vice versa. Since no mass, oil and water, can leave the calculation domain without entering at the other end it is necessary to fix the oil holdup inside the computational domain.

To drive the flow inside the simulation domain, a forcing term has to be specified or else the flow gets slower and slower and eventually stops. There are two approaches in which this forcing can be applied. The first approach is where the mass flow rate is kept constant in time while the pressure gradient varies in time. When the mass flow rate is kept constant in time, an artificial forcing term is applied to the flow which acts as the pressure gradient. This artificial forcing term is iterated during every time step until the specified mass flow is obtained. The final value of the artificial forcing term for every time step is the desired output of the pressure gradient in time. The other approach is to keep the pressure gradient constant in time while the mass flow rate varies in time. The pressure gradient acts directly as the forcing term here which drives the flow and the desired output of mass flow rate is obtained in time. For this thesis, the periodic boundary condition is applied with the pressure gradient being constant in time which was also done by Kim and Choi [15]. Thus, in the RANS OpenFOAM simulations, the pressure drop and oil holdup fraction are prescribed, and the total flow rate and water-cut follow as output results.

3.3. Initial conditions and fluid properties

The initial condition for the simulations are the analytical solutions for PCAF as given by Li and Renardy [19]. The geometric parameters used to define PCAF are shown in Figure 3.2. The pipe radius is R while the undisturbed interface position is R_1. The frictional pressure gradient in the axial direction is constant and is denoted by $-\frac{dP}{dx}$ and the surface tension is denoted by σ. There are certain dimensionless parameters defined to model the PCAF as given below:

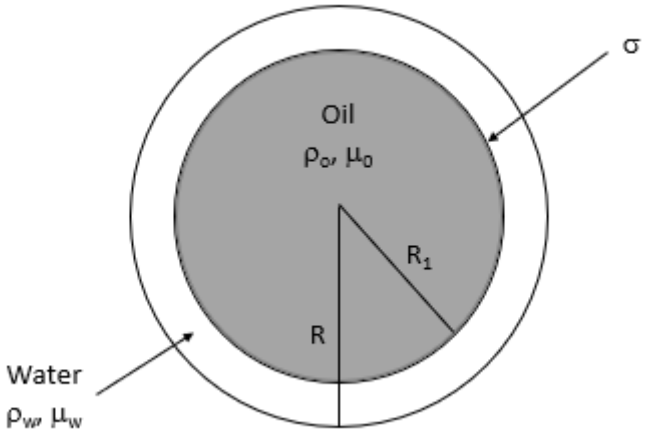

Figure 3.2: Geometric parameters for core-annular flow.

- Ratio of oil viscosity to water viscosity

$$m = \frac{\mu_w}{\mu_o} \tag{3.3}$$

- Ratio of pipe radius and mean radial location of the phase interface

$$a = \frac{R}{R_1} \tag{3.4}$$

- Ratio of oil density to water density

$$\zeta = \frac{\rho_w}{\rho_o} \tag{3.5}$$

- Ratio of the driving forces in the core and the annulus

$$K = \frac{\left(-\frac{\mathrm{d}P}{\mathrm{d}x} + \rho_o g\right)}{\left(-\frac{\mathrm{d}P}{\mathrm{d}x} + \rho_w g\right)} \tag{3.6}$$

- Parameter for surface tension

$$J = \frac{\sigma R_1 \rho_o}{\mu_o^2} \tag{3.7}$$

- Reynolds number for oil

$$Re_o = \frac{\rho_o v_0(0) R_1}{\mu_o} \tag{3.8}$$

- Reynolds number for water

$$Re_w = \frac{\rho_w v_0(0) R_1}{\mu_w} \tag{3.9}$$

Here $v_0(0)$ is the centreline velocity for PCAF given in equation 3.10 where A is defined as shown in equation 3.11.

$$v_0(0) = \left(-\frac{\mathrm{d}P}{\mathrm{d}x} + \rho_w g\right) \frac{R_1^2}{4\mu_w} A \tag{3.10}$$

$$A = mK + a^2 - 1 + 2(K-1)\log a \tag{3.11}$$

The velocity in the radial direction can be defined as shown in equation 3.12 which is used to initialize the velocity fields for the simulations performed in this thesis.

$$v(r) = \begin{cases} \left[a^2 - r^2 - 2(K-1)\log(r/a)\right]/A, & 1 \leqslant r \leqslant a \quad \text{(annulus)} \\ 1 - mr^2 K/A, & r < 1 \quad \text{(core)}. \end{cases} \tag{3.12}$$

The total flow rate, the pressure drop, the water-cut and the oil holdup fraction are the four parameters which can be used to completely define a core-annular flow configuration. The two parameters among the four are set as the input for the simulations, while the other two will be obtained as the results of the simulation. Here, Q_o is the oil flow rate, Q_w is the water flow rate, V_o is the volume occupied by oil, V_w is the volume occupied by water and V is the total volume of the pipe. The parameters are defined as follows:

- Total flow rate

$$Q = Q_w + Q_o \tag{3.13}$$

- Oil holdup fraction

$$\varepsilon_o = V_o/V \tag{3.14}$$

- Water-cut

$$WC = \frac{Q_w}{Q_w + Q_o} \tag{3.15}$$

There are some parameters which will be used to analyse the results obtained from the simulations. Here, $v_o = Q_o/A$ and $v_w = Q_w/A$ are the superficial oil and water velocities respectively. The parameters are defined below:

- Mean radial location of the phase interface

$$H_{\text{avg}} = \varepsilon_o^{1/2} R \tag{3.16}$$

- Holdup ratio

$$h = \frac{Q_o/Q_w}{V_o/V_w} \tag{3.17}$$

- Fanning friction factor

$$f = -\frac{\frac{dP}{dx}R}{\rho_w(v_o + v_w)^2} \tag{3.18}$$

The density and viscosity of the oil used in this thesis are ρ_o= 963 kg m^{-3} and μ_o= 0.745 Pa s respectively for the 2D OpenFOAM simulations. While for the 1D OpenFOAM simulations, the oil viscosity μ_o used is 17.6 Pa s. The density and viscosity of water are ρ_w= 998 kg m^{-3} and μ_w= 0.001 Pa s respectively. The oil is assumed to be Newtonian as also done by Kim and Choi [15]. The surface tension coefficient is taken as σ = 0.03 N m^{-1}. The fluid properties are the same as used by Kim and Choi [15] for their simulations and by Vanegas Prada and Bannwart [27] for their experiments except for the oil viscosity, which is equal to 17.6 Pa s for the DNS simulations done by Kim and Choi [15]. (See appendix A).

Applying the momentum balance to a pipe section, equation 3.19 is obtained where $\int \rho g \, \mathrm{d}V$ is the gravitational force and $\bar{\tau}_w$ is the mean wall shear stress on the pipe wall.

$$-\frac{\mathrm{d}P}{\mathrm{d}x} = \frac{2\bar{\tau}_w}{R} + \frac{1}{V}\int \rho g \, \mathrm{d}V \tag{3.19}$$

Equation 3.19 is normalized by the friction velocity ($u_\tau = \sqrt{\bar{\tau}_w/\rho_w}$) and the pipe radius ($R$) to obtain equation 3.20.

$$-\frac{\mathrm{d}P/\mathrm{d}x}{\rho_w u_\tau^2/R} = 2 + \frac{\int \rho g \, \mathrm{d}V/V}{\rho_w u_\tau^2/R} \tag{3.20}$$

The friction Reynolds number $\mathrm{Re}_\tau = u_\tau R/\nu_w = 720$ is fixed in the DNS cases considered by Kim and Choi [15] and thus will also be fixed for the simulations done in this thesis. This Reynolds number was chosen by Kim and Choi [15] from the experimental data ($2\bar{\tau}_w/R$ = 400Pa m^{-1}) of Vanegas Prada and Bannwart [27]. The value of the friction velocity thus is 0.053m s^{-1}. As mentioned in section 3.2, the mean pressure gradient in the axial direction and the oil holdup are applied as the boundary conditions. This also means that the mean radial location of the phase interface is pre-determined. The imposed conditions and the domain length for the five cases simulated by Kim and Choi [15] is given in table 3.1.

Table 3.1: Imposed conditions and domain length for 2D OpenFAOM simulations with different oil holdup fraction.

ε_o	H_{avg}/R	$-\mathrm{d}P/\mathrm{d}x$ (Pa m^{-1})	Domain length (streamwise, radial, tangential)
0.91	0.954	9879.6	$(R, R, 1)$
0.83	0.911	9905.6	$(R, R, 1)$
0.71	0.843	9945.6	$(1.2R, R, 1)$
0.62	0.787	9977.6	$(1.2R, R, 1)$
0.56	0.748	10001.6	$(1.2R, R, 1)$

3.4. Meshing

The meshing is done in such a way that there are less grid cells in the oil core but more cells in the water annulus and near the wall. The water annulus is turbulent and the boundary layer needs to be resolved sufficiently to describe the turbulence characteristics inside the annulus. Hence it is important to resolve the viscous sublayer, when using the low-Re turbulence models, which means that the wall r^+ should be less than 5. Ideally it is desired to have the wall r^+ equal to or less than 1.

To ensure that the mesh is concentrated near the wall, a hyperbolic tangent function can be used to create the mesh. The function that is used to create the mesh for this thesis is shown in equation 3.21.

$$\frac{r_j}{r_{j\max}} = 1 + \frac{\tanh\left[\alpha_1(j/j\max - 1)/2\right]}{\tanh(\alpha_1/2)}, \quad j = 0, 1, \ldots, j\max \tag{3.21}$$

where j max is the maximum number of grid cells across the boundary layer thickness. The coefficient α_1 is calculated as shown in equation 3.22 where α_2 is taken as 0.015.

$$\alpha_2 = \frac{\alpha_1}{\sinh(\alpha_1)} \tag{3.22}$$

The wall r^+ value is calculated as shown in equation 3.23. Here Δr is defined as the cell height of the first cell from the wall. The equation 3.21 is first used to calculate the coordinates of all the cells in the mesh. The cell height can be calculated from the coordinates obtained. The calculated cell height of the last cell, which is the first from the wall, is used in equation 3.23.

$$r^+ = \Delta r \frac{u_\tau}{\nu_w} \tag{3.23}$$

The mesh used for the 2-D case with the oil holdup fraction 0.71 is shown in Figure 3.3. There are 200 cells in the radial direction and 100 cells are used in the streamwise direction. Figure 3.3b is a zoomed-in view and shows only a section of the pipe. The red area in the Figure 3.3 is the oil core while the blue area is the water annulus. It clearly shows the higher concentration of the grid cells near the wall and in the water annulus.

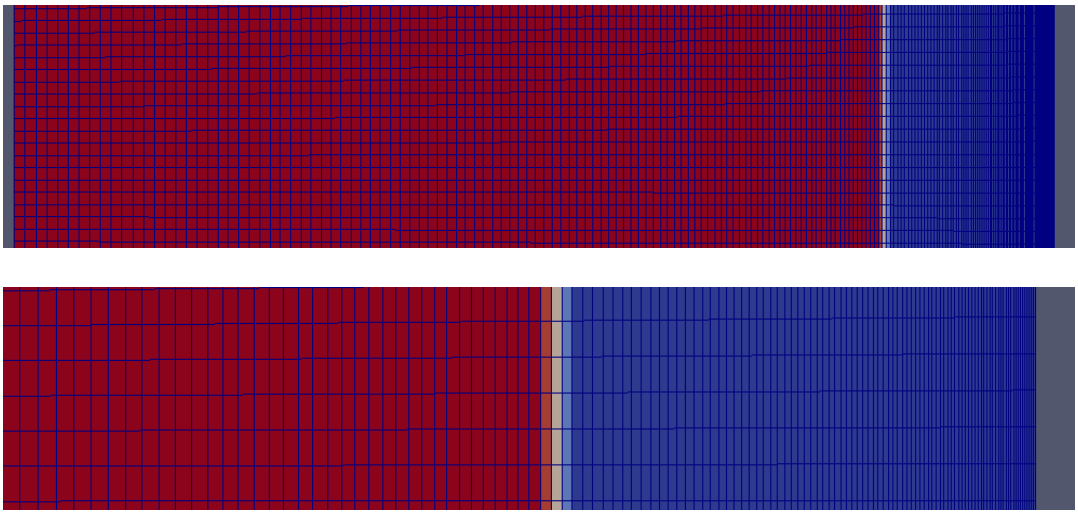

(a)

(b)

Figure 3.3: Concentration of grid cells near the wall for 2D OpenFOAM simulations (a) Normal view (b) Zoomed view.

4

1D simulations

A 2D core-annular flow has a wavy interface. If 1D core-annular flow is considered, the waves at the interface have to be neglected. The 1D simulations only take into consideration the flow physics in the radial direction. But 1D core-annular flow simulations are important in determining if turbulence is sufficiently resolved or not by studying the variation in the radial direction. Since only one dimension needs to be resolved in the domain, the 1D simulations are computationally very fast. It also gives an idea about the number of grid cells to be used in the radial direction for the 2D simulations. The oil viscosity used for 1D simulations is the same as Kim and Choi [15] i.e. 17.6 Pa s. A specific case of $\varepsilon_o = 0.71$ is used to determine the grid independence and the predictions are also compared with the 1D MATLAB results which will be considered as the standard for 1D core-annular flow simulations. Also, all five cases, for different oil holdups, from Kim and Choi [15] are analysed and the scaling of turbulence in the water annulus is verified.

4.1. 1D MATLAB model

The 1D MATLAB model uses a line as the simulation domain and resolves the flow in only the radial direction. It also uses the Launder-Sharma low-Re k-ε turbulence model. Since the geometry is a line, the computational expense of the simulation is very small and a single simulation can be performed in a matter of seconds. To consider the 1D MATLAB model as the standard to which the RANS results can be compared, it is necessary to demonstrate that the predictions from the 1D MATLAB model are grid independent. To determine the grid independency, the case with $\varepsilon_o = 0.71$ is chosen. The simulations are performed on four different grids with 120, 240, 480 and 960 grid cells respectively. The grid cells are equally divided in the water annulus and the oil core with the wall r^+ value being less than 1. The variation of the velocity magnitude for the four grids is shown in Figure 4.1. It shows that the prediction is very accurate and the curves are almost on top of each other for the 240, 480 and 960 grid cells case. The comparison of the flow rates and the water-cut for all four grids is shown in Table 4.1. This also shows that there is a negligible difference between the four grids. Hence, the 1D MATLAB model with 960 grid cells can be considered as the standard to which the RANS simulations can be compared.

Table 4.1: Grid independence test for four different grids with 120, 240, 480 and 960 cells respectively in the radial direction from the 1D MATLAB model.

	120 grid cells	**240 grid cells**	**480 grid cells**	**960 grid cells**
Imposed pressure drop ($\mathrm{Pa\,m^{-1}}$)	9945.6	9945.6	9945.6	9945.6
Imposed oil holdup	0.71	0.71	0.71	0.71
Oil flow rate ($\mathrm{m^3\,s^{-1}}$)	7.03×10^{-4}	7.21×10^{-4}	7.26×10^{-4}	7.28×10^{-4}
Water flow rate ($\mathrm{m^3\,s^{-1}}$)	1.41×10^{-4}	1.45×10^{-4}	1.46×10^{-4}	1.46×10^{-4}
Total flow rate ($\mathrm{m^3\,s^{-1}}$)	8.44×10^{-4}	8.66×10^{-4}	8.72×10^{-4}	8.74×10^{-4}
Water-cut	0.167	0.167	0.167	0.167

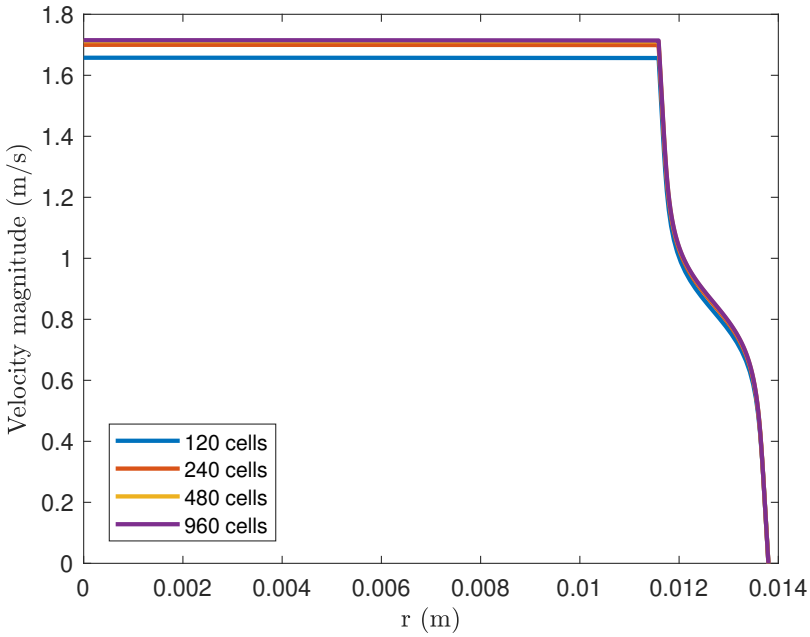

Figure 4.1: Comparison of velocity magnitude for the four different grid sizes used from the 1D MATLAB model.

4.2. Comparison with 1D MATLAB results

The case with oil holdup $\varepsilon_o = 0.71$ and imposed pressure drop of 9945.6 $\mathrm{Pa\,m^{-1}}$ is considered for 1D OpenFOAM simulations. The wedge shaped domain is used in OpenFOAM with 2 grid cells in the streamwise direction and 1 grid cell in the tangential direction, essentially making it a 1D domain. The streamwise domain length used is 0.00256 m. The number of grid cells can be varied in the radial direction to perform the grid independence study and also to compare the predictions from different grids in OpenFOAM with the MATLAB results. There are three different grid considered with 100, 200 and 400 grid cells in the radial direction respectively. All the other properties and conditions are kept constant. It is confirmed that there are no waves present as shown in Figure 4.2. The Figure 4.2 is the snapshot at 20 s for the simulation with 200 grid cells.

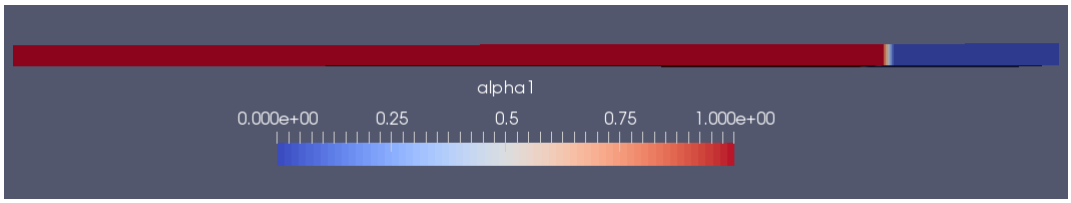

Figure 4.2: No waves at the interface for 1D simulations.

The variation of the oil, water and total flow rates in time for all three grids is shown in Figure 4.3. As can be seen, the simulation with 100 grid cells gives almost steady values for the flow rates after 10 s while the simulation with 200 grid cells gives almost steady values for the flow rates after 20 s. The simulation with 400 grid cells has been performed until 180 s but it still has a minor change in the flow rate values. The results obtained from the simulations and the predictions from the 1D MATLAB model are compared in Table 4.2. As can be observed, the simulation with 100 grid cells does not give a comparable prediction with the simulation with 200 grid cells and 400 grid cells respectively and also with the 1D MATLAB model. The flow rate predictions from the simulation with 200 and 400 grid cells respectively are slightly lower as compared to the predictions from the 1D MATLAB model.

The radial variation of the velocity and the turbulence characteristics of the flow are analyzed and compared

Table 4.2: Comparison of 1D RANS OpenFOAM results for 100, 200 and 400 grid cells respectively with the 1D MATLAB model.

	1D MATLAB	**100 grid cells**	**200 grid cells**	**400 grid cells**
Imposed pressure drop ($Pa\,m^{-1}$)	9945.6	9945.6	9945.6	9945.6
Imposed oil holdup	0.71	0.71	0.71	0.71
Oil flow rate ($m^3\,s^{-1}$)	7.28×10^{-4}	5.30×10^{-4}	6.70×10^{-4}	6.98×10^{-4}
Water flow rate ($m^3\,s^{-1}$)	1.46×10^{-4}	1.38×10^{-4}	1.45×10^{-4}	1.46×10^{-4}
Total flow rate ($m^3\,s^{-1}$)	8.74×10^{-4}	6.68×10^{-4}	8.15×10^{-4}	8.44×10^{-4}
Water-cut	0.167	0.206	0.178	0.173

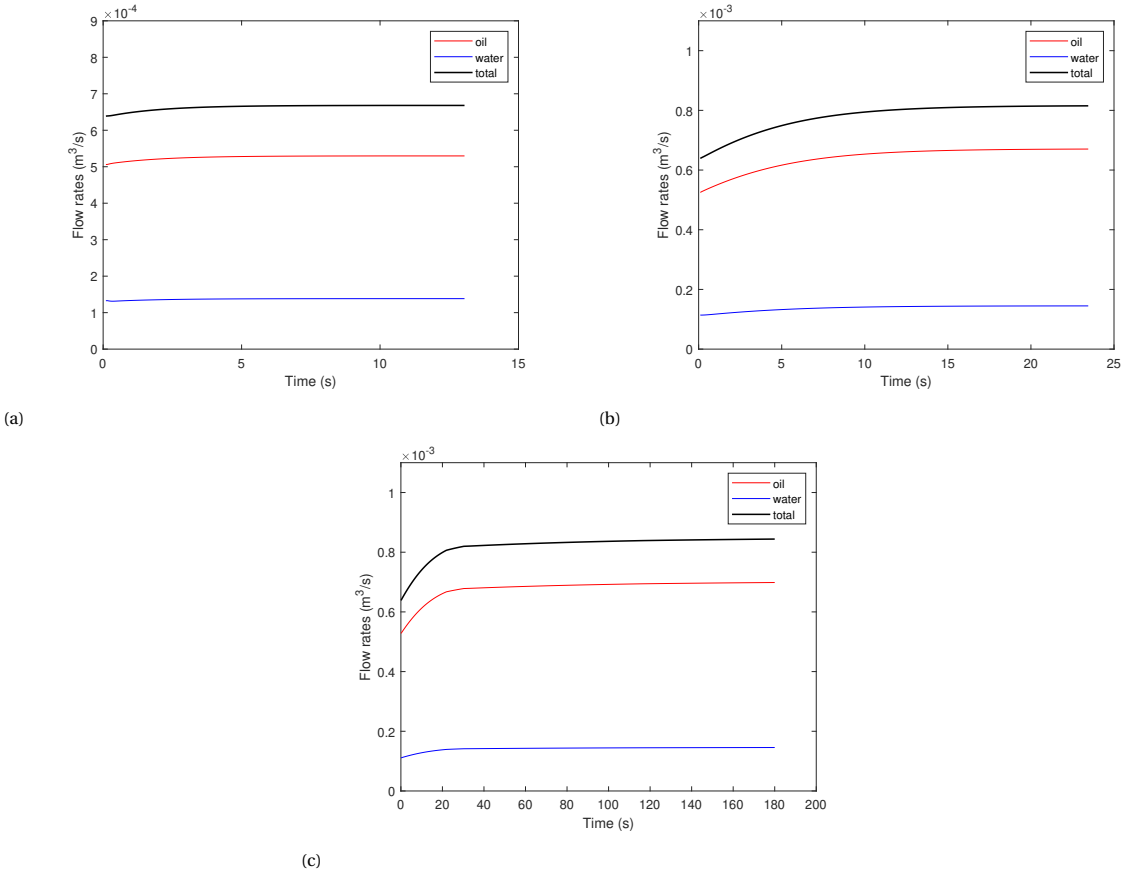

Figure 4.3: Variation of oil, water and total flow rates in time for 1D OpenFOAM simulations with (a) 100 grid cells (b) 200 grid cells (c) 400 grid cells.

with the 1D MATLAB results to verify if the turbulence is fully resolved. Only the results for the simulation with 200 and 400 grid cells respectively are compared because it is observed from Table 4.2 that the simulation with 100 grid cells does not provide comparable results. The comparison of the streamwise velocity, turbulent kinetic energy, turbulent viscosity and turbulent dissipation rate is shown in Figure 4.4. As was also observed from the prediction of flow rates, there is a slight difference between the velocity predictions of the oil for the simulations with 200 and 400 grid cells respectively and the 1D MATLAB model. The water velocity predictions are similar for all the three curves. The turbulent kinetic energy and the turbulent viscosity is negligible in the oil core. While the values for the turbulent kinetic energy and the turbulent viscosity are increasing on approaching the interface starting in the water annulus, they also are decreasing very near to the wall. The curves predicted from both the simulations are very similar to the curve predicted by the 1D MATLAB model for the turbulent kinetic energy and the turbulent viscosity. There is a slight under-prediction for the turbulent dissipation rate at the interface and at the wall by the OpenFOAM simulations as compared to the 1D MATLAB model. From these comparisons, it can be concluded that the turbulence characteristics in the water annulus are predicted accurately in OpenFOAM in both the simulations with 200 and 400 grid cells

respectively. The further 1D simulations will be performed on a mesh with 400 grid cells since the velocity predictions are slightly better for that mesh.

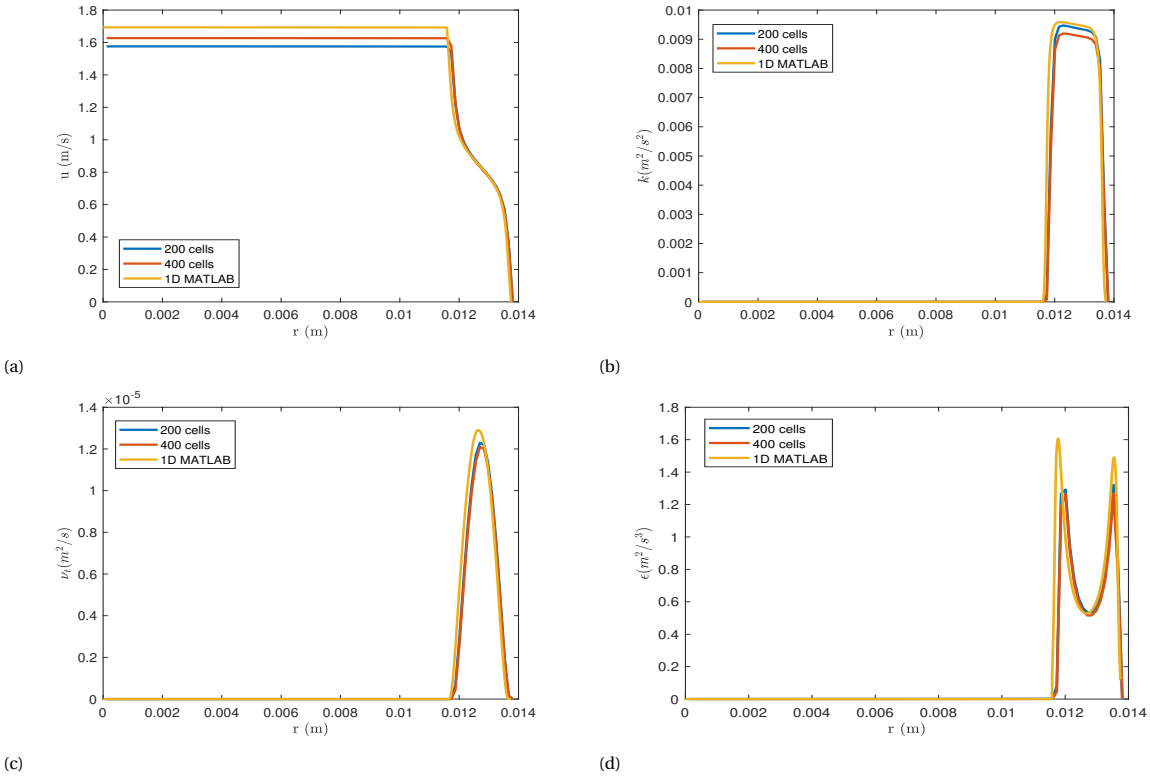

Figure 4.4: Comparison of 1D OpenFOAM results with 1D MATLAB results for (a) Streamwise velocity (b) Turbulent kinetic energy (c) Turbulent viscosity (d) Turbulent dissipation rate.

The asymptotic behaviour of the Launder-Sharma low-Re k-ε turbulence model in the inertial sublayer for wall bounded turbulent flows has been shown by Henkes [9]. These wall laws are shown in equations 4.1-4.4. Here, $\kappa = 0.431$, $C = 6,4$ and $C_\mu = 0.09$. The quantities are scaled with the kinematic viscosity of water and the friction velocity where $u^+ = u/u_\tau$, $\nu_t^+ = \nu_t/\nu_w$, $k^+ = k/u_\tau^2$ and $\epsilon^+ = \epsilon\nu_w/u_\tau^4$.

$$u^+ = \frac{1}{\kappa}\ln r^+ + C \tag{4.1}$$

$$\nu_t^+ = \kappa r^+ \tag{4.2}$$

$$k^+ = \frac{1}{\sqrt{C_\mu}} \tag{4.3}$$

$$\varepsilon^+ = \frac{1}{\kappa r^+} \tag{4.4}$$

The five different cases for different oil holdups are compared with the asymptotic wall laws. The comparison between the 1D OpenFOAM simulations with different oil holdup fraction and the asymptotic wall laws for the streamwise velocity, the turbulent kinetic energy, the turbulent viscosity and the turbulent dissipation rate in the radial direction are shown in Figure 4.5, 4.6, 4.7 and 4.8 respectively. The dotted black line represents $r^+ = 20$. The comparison with the wall laws is relevant only from $r^+ > 20$ and until the interface since that is the region where turbulence is present. As can be observed, the turbulence decreases with increasing oil holdup and the case with $\varepsilon_o = 0.91$ is completely laminar as observed from very negligible turbulent kinetic energy, turbulent viscosity and turbulent dissipation rate. For all the turbulent properties and the streamwise velocity, the predictions from the simulations are close to the asymptotic wall law between $r^+ = 20$ to $r^+ = 100$. This shows that the Reynolds number is sufficiently high for the flow to be turbulent. The case with

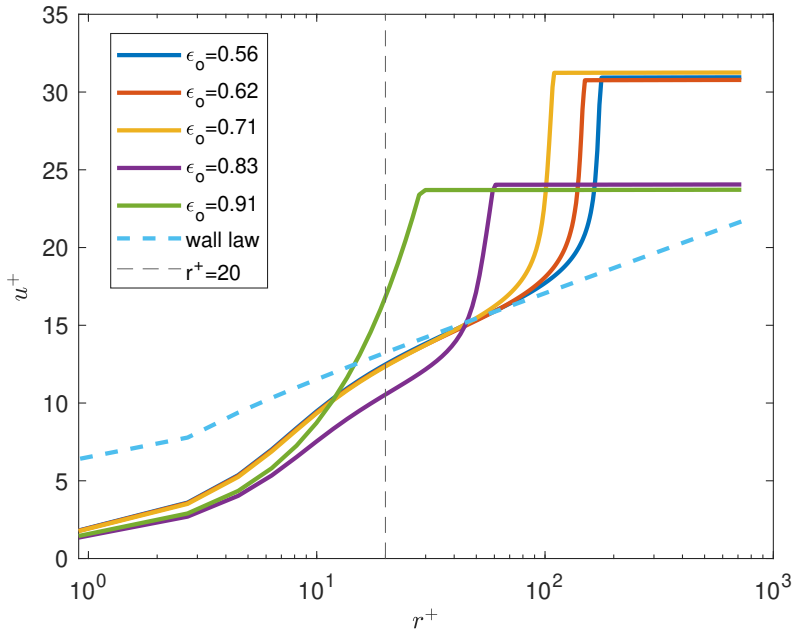

Figure 4.5: Comparison of the variation of streamwise velocity in the radial direction between the 1D OpenFOAM simulations with different oil holdup fraction and the asymptotic wall laws to analyze the turbulent scaling in the water annulus.

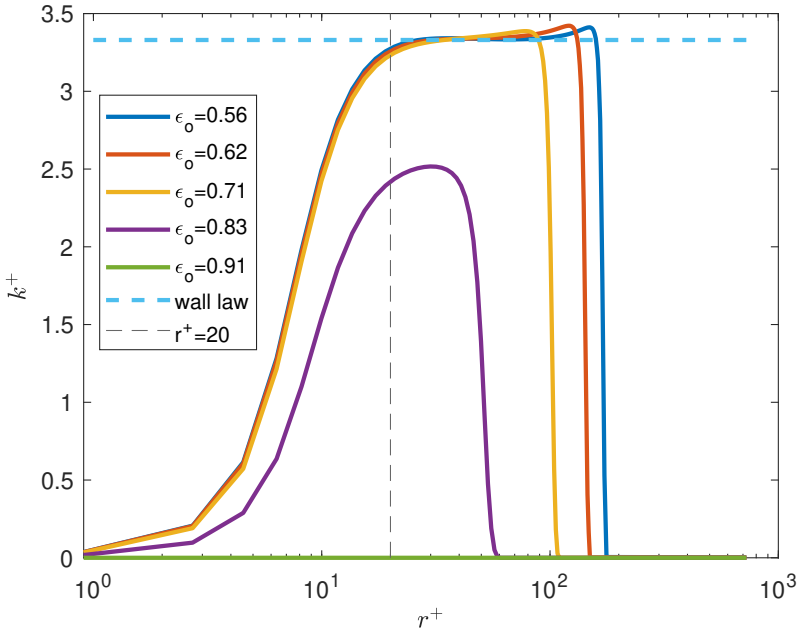

Figure 4.6: Comparison of the variation of turbulent kinetic energy in the radial direction between the 1D OpenFOAM simulations with different oil holdup fraction and the asymptotic wall laws to analyze the turbulent scaling in the water annulus.

ε_o = 0.83 has lower turbulence levels as compared to the other turbulent cases as seen from Figure 4.6. Thus, this case should be handled carefully since the flow might not be fully turbulent.

After analyzing the 1D simulations, it can be concluded that both the simulations with 200 cells and 400 cells respectively give almost similar results and the turbulence is sufficiently resolved. Thus, the 2D simulations should be done with 200 cells in radial direction.

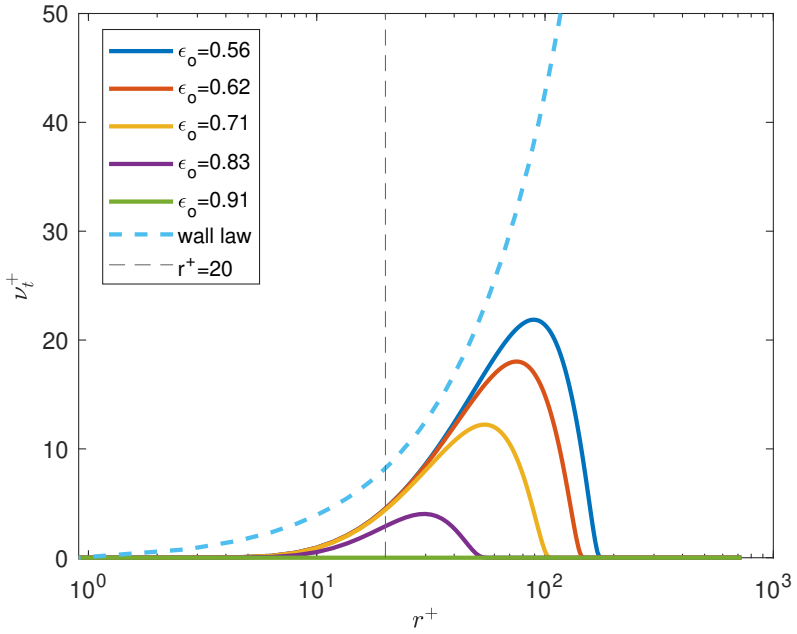

Figure 4.7: Comparison of the variation of turbulent viscosity in the radial direction between the 1D OpenFOAM simulations with different oil holdup fraction and the asymptotic wall laws to analyze the turbulent scaling in the water annulus.

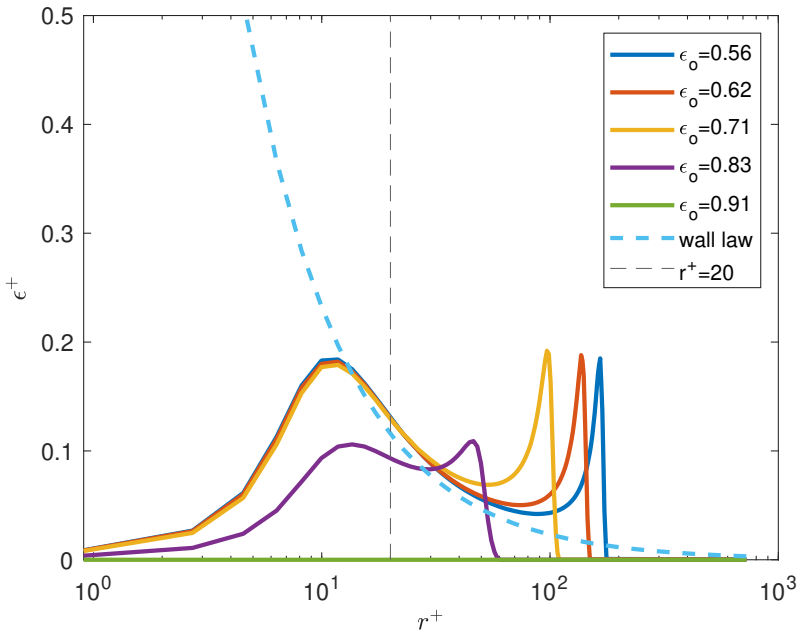

Figure 4.8: Comparison of the variation of turbulent dissipation rate in the radial direction between the 1D OpenFOAM simulations with different oil holdup fraction and the asymptotic wall laws to analyze the turbulent scaling in the water annulus.

5

Validation of the simulations

It is important to know whether the simulations done are indeed physical and give accurate predictions. There are many factors which can impact the results of the simulation. Thus, it is necessary to examine different factors like grid size and the streamwise domain length and understand if they impact the prediction of the results. To examine the effects of such factors, all the other parameters in the simulations are kept the same except the parameter whose effect is being observed. This chapter examines in detail the impact of the grid size, the streamwise domain length, presence of gravity and the effect of change in oil viscosity on the prediction of the 2D results. As the simulations are 2D, instead of 1D, waves will develop at the oil-water interface.

5.1. Grid independence study

The numerical accuracy of the grids used for the simulations can be verified by performing the same simulation on successively finer grids. The fluid properties, boundary conditions, initial conditions and the domain length are all kept the same for all the grids. If the predictions are constant for successively finer grids, then the coarsest grid among them should be chosen to perform the simulations considering the relative accuracy and computational time. The case with $\varepsilon_0 = 0.71$ is chosen to perform the grid independence study. As specified in chapter 3, the pressure drop is also imposed in addition to the oil holdup, and the total flow rate and the water-cut are obtained as the results from the simulation.

The considered case is shown to be grid independent by studying four different simulations. The pipe wall is stationary in two simulations with different grids while the pipe wall moves with the velocity of -1 $\mathrm{m\,s^{-1}}$ in the other two simulations with different grids. The moving wall configuration is studied because it gives a possibility to obtain a steady wave interface which in turn reduces the computation time. The wave velocity that was calculated from the stationary wall simulation is approximately used as the imposed wall velocity for the moving wall simulations. It has been observed that the moving wall simulation is approximately 5 times faster. The grids that are used for both the stationary wall and the moving wall simulations are 200X100 and 400X200 grid cells in the radialXstreamwise directions. A coarser mesh of 100X50 grid cells in radialXstreamwise direction is also tried. But as can be seen from Figure 5.1, the interface is not sharp and the waves break. Thus, it can be concluded that finer grids are needed.

The variation of the oil, water and total flow rates in time is shown in Figure 5.2 for all the four simulations. The simulations are carried out until 5 s to ensure that the flow rates and the water-cut reach a final fully developed state. The flow rates are calculated at a certain cross-section of the computational domain for every 0.1 s. As can be seen in Figure 5.2a and 5.2b, the oil and water flow rates show considerable fluctuations for the stationary wall simulations. These fluctuations are the result of the wave moving through the domain. The oil flow rate will have a higher value when the wave crest is at the cross section where the flow rates are calculated while it has a lower value when the wave trough is at the same cross section. The water flow rate fluctuates in the opposite way: lower at the wave crest and higher at the wave trough. It can also be seen that the fluctuations are lower for the moving wall simulations as compared to the stationary wall simulations. This is due to the fact that the wave travels very slowly for the moving wall simulation as it is ensured that the

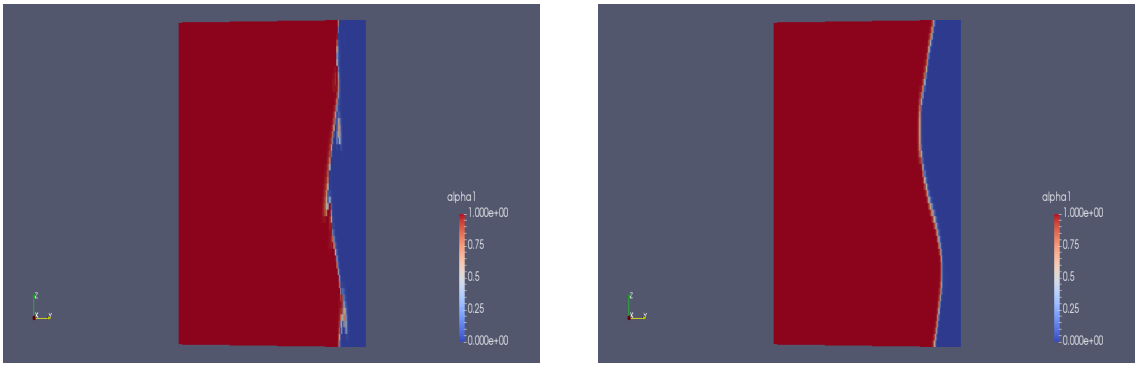

(a) (b)

Figure 5.1: Breaking of the wave structure for the simulations with (a) stationary wall and 100X50 grid cells (b) moving wall and 100X50 grid cells.

imposed wall velocity should be approximately the same as the wave velocity. Despite the fluctuations in the oil and water flow rates, the total flow rate reaches a final value for all the four simulations. Thus, it can be said that the simulations are fully developed with respect to the output values.

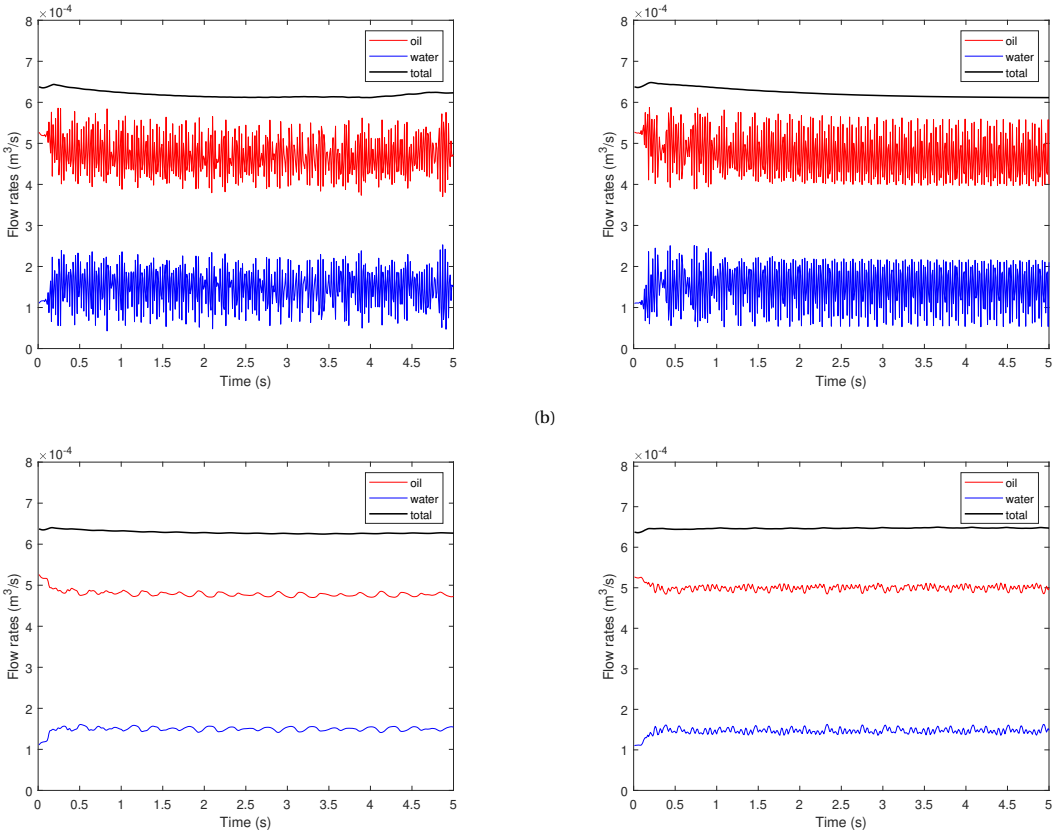

(a) (b)

(c) (d)

Figure 5.2: Variation of oil, water and total flow rates in time for the simulations with (a) stationary wall and 200X100 grid cells (b) stationary wall and 400X200 grid cells (c) moving wall and 200X100 grid cells (d) moving wall and 400X200 grid cells.

The wave structure for the four different simulations can be seen in Figure 5.3. It was observed that the wave structure in the coarser mesh for the stationary wall simulation was different from the wave structure in the other three simulations. The wave structure for all the other three cases looks similar and thus further analysis is done to determine the grid independence.

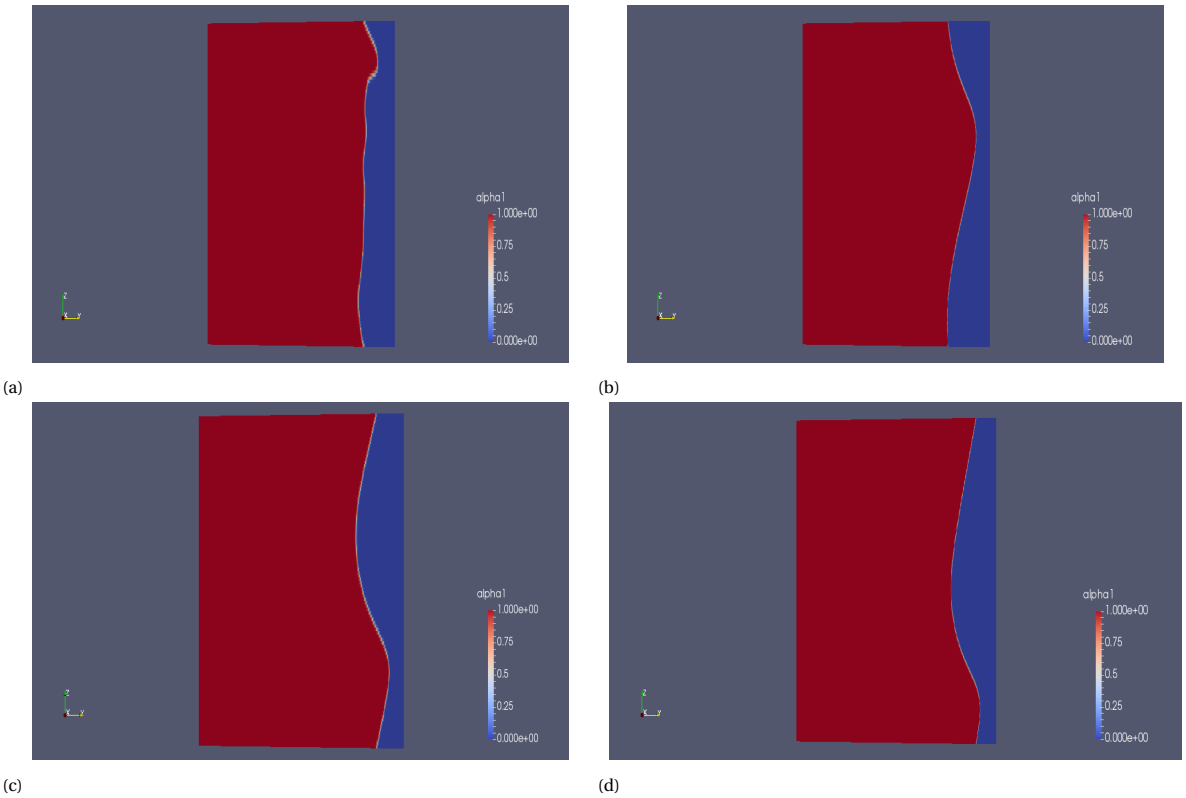

Figure 5.3: Wave structure for the simulations with (a) stationary wall and 200X100 grid cells (b) stationary wall and 400X200 grid cells (c) moving wall and 200X100 grid cells (d) moving wall and 400X200 grid cells.

The output of all the four simulations is summarised in Table 5.1. As it is a grid independence test, the imposed conditions are the same for all four cases. It can also be seen that it has been ensured that the r^+ value for all the four grids is less than 1 so that the viscous sub-layer is resolved sufficiently. The oil flow rate, water flow rate, the total flow rate and the water-cut obtained are similar for all the four simulations. The difference in the oil, water and total flow rates for the moving wall simulations is 2.8% between both the grids while the difference in the water-cut is 1.2%. The difference in the flow rates and the water-cut for the stationary wall simulations is very small. The hold-up ratio, the measure of the apparent slip velocity between the oil core and the water annulus, is also similar for all the four simulations. The friction factor is slightly lower for the moving wall simulations as compared to the stationary wall simulations. The maximum turbulence viscosity ratio gives an idea about the turbulence levels in the domain. It is the ratio of the maximum turbulence viscosity in the domain and the water kinematic viscosity. This ratio is larger for the moving wall simulations and hence there is a larger turbulence level inside the simulation domain. The turbulence viscosity ratio is similar for both the grids for the moving wall simulations. The values summarised in Table 5.1 show that the results from the different meshes are similar though the full asymptotic decay of numerical error is not observed. Also, there is not much difference between the stationary wall simulation and the moving wall simulation.

The time signal analysis has been carried out for the stationary wall simulations since it is necessary to analyse the predictions in time as the wave moves inside the domain. It is similar to inserting a probe inside the flow and getting the readings at different times. Since the wall is stationary, this shows the time dependence of the flow properties. The water layer thickness and the turbulence viscosity ratio for both the grids of the stationary wall simulations are compared in Figure 5.4. The time signal analysis is done after a simulation time of 5s ensuring that the flow is fully developed as seen from Figure 5.2. As we can see in Figure 5.4, the water layer thickness and the maximum turbulence viscosity for the 400X200 grid show a steady wave pattern which means that all the unsteadiness in the flow has disappeared. In contrast to this the wave pattern for the 200X100 grid does not show a steady wave pattern which means that there is still some unsteadiness left in the flow. The water layer thickness for both the grids looks similar while there is a small difference in the

Table 5.1: Comparison of the results from the stationary wall 200X100 grid, stationary wall 400X200 grid, moving wall 200X100 grid and moving wall 400X200 grid for the grid independence test.

	Stationary wall 200X100	**Stationary wall 400X200**	**Moving wall 200X100**	**Moving wall 400X200**
Imposed pressure drop ($\mathrm{Pa\,m^{-1}}$)	9945.6	9945.6	9945.6	9945.6
Imposed oil holdup	0.71	0.71	0.71	0.71
Oil flow rate ($\mathrm{m^3\,s^{-1}}$)	4.69×10^{-4}	4.66×10^{-4}	4.77×10^{-4}	4.92×10^{-4}
Water flow rate ($\mathrm{m^3\,s^{-1}}$)	1.47×10^{-4}	1.47×10^{-4}	1.50×10^{-4}	1.53×10^{-4}
Total flow rate ($\mathrm{m^3\,s^{-1}}$)	6.16×10^{-4}	6.13×10^{-4}	6.27×10^{-4}	6.45×10^{-4}
Water-cut	0.239	0.240	0.239	0.236
Hold-up ratio	1.30	1.29	1.30	1.32
Friction factor	0.00511	0.00516	0.00502	0.00467
Maximum turbulence viscosity ratio	14.7	17.0	19.9	20.1
r^+ value at the first inner grid point	0.93	0.46	0.93	0.46

maximum turbulence viscosity ratio for both the grids which was also observed in Table 5.1.

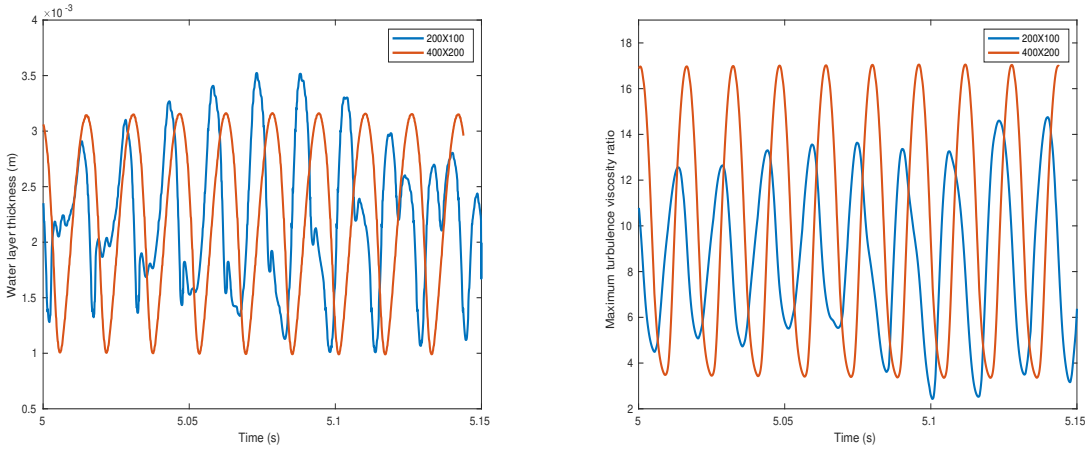

(a) (b)

Figure 5.4: Comparison of the (a) Water layer thickness (b) Maximum turbulence viscosity ratio in time for the fully developed stationary wall simulations with 200X100 and 400X200 grid.

Since the moving wall case essentially means that the wave should be steady, the spatial dependence of the waves at the interface is analyzed. For this, the water layer thickness and the maximum turbulence viscosity ratio for the moving wall simulations is analysed with respect to the streamwise coordinate. Figure 5.5 shows the spatial dependence of the water layer thickness and the maximum turbulence viscosity ratio for the moving wall simulations. The difference between the predictions, from both the grids, of the water layer thickness and the maximum turbulence viscosity ratio is very small. This shows that the turbulence has been properly resolved for both the grids as well as the interface is predicted accurately by the coarser grid.

Normally, grid independence tests are done by comparing the velocity and the volume fraction in the radial direction for all the different grids. Kim and Choi [15] define the mean water volume fraction as shown in equation 5.1. Here, $\bar{\psi}=1$ denotes the water region while $\bar{\psi}=0$ denotes the oil region. The mean streamwise velocity are defined as shown in equation 5.2 and 5.3 for water and oil respectively.

$$\bar{\psi}(r)=\frac{\iiint \psi(z,r,\theta,t)\mathrm{d}\theta\mathrm{d}z\,\mathrm{d}t}{\iiint \mathrm{d}\theta\mathrm{d}z\,\mathrm{d}t} \tag{5.1}$$

$$\bar{u}_w(r)=\frac{\iiint u(z,r,\theta,t)\psi(z,r,\theta,t)\mathrm{d}\theta\mathrm{d}z\,\mathrm{d}t}{\iiint \psi(z,r,\theta,t)\mathrm{d}\theta\mathrm{d}z\,\mathrm{d}t} \tag{5.2}$$

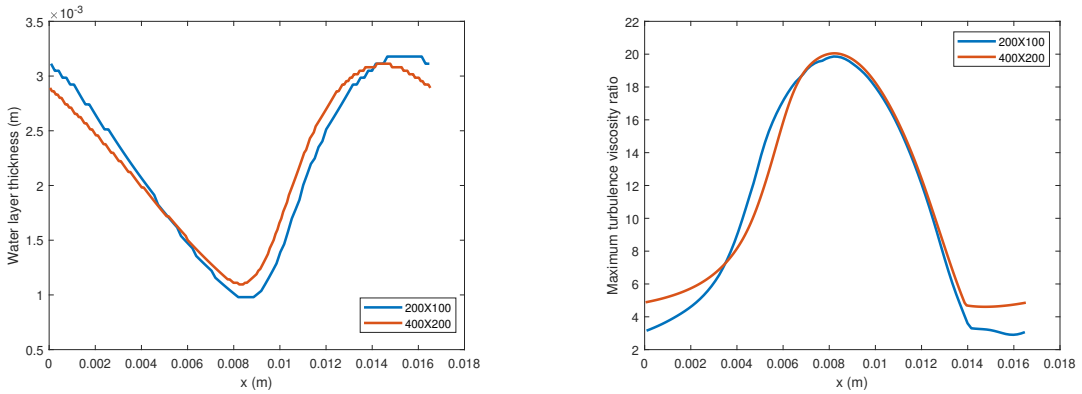

(a) (b)

Figure 5.5: Comparison of the (a) Water layer thickness (b) Maximum turbulence viscosity ratio in space for the fully developed moving wall simulations with 200X100 and 400X200 grid.

$$\bar{u}_o(r) = \frac{\iiint u(z,r,\theta,t)(1-\psi(z,r,\theta,t))\mathrm{d}\theta\mathrm{d}z\,\mathrm{d}t}{\iiint (1-\psi(z,r,\theta,t))\mathrm{d}\theta\mathrm{d}z\,\mathrm{d}t} \tag{5.3}$$

Figure 5.6 shows the comparison of the mean water volume fraction and the scaled mean streamwise velocity for all the four grids. Since these are 2D simulations, the tangential direction has been disregarded from equations 5.1-5.3. The graphs are comparable for all the grids except the stationary wall 200X100 grid for which the mean water volume fraction is not predicted accurately. Thus, the mean water volume fraction and the mean streamwise velocity are accurately predicted by the coarser grid for the moving wall simulation.

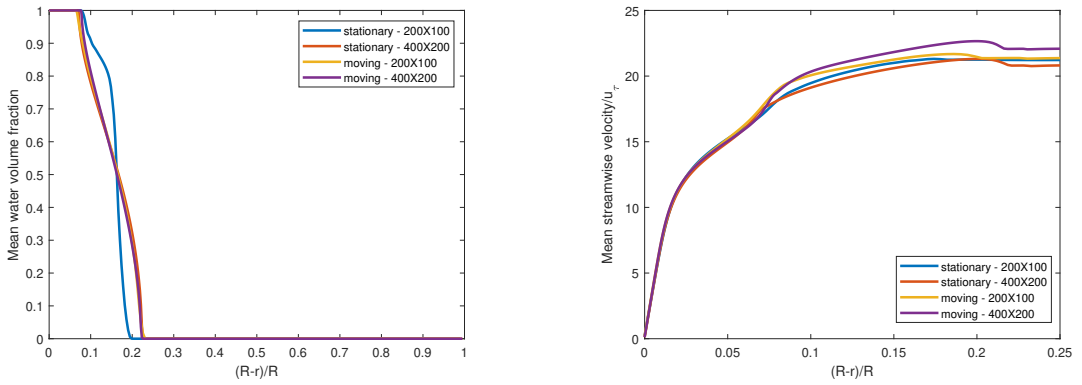

(a) (b)

Figure 5.6: Comparison of the (a) Mean water volume fraction (b) Scaled mean streamwise velocity for the simulations with stationary wall and 200X100 grid, stationary wall and 400X200 grid, moving wall and 200X100 grid, and moving wall and 400X200 grid.

To conclusively say that the simulations are grid independent, it is also necessary to analyse the wave characteristics of the waves from all the four simulations. It was ensured with the selection of the streamwise domain length that there will be only one wave inside the domain. Thus, the wavelength of the wave for all four simulations will be 0.01656 m as also mentioned in Table 5.2. The wave amplitude is calculated as shown in equation 5.4 where δ represents the water layer thickness and the overbar denotes the time-averaged value at a certain streamwise location. The amplitude is defined in such a way that it gives half the difference between the maximum and minimum value for the case of a pure sinus.

$$A = \sqrt{2\overline{\left(\delta - \bar{\delta}\right)^2}} \tag{5.4}$$

The wave frequency can be obtained from the time signal analysis by calculating the number of fluctuations in the simulated time. The wave velocity is the product of the wavelength and the wave frequency. It has also

been ensured that the moving wall simulation results are converted to the stationary reference frame before calculating the wave characteristics. As can be seen from Table 5.2, there is only about 2-5% difference in the values for all the four simulations. Thus, the wave characteristics are accurately predicted by the coarser grids.

Table 5.2: Comparison of the wave characteristics for the simulations with stationary wall and 200X100 grid, stationary wall and 400X200 grid, moving wall and 200X100 grid, and moving wall and 400X200 grid.

	Stationary wall 200X100	**Stationary wall 400X200**	**Moving wall 200X100**	**Moving wall 400X200**
Wave velocity ($m s^{-1}$)	1.053	1.042	1.082	1.106
Wave length (m)	0.01656	0.01656	0.01656	0.01656
Wave frequency (Hz)	63.6	62.9	65.4	66.8
Wave amplitude (m)	0.00087	0.00106	0.00108	0.00096

Since the wave velocity is independent of the water layer thickness, the temporal dependence can be converted to the spatial dependence for the stationary wall simulations. This conversion allows the comparison of all four grids on a graph with a varying streamwise coordinate. The comparison for the water layer thickness and the maximum turbulence viscosity for all four grids is shown in Figure 5.7 and Figure 5.8 respectively. As also observed in the Figure 5.3, because of the different wave shape, the stationary wall 200X100 grid simulation does not give accurate result. The maximum turbulence viscosity ratio is under-predicted while the water layer thickness is not accurately predicted by the stationary wall 200X100 grid as shown in Figure 5.7 and Figure 5.8 respectively. The prediction of the water layer thickness for the three simulations other than the stationary 200X100 grid simulation is similar. The maximum turbulence viscosity ratio is lower for the stationary 400X200 grid as compared to the moving wall simulations. The water layer thickness and the maximum turbulence viscosity ratio for both the moving wall grids is comparable.

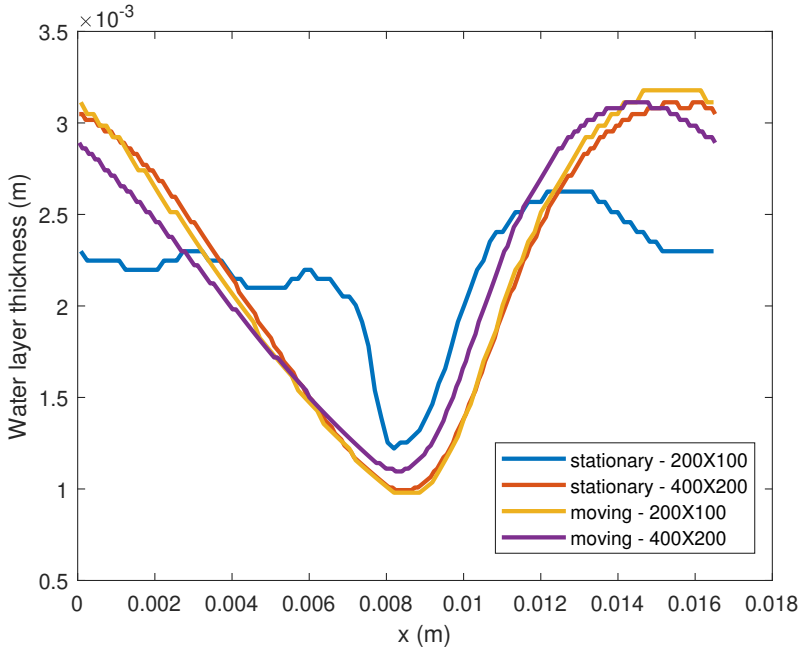

Figure 5.7: Comparison of the water layer thickness for the simulations with stationary wall and 200X100 grid, stationary wall and 400X200 grid, moving wall and 200X100 grid, and moving wall and 400X200 grid.

Thus, from the analysis done of all the four different simulations, it can be concluded that there is not much difference between the predictions of the stationary wall and the moving wall simulations with respect to the simulation outputs such as the flow rates, water-cut and the wave characteristics. The turbulence level

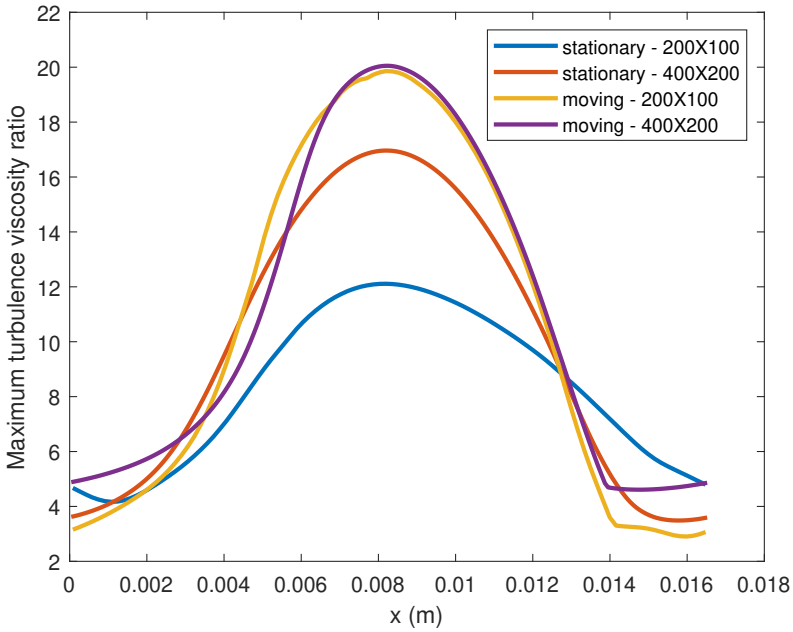

Figure 5.8: Comparison of the maximum turbulence viscosity ratio for the simulations with stationary wall and 200X100 grid, stationary wall and 400X200 grid, moving wall and 200X100 grid, and moving wall and 400X200 grid.

is slightly higher for the moving wall simulations. Thus, it is advantageous to use the moving wall configuration since it takes less computational time as compared to the stationary wall simulations. It can also be concluded that there is not much difference between the predictions from the two grids used in the moving wall simulations, which concludes the grid independence test. Thus, it is better to use the coarser mesh as it takes less computational time as compared to the finer grid. Thus, for this thesis 200X100 grid and a moving wall with a wall velocity of -1 $\mathrm{m\,s^{-1}}$ will be used unless specified otherwise.

5.2. Dependence on streamwise domain length

Since the streamwise domain length has been selected by trial and error such that only one wave exist in the domain, it is necessary to validate the simulations with respect to the streamwise domain length so that it can be concluded that the streamwise length considered does not affect the predictions. To study the dependence on the streamwise domain length, three simulations are done. The oil holdup fraction and the imposed pressure drop are fixed as 0.71 and 9945.6 $\mathrm{Pa\,m^{-1}}$ respectively. The streamwise domain base-length (BL) is considered as 0.01656 m, which is $1.2R$, as was used in the simulations for the grid independence test. The other two simulations have streamwise domain length as 0.5BL and 1.5BL. All other conditions remain the same. There are 200X100 grid cells used for the base-length while 200X50 and 200X150 grid cells are used for the 0.5BL and 1.5BL simulations respectively so that the mesh used is uniform. The simulations are performed with the moving wall configuration with the wall velocity of -1 $\mathrm{m\,s^{-1}}$.

All the three simulations are performed until 5 s simulation time to ensure that they are fully developed. The variation of oil, water and total flow rates in time for the BL simulation is already seen in Figure 5.2c. The variation of the flow rates in time for the 0.5BL and 1.5BL are as shown in Figure 5.9. As already stated, because of the moving wall configuration, the fluctuations in the oil and water flow rates are small. The total flow rate has reached a steady value which means that the flow is fully developed.

The wave structure for the 0.5BL and 1.5BL simulations are as shown in Figure 5.10. The number of waves in the domain for the 1.5BL simulation is two. The wave structure for the BL simulation, shown in Figure 5.3c, is different when compared with the wave structure from the 0.5BL simulation. The wave structure for the 0.5BL simulation has a smaller amplitude which can also be seen in Table 5.4.

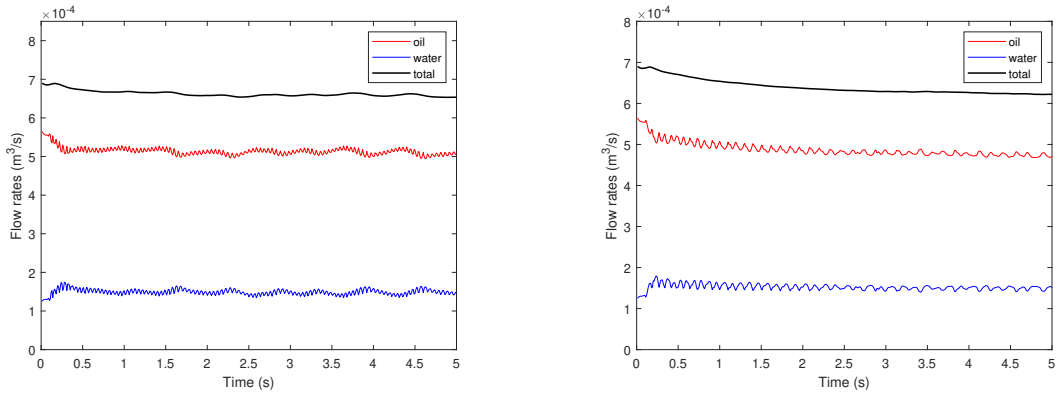

(a) (b)

Figure 5.9: Variation of oil, water and total flow rates in time for the simulations with (a) 0.5BL (b) 1.5BL.

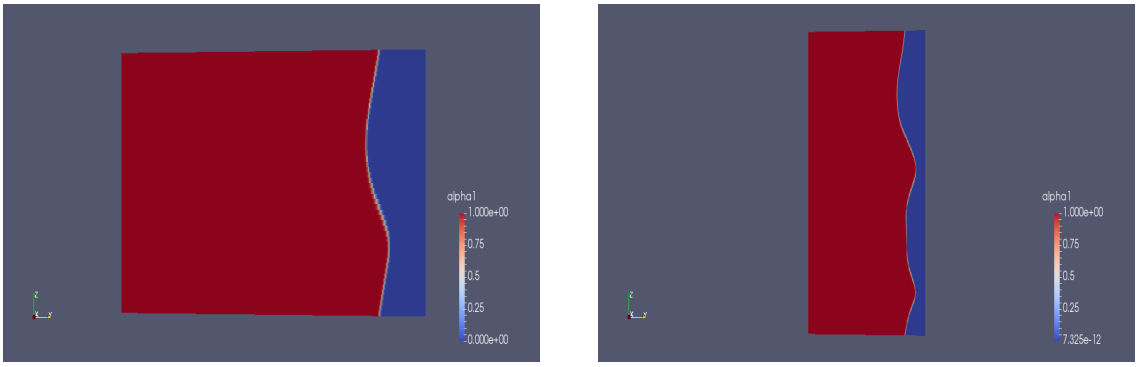

(a) (b)

Figure 5.10: Wave structure for the simulations with (a) 0.5BL (b) 1.5BL.

Table 5.3: Comparison of the results from the simulations with 0.5BL, BL and 1.5BL to analyze the influence of a change in streamwise domain length.

	0.5BL	**BL**	**1.5BL**
Imposed pressure drop ($\mathrm{Pa\,m^{-1}}$)	9945.6	9945.6	9945.6
Imposed oil holdup	0.71	0.71	0.71
Oil flow rate ($\mathrm{m^3\,s^{-1}}$)	5.10×10^{-4}	4.77×10^{-4}	4.74×10^{-4}
Water flow rate ($\mathrm{m^3\,s^{-1}}$)	1.47×10^{-4}	1.50×10^{-4}	1.48×10^{-4}
Total flow rate ($\mathrm{m^3\,s^{-1}}$)	6.57×10^{-4}	6.27×10^{-4}	6.22×10^{-4}
Water-cut	0.224	0.239	0.239
Hold-up ratio	1.42	1.30	1.31
Friction factor	0.00464	0.00502	0.00511
Maximum turbulence viscosity ratio	18.3	19.9	20.2

The analyzed results for the three different streamwise domain length simulation are given in Table 5.3. The first observation is that the results for the BL and the 1.5BL simulation are almost the same and there is not much difference between the predictions which means that the streamwise domain length chosen does not impact the prediction of the results. But if a lower streamwise domain length would have been chosen, the results would have been different as observed from the predictions of the 0.5BL simulation. The total flow rate for the 0.5BL simulation is 5% higher than the BL and the 1.5BL simulations. There is a difference in the prediction of the hold-up ratio, friction factor and the maximum turbulence viscosity ratio as well for the 0.5BL simulation. Thus, it is observed that the streamwise domain length chosen for the BL simulation is sufficient.

Since these are moving wall simulations, the spatial dependence is analyzed. Figure 5.11 shows the variation of the water layer thickness and the maximum turbulence viscosity ratio in the streamwise direction. Since the streamwise domain length of each simulation is different, the x-coordinate has been scaled with L, which is the streamwise domain length for each simulation, so that the comparison is easy. As can be observed, there is visible difference in the prediction of the 0.5BL simulation and the BL simulation. Also, the 1.5BL simulation has two waves in the domain and it seems that one wave follows the prediction of the 0.5BL simulation and the other follows the prediction of the BL simulation. This is because the wave requires a certain streamwise length to develop. When a certain streamwise length is reached for the wave to develop fully, a new wave will start to develop. Hence, this gives the presence of two waves in the 1.5BL simulation. Thus, it can be concluded from the spatial dependence analysis as well that the domain length for the BL simulation is sufficient.

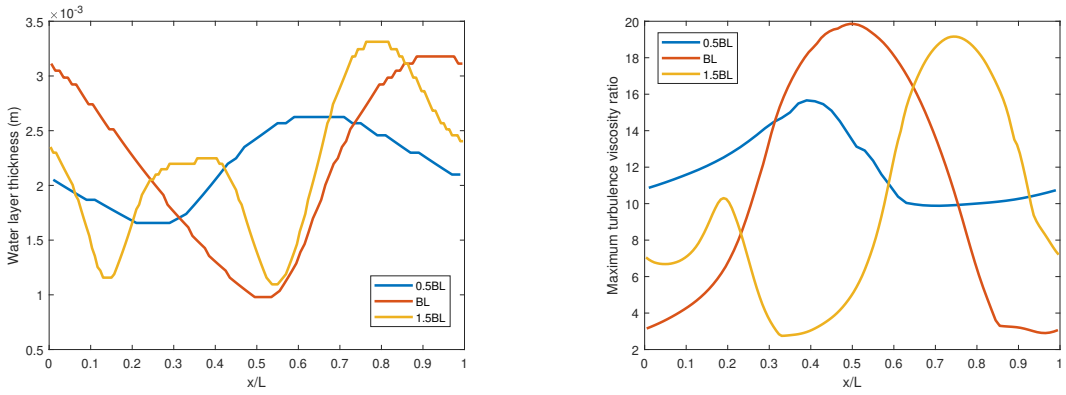

(a) (b)

Figure 5.11: Comparison of the (a) Water layer thickness (b) Maximum turbulence viscosity ratio for the fully developed simulations with streamwise domain length of 0.5BL, BL and 1.5BL.

The wave characteristics are also analysed for all the three simulations and are listed in Table 5.4. All the moving wall simulations are converted to the stationary reference frame and then analysed. The wavelength is the streamwise length of the domain for the 0.5BL and the BL simulation since only one wave is present inside the domain. There are two waves present inside the domain for 1.5BL simulation and thus the average wavelength will be half the streamwise domain length. The wave amplitude and the wave frequency for the 1.5BL simulation is the average of both the waves. Hence, the value is between the prediction for the 0.5BL simulation and the BL simulation since, as already established, the 1.5BL simulation contains waves similar to both the cases. This can also be observed from the individual wave amplitudes for the two waves inside the simulation domain for the 1.5BL case. The wave amplitude for the smaller wave, with wavelength 0.00596 m, is 0.00075 m while the wave amplitude for the larger wave, with wavelength 0.01888 m, is 0.00106 m. The wave velocity is slightly over-predicted by the 0.5BL simulation while the wave velocity for the BL and the 1.5BL simulations is the same. Thus, the wave characteristics are also accurately predicted by the BL simulation.

Table 5.4: Comparison of the wave characteristics for the fully developed simulations with streamwise domain length of 0.5BL, BL and 1.5BL.

	0.5BL	**BL**	**1.5BL**
Wave velocity (ms^{-1})	1.162	1.082	1.082
Wave length (m)	0.00828	0.01656	0.01242
Wave frequency (Hz)	140.34	65.4	87.12
Wave amplitude (m)	0.00048	0.00108	0.00093

Since the streamwise length of the domain is different for all three simulations, it is imperative to examine the radial variation of the flow properties. To analyze the radial dependence, the mean water volume fraction and the scaled mean streamwise velocity are plotted, as defined by Kim and Choi [15], in Figure 5.12. These

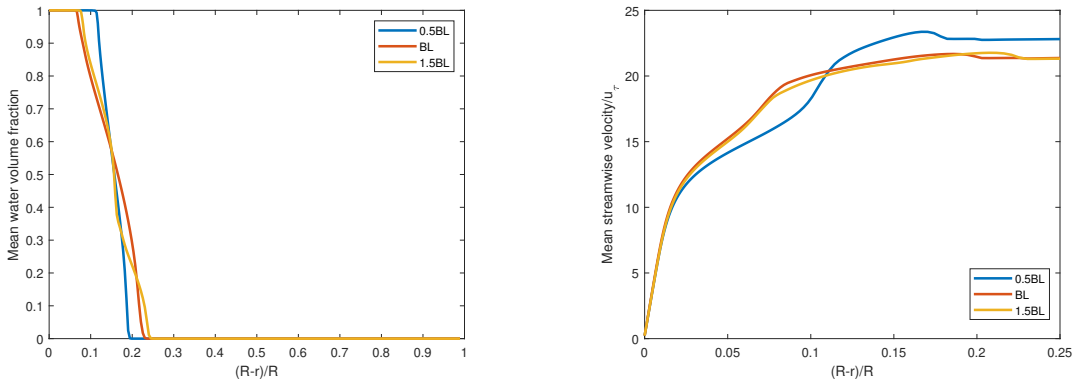

(a) (b)

Figure 5.12: Comparison of the (a) Mean water volume fraction (b) Scaled mean streamwise velocity for the fully developed simulations with streamwise domain length of 0.5BL, BL and 1.5BL.

results also support the observation that the 0.5BL simulation gives slightly different predictions as compared to the Bl and 1.5BL simulations. Also, it can be noticed in the mean water volume fraction graph, the 1.5BL simulation curve is similar to BL curve for a particular section while it is similar to the 0.5BL curve for a similar section. This also supports the observation that one wave in the 1.5BL domain is similar to 0.5BL simulation and the other is similar to the BL simulation.

Thus, from the analysis done, it can be concluded that the streamwise domain length (BL) used in this thesis does not impact the prediction of the results and it is sufficient to simulate one full wave in the simulation domain. Hence, the streamwise domain length of 0.01656 m is used for all the further simulations in this thesis.

5.3. 2D simulation without gravity

The oil core usually becomes eccentric in a horizontal flow configuration for core-annular flow. This is different from the vertical flow configuration where the core will always remain concentric because the gravity is in the direction of the flow while it is perpendicular to the direction of flow for horizontal flow configuration. The difference between the vertical and horizontal 2D simulations is the presence of gravity for the vertical flow configuration. Thus, it is interesting to know the effect of gravity on the prediction of the results (for the flow properties considered in this thesis).

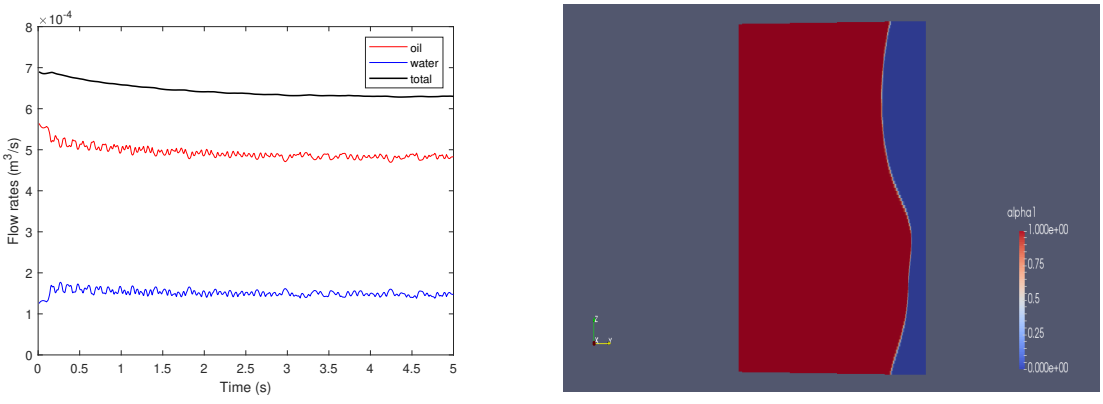

(a) (b)

Figure 5.13: (a) Variation of oil, water and total flow rates in time (b) Wave structure for simulation without gravity

The imposed pressure drop is lower in the simulation without gravity as compared to the simulation with

Table 5.5: Comparison of results between 2D simulations with and without gravity.

	With gravity	**Without gravity**
Imposed pressure drop ($Pa\,m^{-1}$)	9945.6	400
Imposed oil holdup	0.71	0.71
Oil flow rate ($m^3\,s^{-1}$)	4.77×10^{-4}	4.79×10^{-4}
Water flow rate ($m^3\,s^{-1}$)	1.50×10^{-4}	1.48×10^{-4}
Total flow rate ($m^3\,s^{-1}$)	6.27×10^{-4}	6.31×10^{-4}
Water-cut	0.239	0.235
Hold-up ratio	1.30	1.33
Friction factor	0.00502	0.00496
Maximum turbulence viscosity ratio	19.9	18.9

gravity because the gravitational pressure drop is neglected for the simulation without gravity. The variation of the oil, water and total flow rates is as shown in Fig 5.13a. This simulation, without gravity, is also performed until 5 s to ensure that it is fully developed. The wave structure for the simulation without gravity is shown in Figure 5.13b which is similar to the wave structure for the simulation with gravity as shown in Figure 5.3c.

The results obtained from the simulation without gravity are compared with the results obtained from the simulation with gravity in Table 5.5. The predictions for both the simulations are similar for all the parameters. Thus, this shows that there are no significant differences between the simulation without gravity and the simulation with gravity.

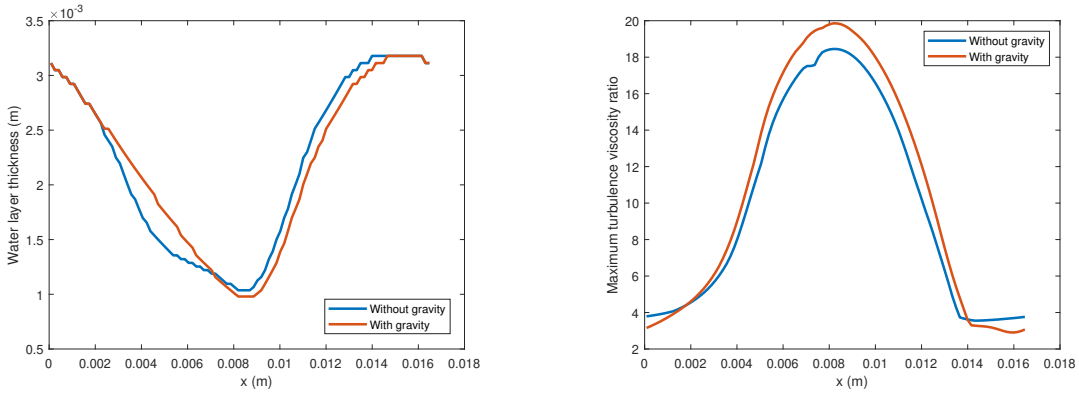

(a) (b)

Figure 5.14: Comparison of the (a) Water layer thickness (b) Maximum turbulence viscosity ratio for the fully developed simulations with and without gravity.

Table 5.6: Comparison of the wave characteristics for simulations with and without gravity.

	With gravity	**Without gravity**
Wave velocity ($m\,s^{-1}$)	1.082	1.073
Wave length (m)	0.01656	0.01656
Wave frequency (Hz)	65.4	64.79
Wave amplitude (m)	0.00108	0.00116

The spatial dependence is analyzed to study the differences in the water layer thickness and the maximum turbulence viscosity ratio as shown in Figure 5.14. The curves are similar for both the simulations. Thus, there is no significant difference between the simulations with and without gravity for the mean water layer and the maximum turbulence viscosity ratio predictions.

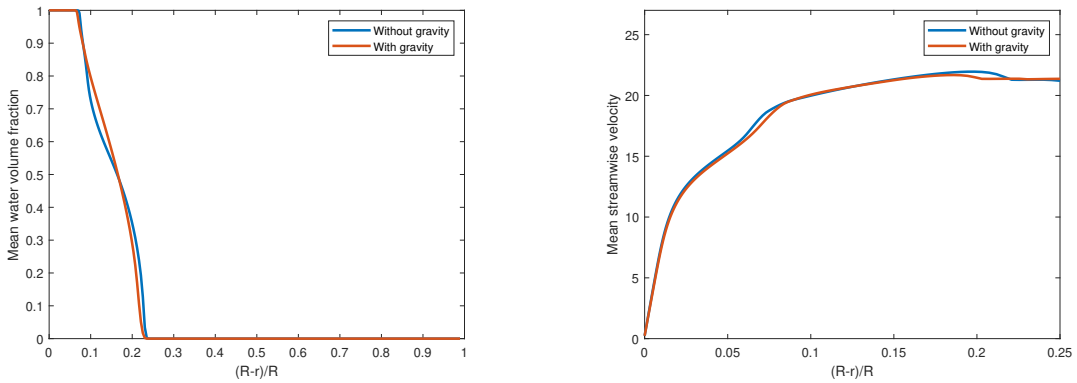

(a) (b)

Figure 5.15: Comparison of the (a) Mean water volume fraction (b) Scaled mean streamwise velocity for fully developed simulations with and without gravity.

The wave characteristics, the mean water volume fraction and the mean streamwise velocity are compared for the simulations with and without gravity as shown in Table 5.6, Figure 5.15a and Figure 5.15b, respectively. All the values for the wave characteristics are similar for both the simulations. The mean water volume fraction and the mean streamwise velocity predictions are also similar. Thus, it can be concluded that there are no significant differences between the predictions of the simulations with and without gravity.

5.4. Different oil viscosities

Since the oil viscosity used in this thesis is lower than the oil viscosity used by Kim and Choi [15] (namely 0.745 Pas versus 17.6 Pas) for their simulations, it is necessary to investigate the effect of oil viscosity on the predictions for core-annular flow. The oil holdup fraction is kept fixed as 0.71 and all other properties are kept the same except for the oil viscosity. The effect of changing oil viscosity is observed by studying three different simulations and comparing it with the base case having oil viscosity as 0.745 Pa s. There are two simulations carried out with higher oil viscosity, 0.963 Pa s and 1.926 Pa s while one simulation with lower oil viscosity of 0.456 Pa s is also performed. If the oil viscosity was increased further, oil fouling of the pipe wall was observed. The grid used for all the simulations is 200X100 except for the lowest oil viscosity (i.e. 0.456 Pa s) simulation, in which case it is 300X150.

The variation of oil, water and total flow rates for the three different oil viscosity simulations is shown in Figure 5.16. These simulations are also carried out until 5 s to ensure that they are fully developed. The wave structure for the three simulations can be seen in Figure 5.17. It is observed that there are two waves present in the simulation with the lowest oil viscosity while there is one wave present in all the other simulations.

The results obtained from the simulations for four different oil viscosities are tabulated in Table 5.7. The oil holdup fraction and the imposed pressure drop are the same for all four simulations. It is observed that there is just a minor difference in the flow rates for all four simulations. The water-cut increases slightly with increasing oil viscosity while the hold-up ratio decreases with increasing oil viscosity. These follow the same trends as observed in the literature. The friction factor does not show much deviation for all the four simulations. The maximum turbulence viscosity ratio increases with increasing oil viscosity but is lower for the simulation with the highest oil viscosity. Thus, it can be concluded that for the range of the ratio of oil viscosity to water viscosity (viscosity ratio) considered, the simulation outputs do not show much deviation and it can be extrapolated to the higher oil viscosity simulations done by Kim and Choi [15] by assuming the flow rates to be constant.

The spatial dependence analysis for the simulations with different oil viscosities is shown in Figure 5.18. It is observed that the maximum turbulence viscosity ratio and the water layer thickness curves for simulation with oil viscosity 0.745 Pa s and 0.963 Pa s are almost the same. This can be expected as there is not much difference between the oil viscosity for both the simulations. The curve for the lowest oil viscosity simulation has two peaks which is due to the presence of two waves in the simulation domain. The maximum turbulence

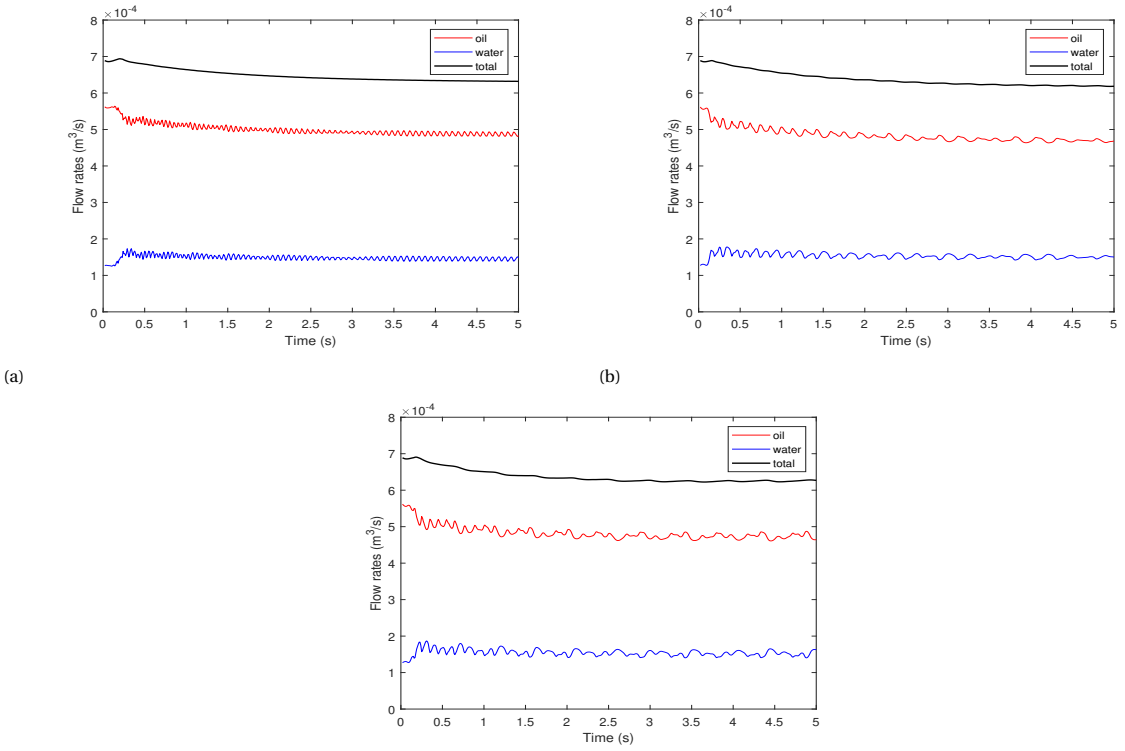

Figure 5.16: Variation of oil, water and total flow rates for the simulations with oil viscosity (a) 0.456 Pas (b) 0.963 Pas (c) 1.926 Pas.

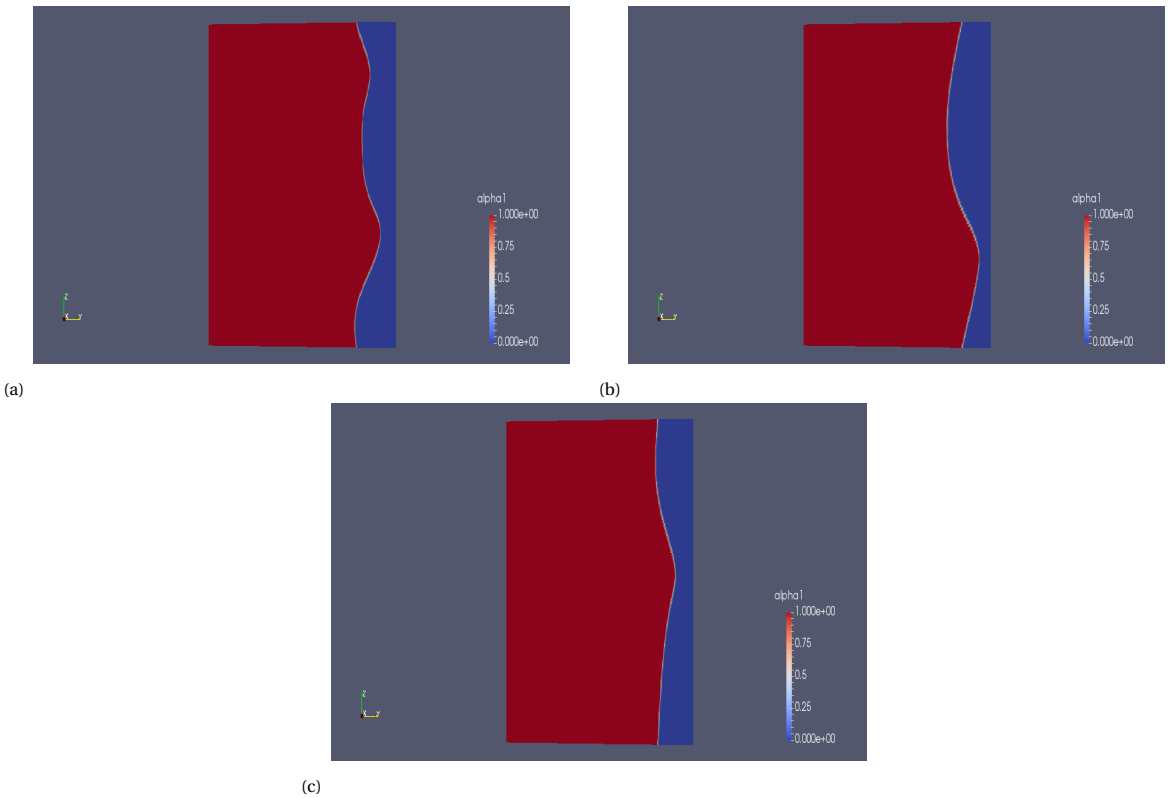

Figure 5.17: Wave structure for the simulations with oil viscosity (a) 0.456 Pas (b) 0.963 Pas (c) 1.926 Pas.

Table 5.7: Comparison of results for the simulations with oil viscosity of 0.456 Pas, 0.745 Pas, 0.963 Pas and 1.926 Pas.

Oil viscosity (Pas)	**0.456**	**0.745**	**0.963**	**1.926**
Imposed pressure drop ($Pa\,m^{-1}$)	9945.6	9945.6	9945.6	9945.6
Imposed oil holdup	0.71	0.71	0.71	0.71
Oil flow rate ($m^3\,s^{-1}$)	4.88×10^{-4}	4.78×10^{-4}	4.69×10^{-4}	4.76×10^{-4}
Water flow rate ($m^3\,s^{-1}$)	1.45×10^{-4}	1.50×10^{-4}	1.49×10^{-4}	1.53×10^{-4}
Total flow rate ($m^3\,s^{-1}$)	6.33×10^{-4}	6.28×10^{-4}	6.18×10^{-4}	6.29×10^{-4}
Water-cut	0.230	0.239	0.241	0.243
Hold-up ratio	1.37	1.30	1.29	1.27
Friction factor	0.00491	0.00502	0.00519	0.00496
Maximum turbulence viscosity ratio	18.8	19.9	20.8	16.8

viscosity ratio curve for the simulation with the highest oil viscosity is similar to the curves for the simulations with 0.745 Pas and 0.963 Pas but the peak is lower which is also seen in Table 5.7.

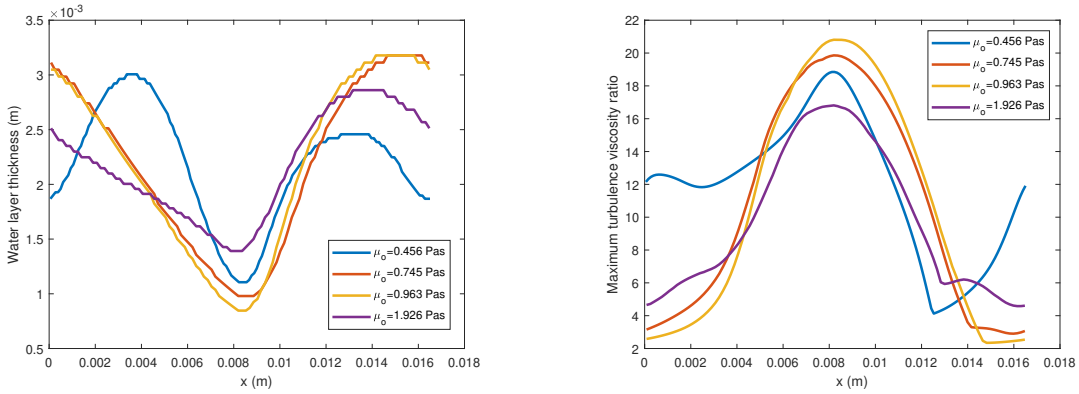

(a) (b)

Figure 5.18: Comparison of the (a) Water layer thickness (b) Maximum turbulence viscosity ratio for the fully developed simulations with oil viscosity of 0.456 Pas, 0.745 Pas, 0.963 Pas and 1.926 Pas.

The variation of the mean water volume fraction and the scaled mean streamwise velocity in the radial direction for the four simulations are shown in Figure 5.19. The curves for all the four simulations are identical. This shows that the mean quantities are identical for the simulations with different oil viscosities.

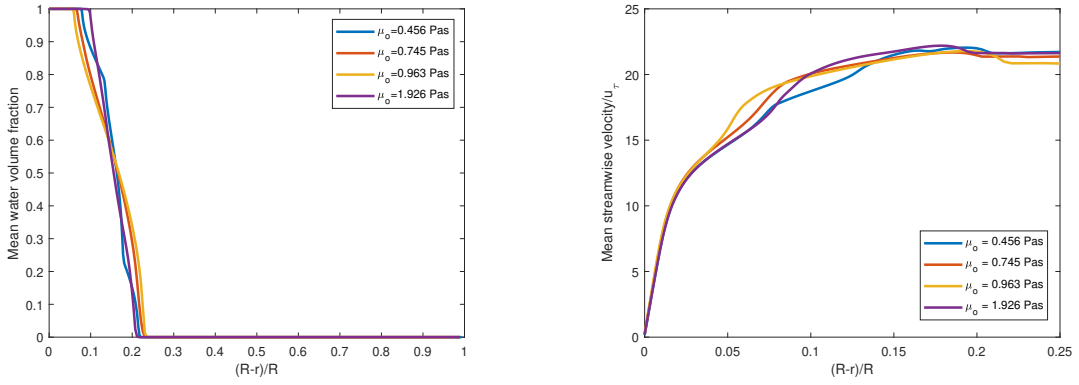

(a) (b)

Figure 5.19: Comparison of the (a) Mean water volume fraction (b) Scaled mean streamwise velocity for the simulations with oil viscosity of 0.456 Pas, 0.745 Pas, 0.963 Pas and 1.926 Pas.

The wave characteristics of the waves present in the simulation domain for the four simulations with different oil viscosities are compared in Table 5.8. It is observed that the wave velocity is the same for all the four simulations. The wavelength is same as the length of the computational domain for all the simulations except the simulation with the lowest oil viscosity. The wavelength for the simulation with the lowest oil viscosity is half the length of the simulation domain since it has two waves present in the domain. The wave frequency is higher for the simulation with the lowest oil viscosity which is expected due to the presence of two waves in the domain. The wave frequency for the other three simulations are similar. The wave amplitude is highest for the simulation with 0.963 Pa s with the wave amplitude for the simulation with 0.745 Pa s oil viscosity being similar to it. The wave amplitude for both the simulation with the highest and the lowest oil viscosity is smaller than the wave amplitude for the other two simulations. It can be concluded that even though the wave frequency, amplitude and wavelength are different for different oil viscosity simulations, the wave velocity does not change with a change in oil viscosity for this range of the viscosity ratio.

Table 5.8: Comparison of the wave characteristics for the simulations with oil viscosity of 0.456 Pa s, 0.745 Pa s, 0.963 Pa s and 1.926 Pa s.

Oil viscosity (Pas)	**0.456**	**0.745**	**0.963**	**1.926**
Wave velocity ($m\,s^{-1}$)	1.113	1.082	1.068	1.099
Wave length (m)	0.00828	0.01656	0.01656	0.01656
Wave frequency (Hz)	134.4	65.4	64.5	66.4
Wave amplitude (m)	0.00073	0.00108	0.00113	0.00067

Thus, from the analysis of the simulations with different oil viscosities, it can be concluded that for the range of the viscosity ratio considered, the flow rates obtained do not vary and can be considered constant. The water cut and the hold-up ratio vary slightly with change in oil viscosity. Also, even though the wave characteristics are considerably different, the wave velocity remains constant with change in oil viscosity. The mean volume fraction and the mean streamwise velocity also do not vary with change in oil viscosity. Thus, the results demonstrated in this thesis at a lower oil viscosity of 0.745 Pa s, can be compared with the DNS results of Kim and Choi [15], where the oil viscosity used is 17.6 Pa s. Still, care should be taken when using this comparison since the oil viscosity is indeed different.

6

Comparison with DNS results

The major objective of this thesis is to understand the extent of accuracy of the RANS approach by comparing the predictions from the RANS simulations with the DNS results from the simulations done by Kim and Choi [15]. There are five different cases with different oil holdups and imposed pressure drop which have been simulated by Kim and Choi [15], which are also simulated in OpenFOAM by using the RANS approach and the low-Re Launder-Sharma k-ϵ turbulence model. This chapter deals with the comparison of the results from the RANS OpenFOAM simulations with the DNS data.

6.1. Flow characteristics

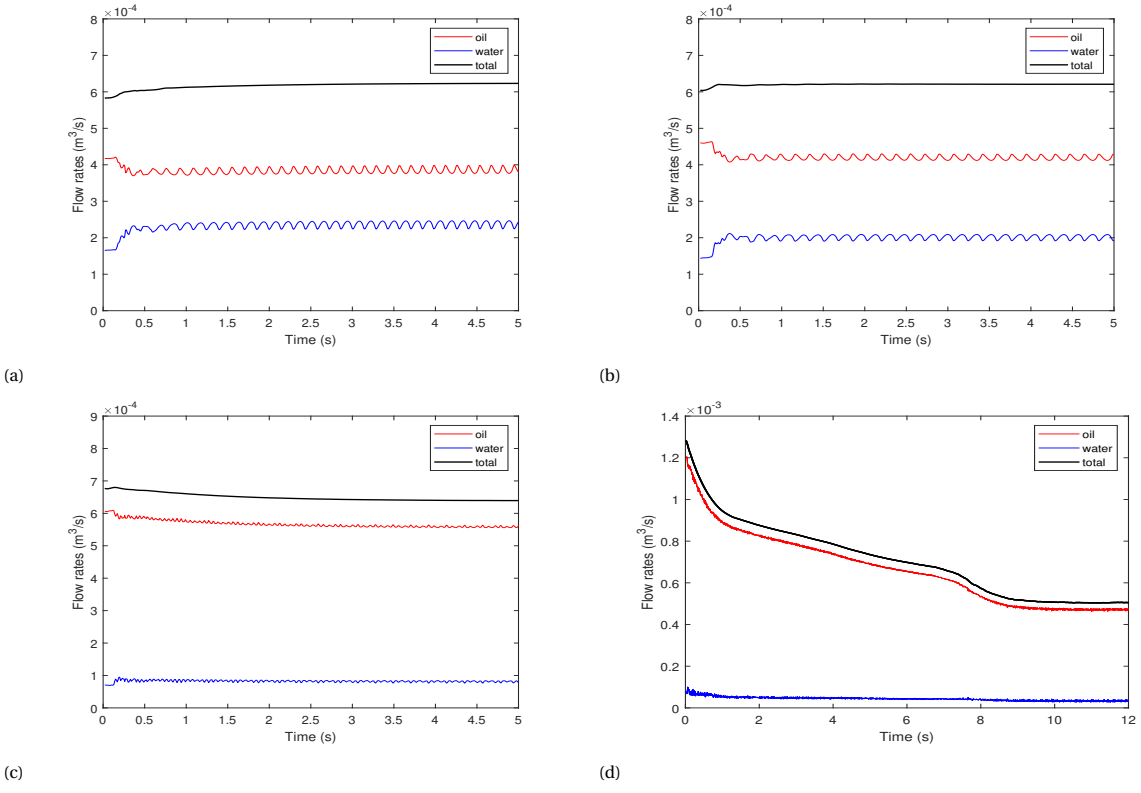

Figure 6.1: Variation of oil, water and total flow rates in time for the simulations with (a) $\epsilon_o = 0.56$ (b) $\epsilon_o = 0.62$ (c) $\epsilon_o = 0.83$ (d) $\epsilon_o = 0.91$.

The five cases that are simulated in this thesis are listed in Table 3.1. The grid used for the simulations for ϵ_o = 0.71, 0.83, and 0.91 is 200 cells in the radial direction and 100 cells in the streamwise direction. The grids used for $\epsilon_o = 0.62$ and $\epsilon_o = 0.56$ are 400X200 and 600X300 cells, respectively. The domain length for the simulation

with $\epsilon_o = 0.56$, $\epsilon_o = 0.62$ and $\epsilon_o = 0.71$ is 0.01656 m while the domain length for the simulation with $\epsilon_o = 0.83$ and $\epsilon_o = 0.91$ is taken as 0.0138 m as fouling was observed for a larger domain length. The variation of oil, water and total flow rates for the five different cases except $\epsilon_o = 0.71$ is shown in Figure 6.1. The variation of flow rates for $\epsilon_o = 0.71$ case was shown in Figure 5.2c. These simulations are also carried out until 5 s to ensure that they are fully developed. The case for $\epsilon_o = 0.91$ has been carried out until 12 s since it needed more simulation time to become fully developed as seen from Figure 6.1d.

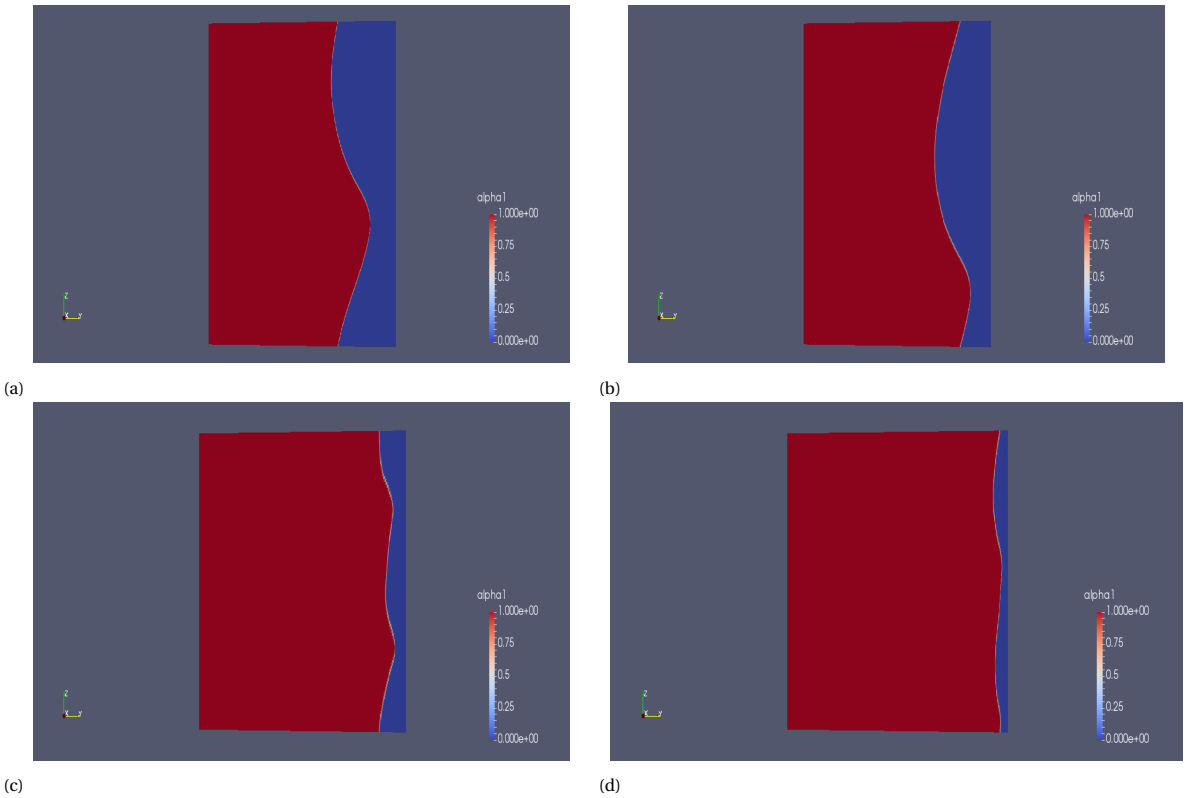

Figure 6.2: Wave structure for the simulations with (a) $\epsilon_o = 0.56$ (b) $\epsilon_o = 0.62$ (c) $\epsilon_o = 0.83$ (d) $\epsilon_o = 0.91$.

The wave structure for the simulations with ϵ_o=0.56, 0.62, 0.83, and 0.91 is shown in Figure 6.2. It is observed that there is one wave in the simulation domain for ϵ_o=0.56 and 0.62 while there are two waves in the simulation domain for ϵ_o=0.83 and 0.91.

The variation of oil, water and total flow rates with varying oil holdup is shown in Figure 6.3. The comparison of the predictions of the 2D RANS OpenFOAM simulations with the DNS data from Kim and Choi [15] for the oil, water and total flow rates is also shown in Figure 6.3. As can be observed, the water flow rate from the 2D OpenFOAM simulations has a very good agreement with the DNS predictions of Kim and Choi [15]. The oil flow rate first increases with an increase in the oil holdup with a maximum at ϵ_o=0.83 and then decreases for ϵ_o=0.91. The total flow rate from the 2D OpenFOAM simulations follows the same trend as the oil flow rate, with a maximum at ϵ_o=0.83 and a decrease for ϵ_o=0.91. This is different from the DNS predictions where the maximum total flow rate occurs at ϵ_o=0.71 and decreases for ϵ_o=0.83 and 0.91. As observed in Table 6.1, the total flow rate from the RANS simulations in OpenFOAM is always higher than the DNS value. There is a difference of 10% between the DNS data and the 2D OpenFOAM predictions for the total flow rate for ϵ_o=0.56, 0.62 and 0.71. This difference increases to 16% for ϵ_o=0.83 and to 29% for ϵ_o=0.91. As was seen from the 1D OpenFOAM simulations in chapter 4, the turbulence is significant for simulations with ϵ_o=0.56, 0.62, and 0.71. The turbulence levels in the water annulus are lower for ϵ_o=0.83 as compared to lower oil holdups while there is no turbulence for ϵ_o=0.91. This shows that the low-Re Launder-Sharma $k-\epsilon$ turbulence model is able to predict the flow rates within 10% of DNS predictions when significant turbulence levels are there in the water annulus. The difference in the predictions increases with decreasing turbulence levels.

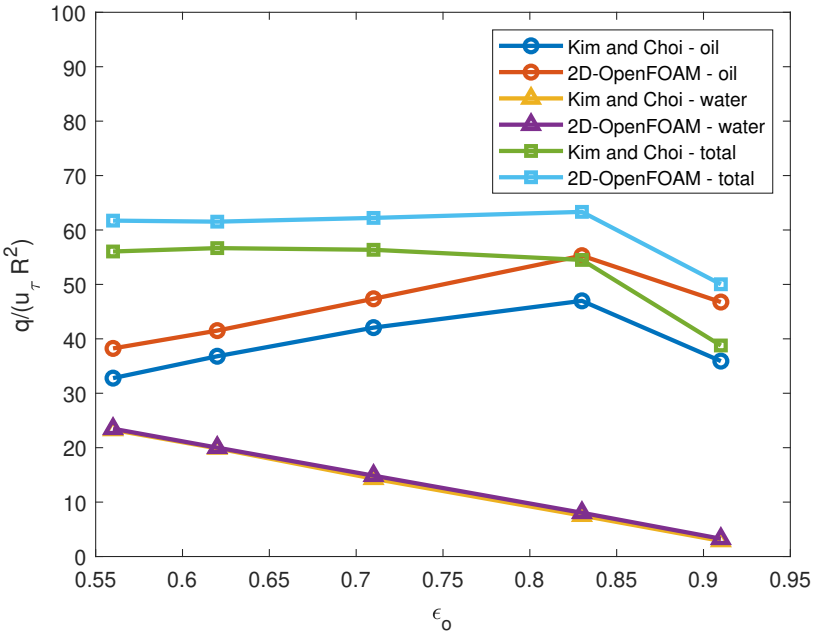

Figure 6.3: Comparison of oil, water and total flow rates from the 2D OpenFOAM simulations with the DNS simulations of Kim and Choi [15] with varying oil holdup fraction.

If the pipe has only high viscosity oil flowing alone at the same wall friction (i.e. $\mathrm{Re}_{\tau,o} \approx 0.040$), the oil flow rate is $q_o/u_{\tau,o}R^2 \approx 0.032$ as mentioned by Kim and Choi [15]. This is orders of magnitude lower than what is predicted for core-annular flow. Also, since the total flow rate and the oil flow rate have maximum values at ϵ_o=0.83 and decreases for ϵ_o=0.91, it does not make sense to increase the oil holdup further because the aim of larger oil throughput will not be fulfilled. The water region for ϵ_o=0.91 is very narrow and the oil core suffers from high wall shear stress to give a lower oil flow rate. Thus, it can be concluded that core-annular flow is indeed essential to transport high viscosity oils since it has a higher oil flow rate as compared to when the oil flows alone in the pipe. Also, there is a particular value of oil holdup for which there is a maximum for the total and oil flow rates. Hence, that should be the oil holdup used in practice to transport the maximum amount of oil using core-annular flow instead of increasing ϵ_o.

Table 6.1: Comparison of oil, water and total flow rates from the 2D OpenFOAM simulations with the DNS simulations of Kim and Choi [15] for the simulations with oil holdup fraction ε = 0.56, 0.62, 0.71, 0.83 and 0.91.

	Oil flow rate (m^3/s)	**Water flow rate (m^3/s)**	**Total flow rate (m^3/s)**	**% difference in total flow rate (OpenFOAM wrt DNS)**
2D OpenFOAM for ϵ_o=0.56	3.86×10^{-4}	2.37×10^{-4}	6.23×10^{-4}	+10%
Kim and Choi for ϵ_o=0.56	3.32×10^{-4}	2.36×10^{-4}	5.68×10^{-4}	
2D OpenFOAM for ϵ_o=0.62	4.19×10^{-4}	2.02×10^{-4}	6.21×10^{-4}	+8%
Kim and Choi for ϵ_o=0.62	3.73×10^{-4}	2.01×10^{-4}	5.74×10^{-4}	
2D OpenFOAM for ϵ_o=0.71	4.78×10^{-4}	1.50×10^{-4}	6.28×10^{-4}	+10%
Kim and Choi for ϵ_o=0.71	4.26×10^{-4}	1.45×10^{-4}	5.71×10^{-4}	
2D OpenFOAM for ϵ_o=0.83	5.58×10^{-4}	8.12×10^{-5}	6.39×10^{-4}	+16%
Kim and Choi for ϵ_o=0.83	4.76×10^{-4}	7.62×10^{-5}	5.52×10^{-4}	
2D OpenFOAM for ϵ_o=0.91	4.72×10^{-4}	3.30×10^{-5}	5.05×10^{-4}	+29%
Kim and Choi for ϵ_o=0.91	3.64×10^{-4}	2.91×10^{-5}	3.93×10^{-4}	

The comparison for the water-cut, the hold-up ratio and the friction factor for all the five cases between the 2D OpenFOAM results and the DNS data is shown in Table 6.2. As can be observed, the difference in the comparison of the water-cut decreases with increasing oil holdup and is identical for ϵ_o=0.91 for both the 2D OpenFOAM simulation and the DNS prediction. The relative difference between the 2D OpenFOAM simu-

Table 6.2: Comparison of the result outputs from the 2D OpenFOAM simulations with the DNS simulations of Kim and Choi [15] for the simulations with oil holdup fraction ε = 0.56, 0.62, 0.71, 0.83 and 0.91.

	Water-cut	**Hold-up ratio**	**Friction factor**
2D OpenFOAM for ϵ_o=0.56	0.38	1.28	0.00510
Kim and Choi for ϵ_o=0.56	0.42	1.11	0.00614
2D OpenFOAM for ϵ_o=0.62	0.33	1.27	0.00513
Kim and Choi for ϵ_o=0.62	0.35	1.14	0.00600
2D OpenFOAM for ϵ_o=0.71	0.24	1.30	0.00502
Kim and Choi for ϵ_o=0.71	0.25	1.20	0.00607
2D OpenFOAM for ϵ_o=0.83	0.13	1.41	0.00485
Kim and Choi for ϵ_o=0.83	0.14	1.28	0.00649
2D OpenFOAM for ϵ_o=0.91	0.07	1.41	0.00776
Kim and Choi for ϵ_o=0.91	0.07	1.24	0.01282

Table 6.3: Relative difference between the 2D OpenFOAM simulations and the DNS predictions for the holdup ratio and the friction factor for the simulations with oil holdup fraction ε_o = 0.56, 0.62, 0.71, 0.83 and 0.91.

Oil holdup	**Difference for holdup ratio**	**Difference for friction factor**
0.56	15%	-17%
0.62	11%	-15%
0.71	8%	-17%
0.83	10%	-25%
0.91	14%	-39%

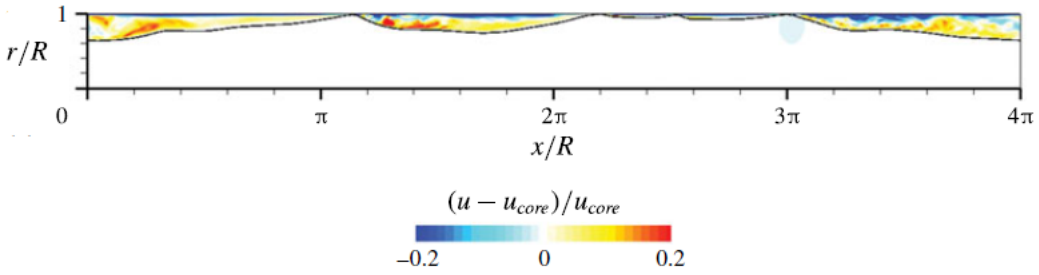

(a)

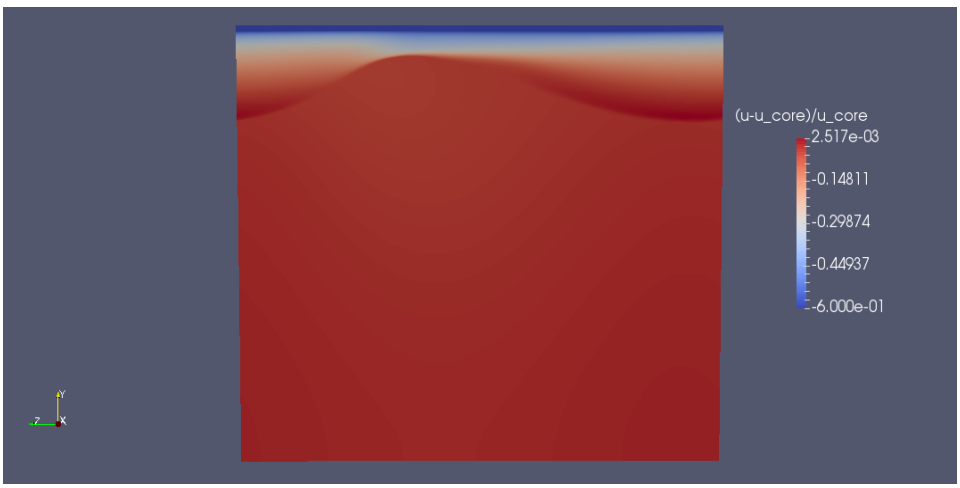

(b)

Figure 6.4: Comparison of the streamwise velocity contours relative to the core velocity for the simulation with ε_o = 0.71 (a) Kim and Choi's [15] DNS simulation (b) 2D OpenFOAM simulation.

lations and the DNS results for the friction factor and the holdup can be seen in Table 6.3. The difference for the holdup ratio decreases first from 15% for ϵ_o = 0.56 to 8% for ϵ_o = 0.71 and then increases to 14% for ϵ_o = 0.91. The friction factor from the 2D OpenFOAM simulations with ϵ_o=0.56, 0.62 and 0.71 is about 17% lower than that from the DNS data. The friction factor for the 2D OpenFOAM simulations with ϵ_o=0.83 is 25% lower while for the 2D OpenFOAM simulations with ϵ_o=0.91, the friction factor is 39% lower as compared to the corresponding friction factor from the DNS data. Thus, it can be concluded that for fully turbulent flow, the difference between the prediction of the friction factor for the 2D RANS OpenFOAM simulations and the DNS simulations by Kim and Choi [15] is about 17% while the difference increases with decreasing turbulence levels.

The comparison of the contours of the streamwise velocity relative to the core velocity for the simulation with ϵ_o=0.71 between the 2D OpenFOAM predictions and the DNS results is shown in Figure 6.4. Note that the flow is depicted from left to right for the DNS results in Figures 6.4a and 6.5a, and from right to left for the 2D OpenFOAM results in Figures 6.4b and 6.5b. The core velocity is calculated as the oil velocity averaged over the volume occupied by the oil as $u_{\text{core}} = j_o/\epsilon_o$ where j_o is the superficial velocity of oil. As can be observed in the Figure 6.4a, the DNS results predict that the oil core contains nearly zero relative velocity which means that the flow in the oil core is a plug flow with velocity u_{core} and having zero velocity fluctuations. This is also observed in Figure 6.4b, which is the streamwise velocity contour from the 2D OpenFOAM simulation. Since the oil core moves at a constant velocity and deforms slowly due to high viscosity, the interface behaves like a slowly deforming wavy wall [4]. Hence, the flow in the water annulus can be characterized as a Poiseuille-Couette flow with a driving velocity of u_{core} and the mean pressure gradient of $dP/dx - \rho_w g$. The relative velocity near the wall is negative while the relative velocity near the interface is positive in a reference frame moving with u_{core}. This can be observed in both the Figures 6.4a and 6.4b. Thus, the qualitative comparison of the streamwise velocity contour for the 2D OpenFOAM and DNS results show similar predictions.

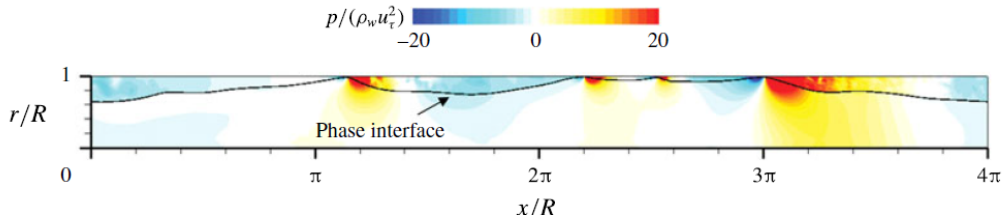

(a)

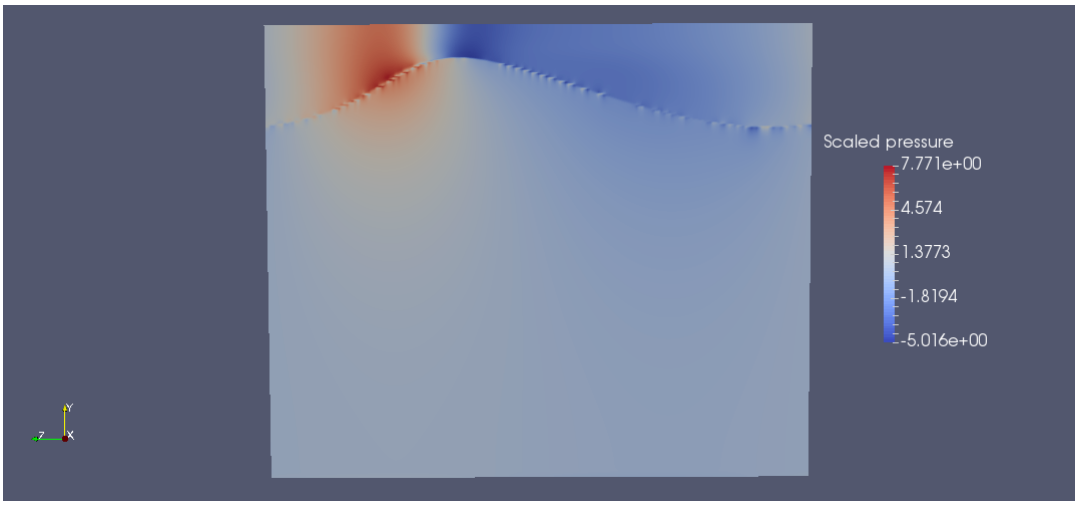

(b)

Figure 6.5: Comparison of the instantaneous pressure fluctuation contours for the simulation with ϵ_o = 0.71 (a) Kim and Choi's [15] DNS simulation (b) 2D OpenFOAM simulation.

The contours of the pressure fluctuations for ϵ_o = 0.71 from the 2D OpenFOAM simulations are compared with the DNS results from Kim and Choi [15] in Figure 6.5. The contours are of the scaled pressure which is

$p/(\rho_w u_{tau}^2)$. This comparison of the contours of the pressure fluctuations looks similar such that the high pressure region is ahead of the wave crest while the low pressure region is behind the wave crest. This is due to the fact that the oil core moves with a constant velocity and drives the water. The pressure at the wave trough is negative and is almost uniform in both the figures. The pressure fluctuations have a jump at the interface which is due to the surface tension. Figure 6.5 and Figure 6.4 show the contours at the same instant of time and thus can be used to understand the relation between the pressure fluctuations and the velocity. The water velocity near the wave trough is nearly uniform while it changes rapidly in both the radial and streamwise direction at the wave crest. The velocity gradient at the phase interface is small except at the wave crest. the high pressure region was also found just beside the wave crest. Thus, the velocity gradient at the phase interface is higher in the high pressure region.

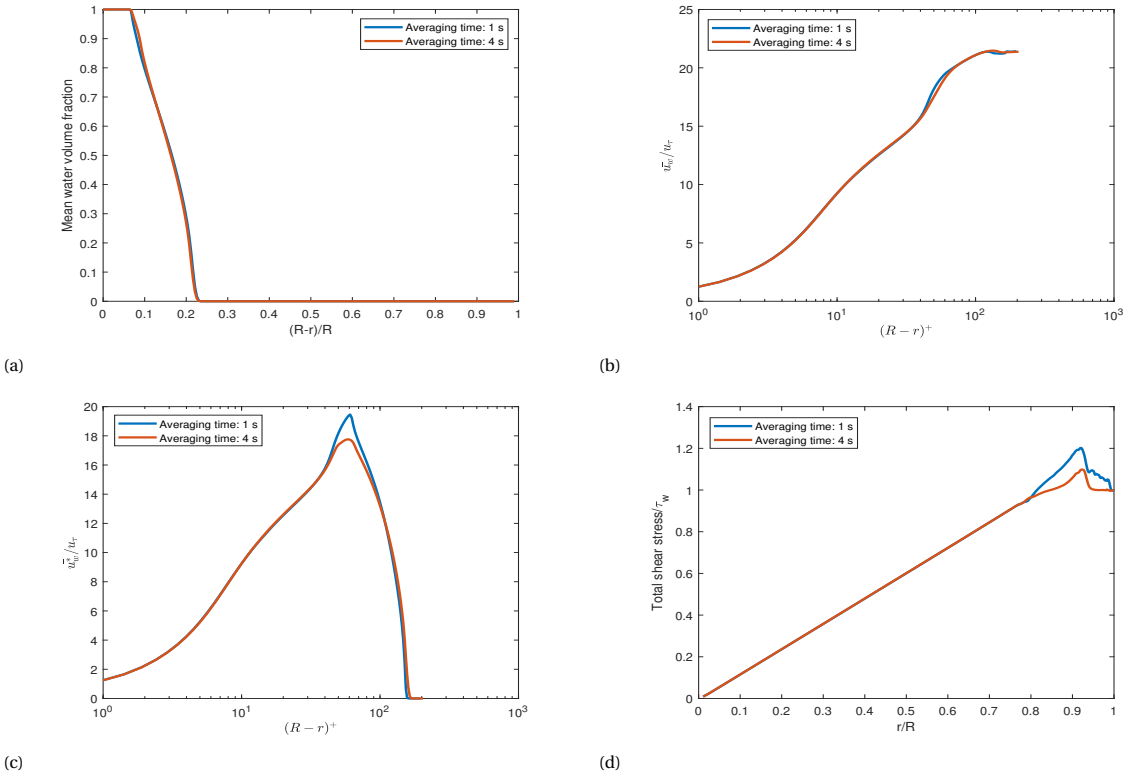

Figure 6.6: Comparison of the (a) Mean water volume fraction (b) Scaled mean streamwise water velocity (c) Scaled mean streamwise water velocity weighted with the mean water volume fraction (d) Scaled total shear stress for averaging time of 1 s and 4 s for the case with oil volume fraction of 0.71.

It should be ensured that the mean water volume fraction, scaled mean streamwise water velocity, scaled mean streamwise water velocity weighted with the mean water volume fraction and the shear stresses are accurately time averaged. Thus, a comparison of the time averaging for simulation time of 1 s and simulation time of 4 s is performed to ascertain if the time averaging is accurate or not. This comparison is shown in Figure 6.6 for the case with oil volume fraction $\varepsilon_o = 0.71$. It is observed that the curves for the mean water volume fraction and the scaled mean streamwise water velocity are on top of each other. The curves for the scaled mean streamwise water velocity weighted with the mean water volume fraction and the total shear stress differ slightly. The curve with averaging time 1 s shows wiggles at and after the interface for the total shear stress while the wiggles are absent for the curve with averaging time 4 s. Thus, it can be concluded that the averaging time of 4 s is appropriate while the averaging time of 1 s still has some inaccuracies. Thus, the averaging time used for the quantities presented in this thesis is 4 s.

The mean streamwise velocity for different oil holdups is compared between the 2D OpenFOAM simulations and the DNS results in Figure 6.7. The mean streamwise velocity is calculated from equation 5.2 and 5.3, as defined by Kim and Choi [15]. The mean streamwise velocity first increases with increasing distance from the

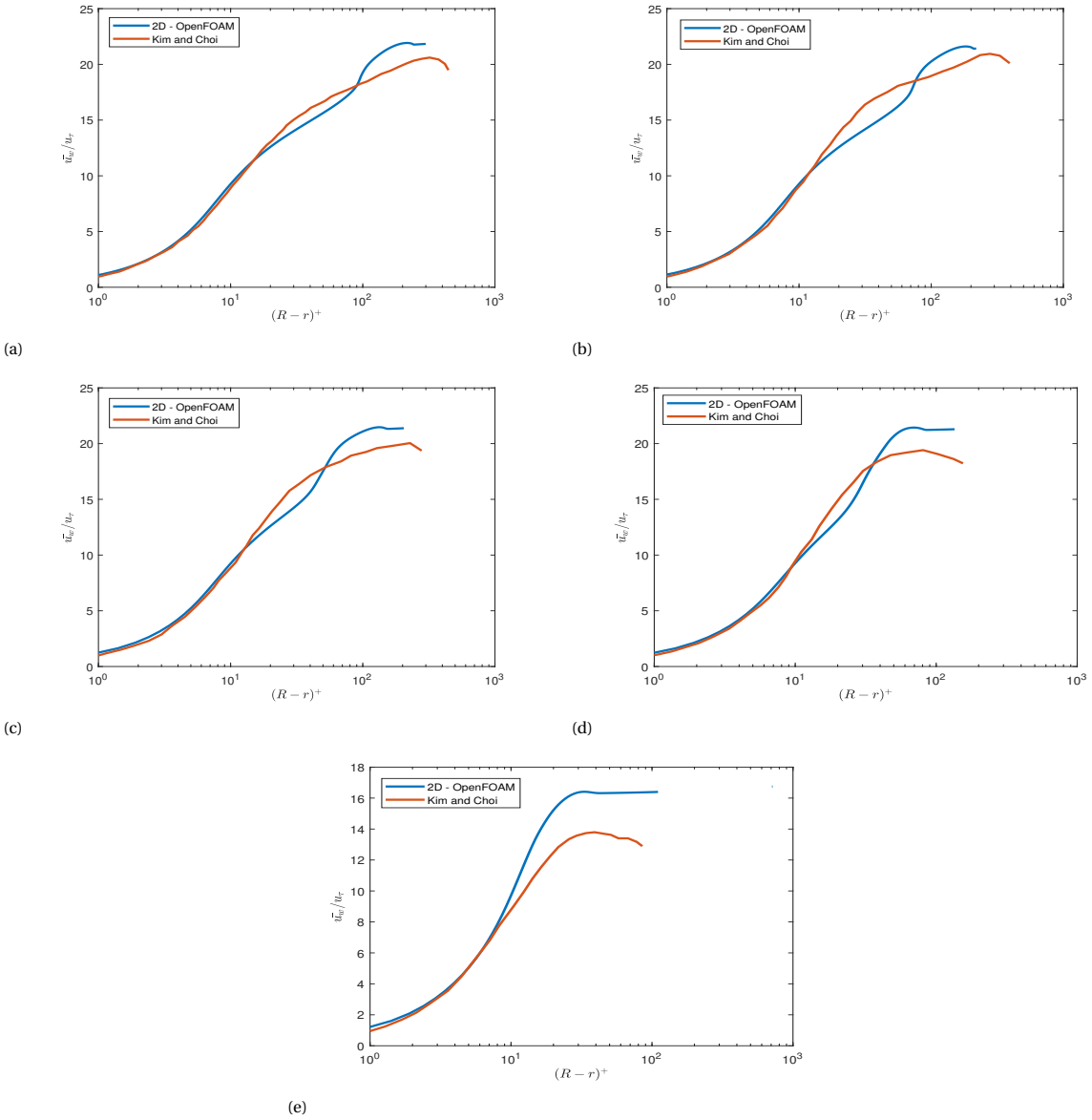

Figure 6.7: Comparison of the scaled mean streamwise water velocity between Kim and Choi [15] results and 2D OpenFOAM predictions for (a) $\varepsilon_o = 0.56$ (b) $\varepsilon_o = 0.62$ (c) $\varepsilon_o = 0.71$ (d) $\varepsilon_o = 0.83$ (e) $\varepsilon_o = 0.91$.

wall, attains a maximum value and then decreases to a constant value. The velocity of the oil remains constant throughout the core. Thus, the maximum velocity of the water is higher than the oil velocity. This was also observed at the wave crest in Figure 6.4. The comparison for the mean streamwise water velocity shows that a better agreement for the 2D OpenFOAM simulations with the DNS results is found for fully turbulent cases as compared to the case with less or no turbulence. The difference in the mean streamwise velocity increases with an increase in oil holdup fraction.

Kim and Choi also define the mean streamwise water velocity weighted with the mean water volume fraction as shown in equation 6.1. The value of $\bar{u}^*_w$ first increases with increasing distance from the wall, reaches a maximum and then decreases. The decrease in the $\bar{u}^*_w$ is due to the change in the $\bar{\psi}$ value from 1 to 0. The comparison between the 2D OpenFOAM simulations and the DNS data for all the five cases is presented in Figure 6.8. This comparison also follows the same trend with the case for $\varepsilon_o = 0.91$ giving the worst comparison because of the non-existent turbulence.

$$\begin{aligned}\bar{u}_w^*(r) &= \frac{\iiint u(x,r,\theta,t)\psi(x,r,\theta,t)\mathrm{d}\theta\mathrm{d}x\,\mathrm{d}t}{\iiint \mathrm{d}\theta\mathrm{d}x\,\mathrm{d}t} \\ &= \frac{\iiint u(x,r,\theta,t)\psi(x,r,\theta,t)\mathrm{d}\theta\mathrm{d}x\,\mathrm{d}t}{\iiint \psi(x,r,\theta,t)\mathrm{d}\theta\mathrm{d}x\,\mathrm{d}t}\,\frac{\iiint \psi(x,r,\theta,t)\mathrm{d}\theta\mathrm{d}x\,\mathrm{d}t}{\iiint \mathrm{d}\theta\mathrm{d}x\,\mathrm{d}t} \\ &= \bar{u}_w(r)\bar{\psi}(r)\end{aligned} \tag{6.1}$$

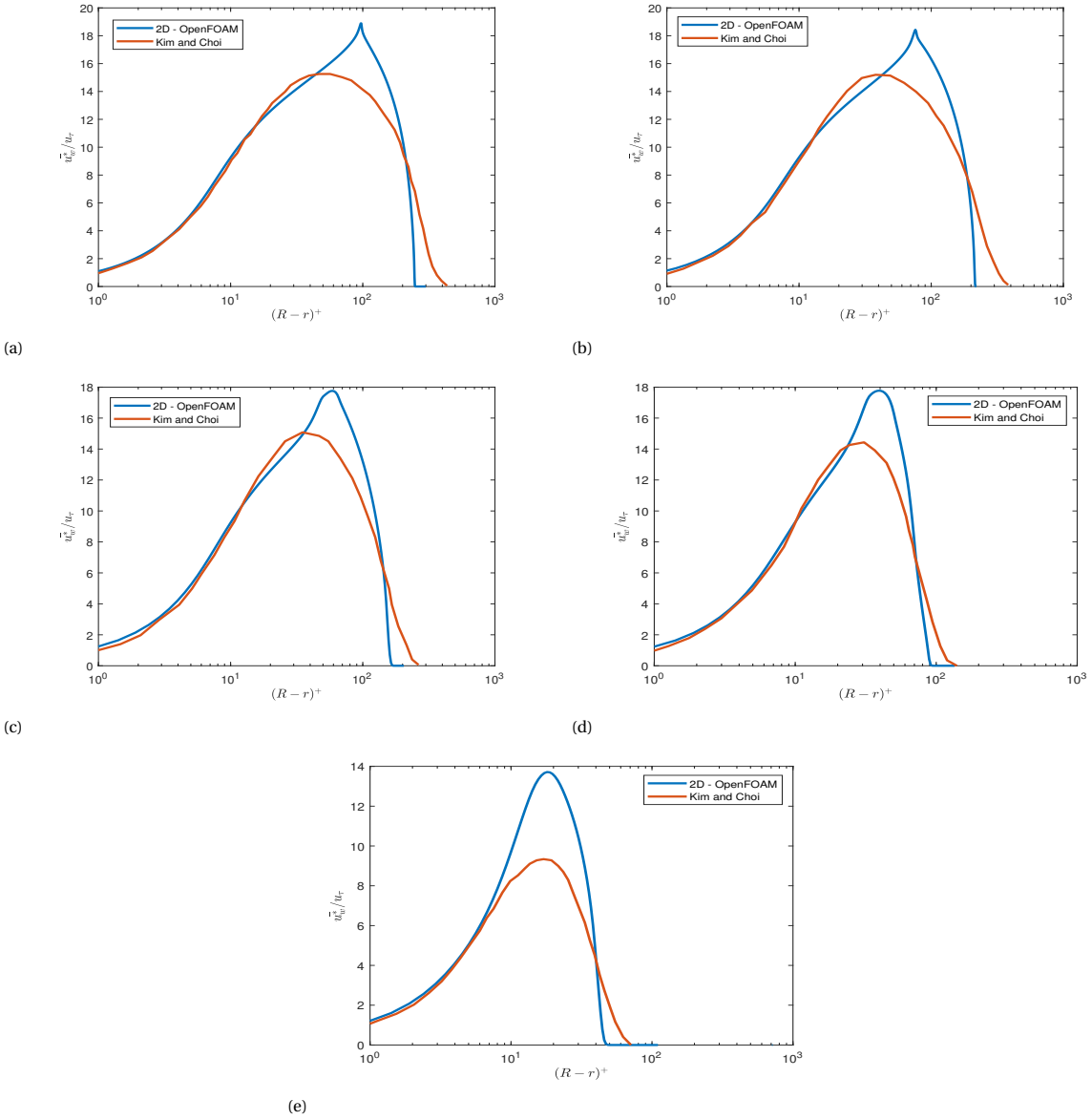

Figure 6.8: Comparison of the scaled mean streamwise water velocity weighted by the mean water volume fraction between Kim and Choi [15] results and 2D OpenFOAM predictions for (a) $\varepsilon_o = 0.56$ (b) $\varepsilon_o = 0.62$ (c) $\varepsilon_o = 0.71$ (d) $\varepsilon_o = 0.83$ (e) $\varepsilon_o = 0.91$.

6.2. Wave characteristics

Due to the waves present at the interface, there is an intermittent region present at the interface where the volume fraction changes. Thus, it is important to look at the mean quantities and compare it for the 2D OpenFOAM results and the DNS data from Kim and Choi [15]. Kim and Choi [15] have defined the mean water volume fraction as shown in equation 5.1. The mean water volume fraction denotes the amount of water

present at the specified radial location in the domain. The comparison between 2D OpenFOAM predictions and the DNS results for all five cases is shown in Figure 6.9. For the DNS results, the $\bar{\psi}$ value linearly decreases with distance from wall except for the region with very low $\bar{\psi}$ values. While for the 2D OpenFOAM simulations, the $\bar{\psi}$ has a constant value of 1 for the initial region very close to wall while it decreases almost linearly after that.

The comparison in Figure 6.9 shows that there is a very good agreement in the mean water volume fraction for the higher oil holdups while the difference between the predictions increases with decreasing oil holdups. This can be explained from Figure 6.10, which shows the comparison of the radial location of the maximum and minimum points of the interface in the simulation domain. It shows that there is a larger difference for both, the maximum and minimum points of the interface, between the 2D OpenFOAM simulations and the DNS data for lower oil holdups. The difference decreases as the oil holdup increases. Thus, it also supports the observation done for the mean water volume fraction that the difference is higher at lower oil holdups.

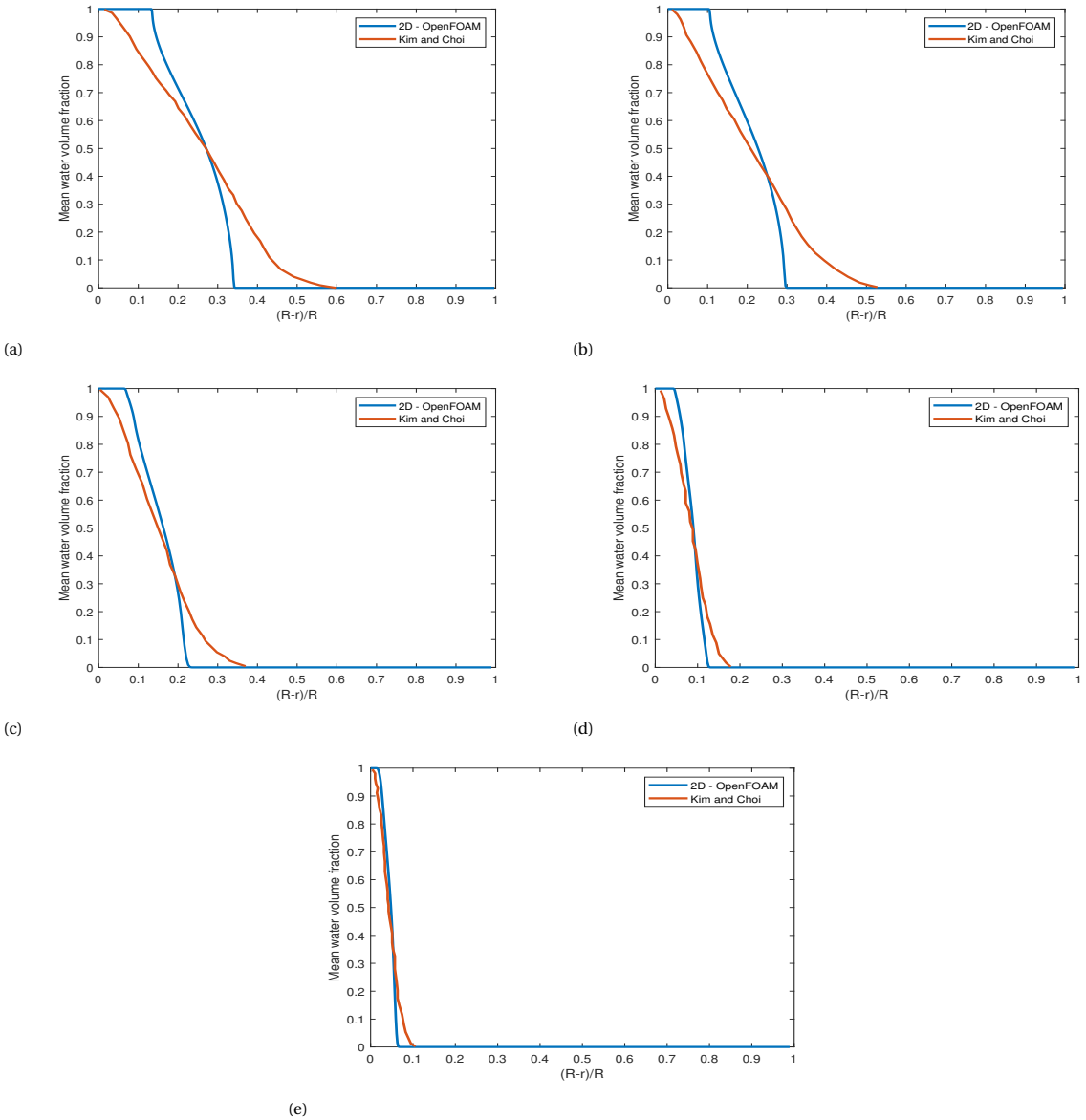

Figure 6.9: Comparison of the mean water volume fraction in the radial direction between the Kim and Choi [15] results and the 2D OpenFOAM predictions for (a) $\varepsilon_o = 0.56$ (b) $\varepsilon_o = 0.62$ (c) $\varepsilon_o = 0.71$ (d) $\varepsilon_o = 0.83$ (e) $\varepsilon_o = 0.91$.

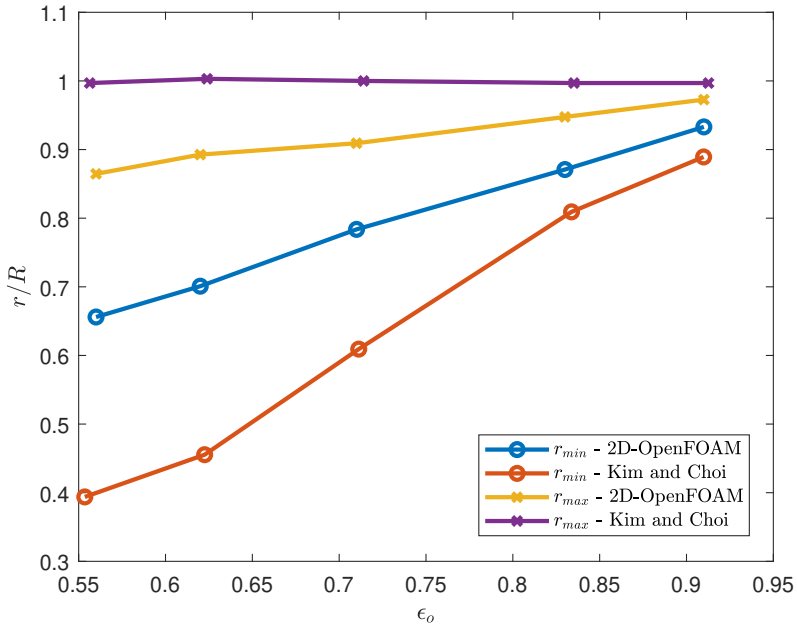

Figure 6.10: Comparison of minimum and maximum interface position from the 2D OpenFOAM simulations with the DNS simulations of Kim and Choi [15] for varying oil holdup fraction.

The maximum interface position from the DNS data is almost constant while the minimum interface position increases with increasing oil holdup. This shows that the wave amplitude decreases with increasing oil holdup. For the 2D OpenFOAM simulations, the maximum interface position moves slightly towards the wall with increasing oil holdup while the minimum interface position also increases with increasing oil holdup. The increase in the minimum interface position is larger than the increase in maximum wave position which means that the amplitude decreases with increasing oil holdup for the 2D OpenFOAM simulations as well. This can also be seen from Table 6.4 where the wave characteristics for all the five cases are presented. The wave amplitude decreases from 0.00138 m for ε_o = 0.56 to 0.00023 m for ε_o = 0.91. The wavelengths for ε_o = 0.56, 0.62 and 0.71 will be the simulation domain length (0.01656 m) as there is only one wave present in the simulation domain. While the wavelength for ε_o = 0.83 and 0.91 will be half of the domain length (0.0138 m) as there are two waves present in the simulation domain. The wave velocity is almost constant for all the five cases. The wave frequency is in the range of 60-65 Hz for ε_o = 0.56, 0.62 and 0.71 while it is about 145 Hz for ε_o = 0.83 and 0.91.

The comparison of the probability distribution function (PDF) of radial location of the interface for the 2D OpenFOAM simulations and the DNS predictions is shown in Figure 6.11. The PDF represents how often the interface is found at the specified radial location. If the peak of the PDF is broad, it means that the waves in the simulation domain have a mixture of wavelengths while the sharper PDF represents the dominance of a specific wavelength. The DNS predictions for the cases with ε_o = 0.56 and 0.71 have a broader peak while the case with ε_o = 0.91 has a sharper peak. The RANS simulations always have a sharp peak since it has a specified dominant wavelength as also shown in Table 6.4. The PDFs shift towards the wall with increasing oil holdup which substantiates the fact that the minimum interface position increases with increasing

Table 6.4: Comparison of the wave characteristics for the simulations with oil holdup fraction ε_o = 0.56, 0.62, 0.71, 0.83 and 0.91.

Oil holdup	**0.56**	**0.62**	**0.71**	**0.83**	**0.91**
Wave velocity ($m\,s^{-1}$)	1.02	1.003	1.082	1.0005	1.0002
Wave length (m)	0.01656	0.01656	0.01656	0.0069	0.0069
Wave frequency (Hz)	61.59	60.55	65.4	145.01	144.96
Wave amplitude (m)	0.00138	0.00126	0.00108	0.00042	0.00023

oil holdup. Also, the difference between the maximum and the minimum radial value for the interface decreases with the increase in oil holdup, which substantiates the fact that the wave amplitude decreases with increasing oil holdup. The comparison between the 2D OpenFOAM simulations and the DNS predictions for $\varepsilon_o = 0.91$ shows that the peak is almost at the same radial location while the agreement for $\varepsilon_o = 0.56$ and 0.71 is not good. Thus, it can be concluded that due to the presence of a broader peak (waves with different wavelengths) in the DNS predictions at lower oil holdups, the agreement for the wave characteristics decreases with the 2D OpenFOAM simulations.

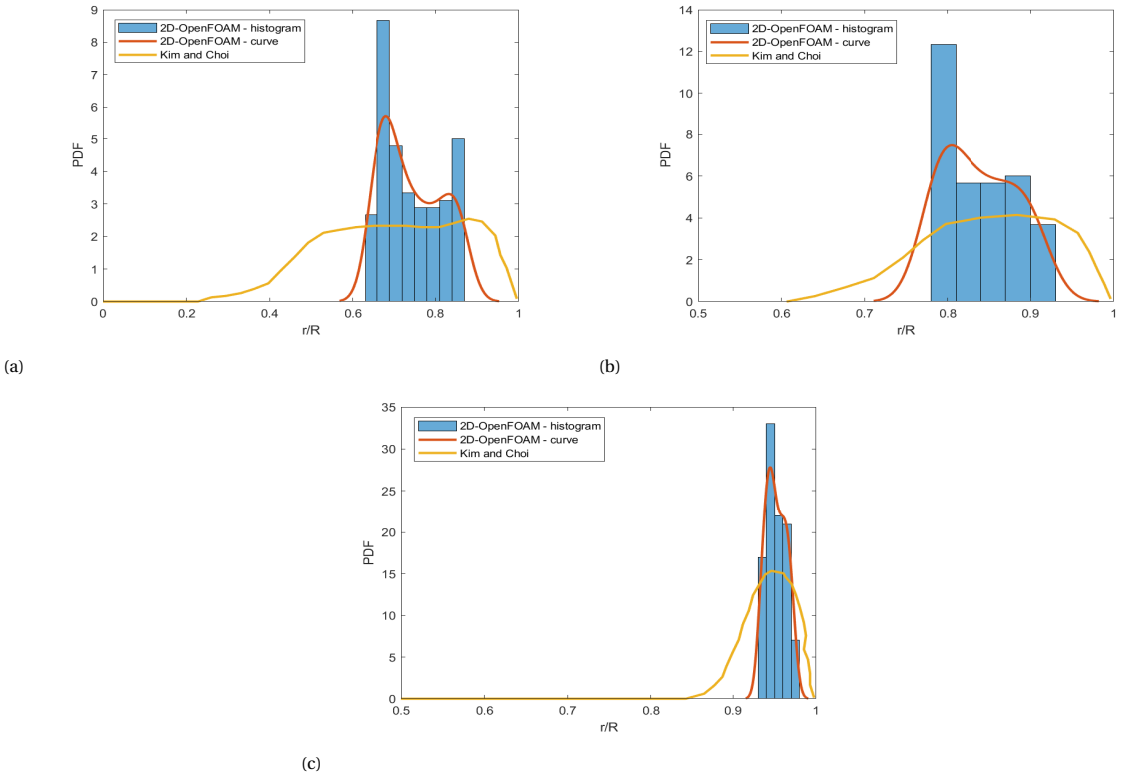

Figure 6.11: Comparison of PDFs of radial location of the interface from the 2D OpenFOAM simulations with the DNS simulations of Kim and Choi [15] for (a) $\varepsilon_o = 0.56$ (b) $\varepsilon_o = 0.71$ (c) $\varepsilon_o = 0.91$.

6.3. Turbulence characteristics

The turbulence levels inside the simulation domain can be represented by calculating the maximum turbulence viscosity ratio. Figure 6.12 shows the comparison of the maximum turbulence viscosity ratio in the simulation domain for all the five cases of different oil holdups. The X-axis has been scaled with the streamwise domain length, L, so that the comparison is easier since the domain length for all the cases is not same. Figure 6.12 shows that the maximum turbulence viscosity ratio decreases with increasing oil holdup which was also observed in the 1D simulations. The flow can be said to be fully turbulent if the turbulence viscosity ratio is above 10 or so, which is the case for simulations with $\varepsilon = 0.56$, 0.62 and 0.71. The case with $\varepsilon = 0.83$ still has some turbulence level in the domain but it cannot be called fully turbulent while the case with $\varepsilon = 0.91$ does not have any turbulence in the simulation domain. Thus, it can be concluded that a fully turbulent 2D OpenFOAM simulation has less differences with the DNS data as compared to the 2D OpenFOAM simulation with less or no turbulence, which has higher differences with the DNS data.

The comparison of the viscous shear stress, Reynolds shear stress and the total shear stress between the 2D OpenFOAM simulations and the DNS data is shown in Figure 6.13, 6.15 and 6.16 respectively. The total shear stress is calculated as shown in equation 6.2.

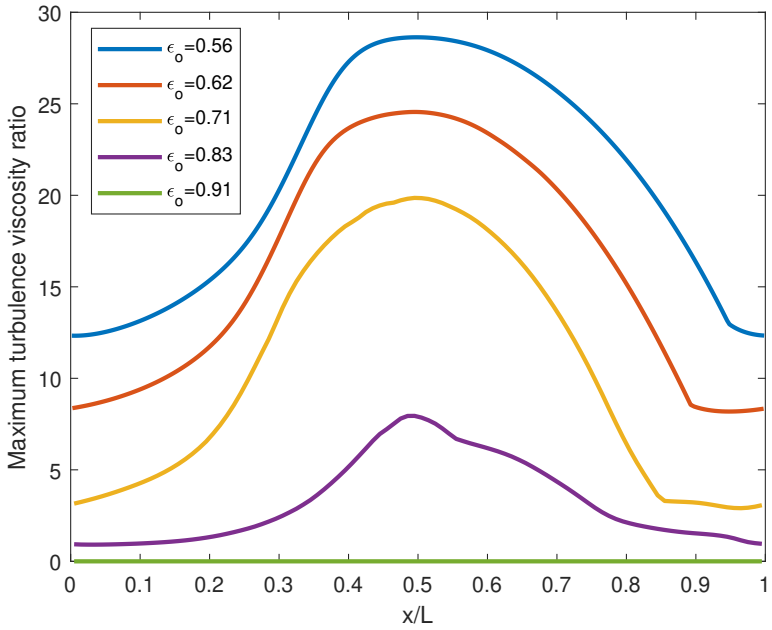

Figure 6.12: Comparison of maximum turbulence viscosity ratio for fully developed simulations with oil holdup fraction ε = 0.56, 0.62, 0.71, 0.83 and 0.91.

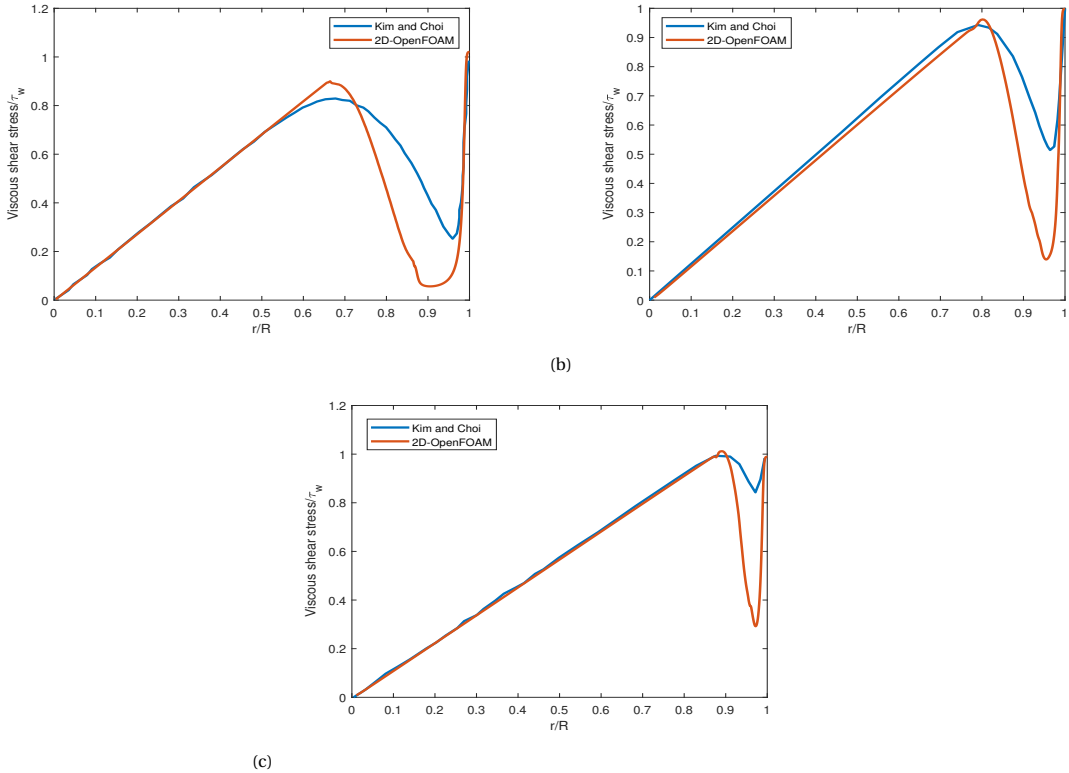

Figure 6.13: Comparison of the scaled viscous shear stress from the 2D OpenFOAM simulations with the DNS simulations of Kim and Choi [15] for (a) $\varepsilon_o = 0.56$ (b) $\varepsilon_o = 0.71$ (c) $\varepsilon_o = 0.83$.

$$\bar{\tau}(r) = \overline{\rho u_x u_r} - \overline{\mu\left(\frac{\partial u_x}{\partial r} + \frac{\partial u_r}{\partial x}\right)} \tag{6.2}$$

The second term on the right of equation 6.2 denotes the viscous shear stress which is dominant in the oil core. The overbar denotes the averaging in time and space. The viscous shear stress increases with the increase in distance from the centre while it decreases rapidly when $\bar{\psi} \neq 0$, reaches a local minimum and then increases with decrease in distance from the wall. The curves of the viscous shear stress for both the 2D OpenFOAM simulation and the DNS data are identical in the oil core since the Reynolds shear stress is negligible in the oil core. The total shear stress can also be calculated, as shown in equation 6.3, from the momentum balance applied to a section of the pipe, where the surface tension term is negligibly small [15]. The 2D OpenFOAM simulation curve has a lower local minimum as compared to the DNS curve for the viscous shear stress. Also, both the curves become identical once again very near to the wall.

$$\bar{\tau}(r) = \frac{r}{2}\left(-\frac{\mathrm{d}P}{\mathrm{d}x}\right) + \frac{1}{r}\int_0^r \left(\overline{\sigma\kappa\delta n_x} - \bar{\rho}g\right) r \, \mathrm{d}r \tag{6.3}$$

The first term on the right in equation 6.2 denotes the Reynolds stress but since $\overline{\rho u_x u_r} = \bar{u}_x\overline{\rho u_r'} + \overline{\rho u_x' u_r'} \approx \overline{\rho u_x' u_r'}$, the contribution to Reynolds shear stress for the RANS simulations can be divided into two parts. The first being the contribution from the modelled turbulence calculated directly from the turbulence model used. The other contribution is the fluctuations of the velocity in the simulation domain. Thus, the total Reynolds shear stress is calculated by adding the contribution from the modelled turbulence part as well as the fluctuations of the velocity in the simulation domain as shown in equation 6.4. The different contributions to the Reynolds stress for the simulation with $\varepsilon_o = 0.71$ is shown in Figure 6.14.

$$\overline{\rho u_x' u_r'} = \overline{\mu_t\left(\frac{\partial u_x}{\partial r} + \frac{\partial u_r}{\partial x}\right)} + \overline{\rho(u_x - U_x)(u_r - U_r)} \tag{6.4}$$

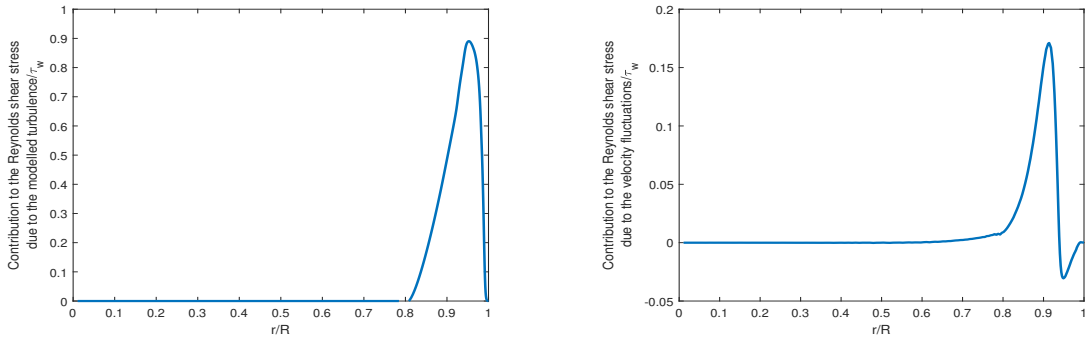

(a) (b)

Figure 6.14: Contribution to the Reynolds shear stress due to the (a) Modelled turbulence (b) Velocity fluctuations in the domain for the simulation with $\varepsilon_o = 0.71$.

The Reynolds shear stress is negligible in the oil core while in the warer region, it increases and reaches a maximum before going back to zero at the wall. The comparison for the total Reynolds shear stress between the 2D OpenFOAM simulations and the DNS data shows that the maximum for the 2D OpenFOAM simulations is higher than the maximum for the DNS curve. The local minimum of the viscous shear stress becomes higher with increasing oil holdup (decreasing turbulence) while the maximum of the total Reynolds shear stress becomes lower with increasing oil holdup. The comparison of the total shear stress is almost identical for $\varepsilon_o = 0.56$ as can be seen from Figure 6.16a. The curves for the case with $\varepsilon_o = 0.71$ and $\varepsilon_o = 0.83$ differ slightly in the water annulus part. Thus, it can be concluded that the turbulence level also impacts the comparison of the shear stress. The higher the turbulence inside the simulation domain, the better the comparison.

The comparison of the total shear stress obtained from the 2D OpenFOAM simulations and the force balance from equation 6.3 is shown in Figure 6.17. The total stress from equation 6.3 is calculated after neglecting the surface tension term and using the water volume fraction obtained from the 2D OpenFOAM simulations. The comparison shows that the curves are similar in the oil core while there is a slight difference near the interface. Since both the curves are obtained from the results of the 2D OpenFOAM simulations, it can be argued that this difference is due to the inaccuracy in the averaging done while calculating the total shear

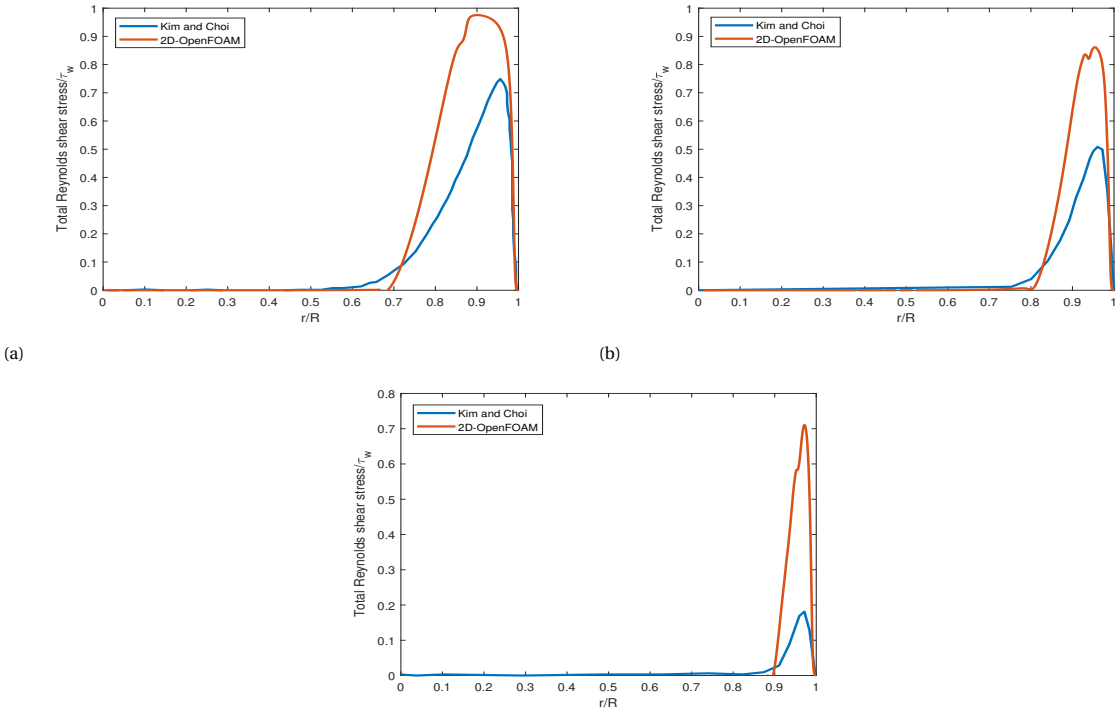

Figure 6.15: Comparison of the scaled Reynolds shear stress from the 2D OpenFOAM simulations with the DNS simulations of Kim and Choi [15] for (a) $\varepsilon_o = 0.56$ (b) $\varepsilon_o = 0.71$ (c) $\varepsilon_o = 0.83$.

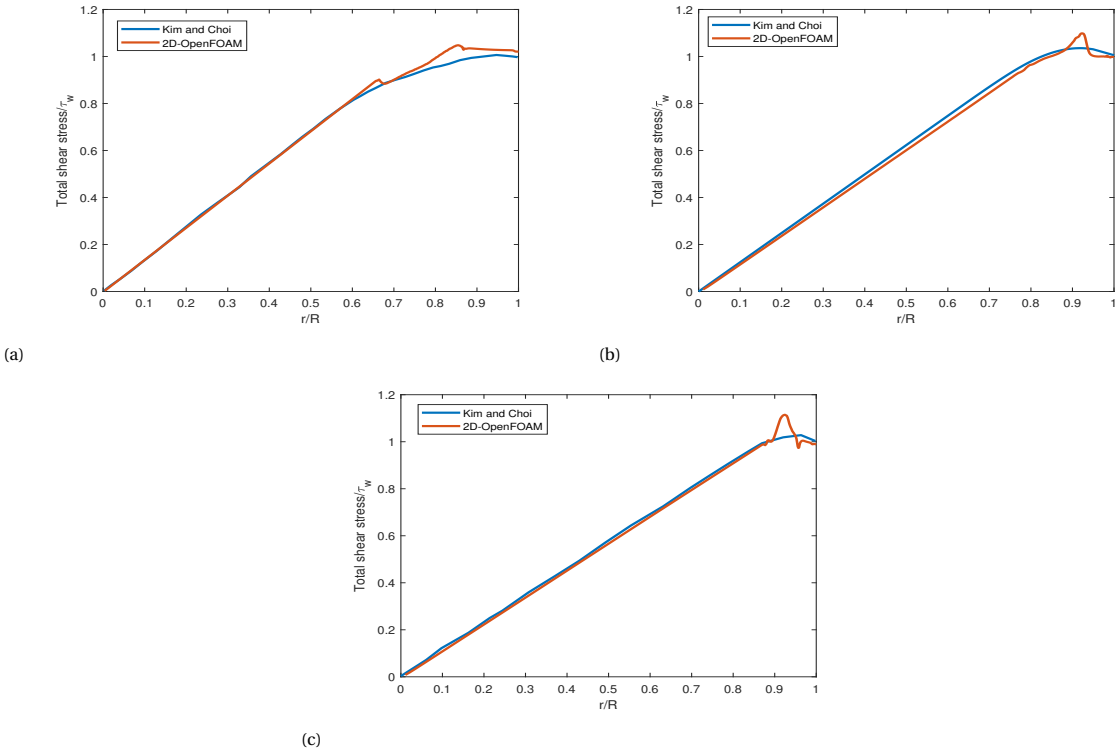

Figure 6.16: Comparison of the scaled total shear stress from the 2D OpenFOAM simulations with the DNS simulations of Kim and Choi [15] for (a) $\varepsilon_o = 0.56$ (b) $\varepsilon_o = 0.71$ (c) $\varepsilon_o = 0.83$.

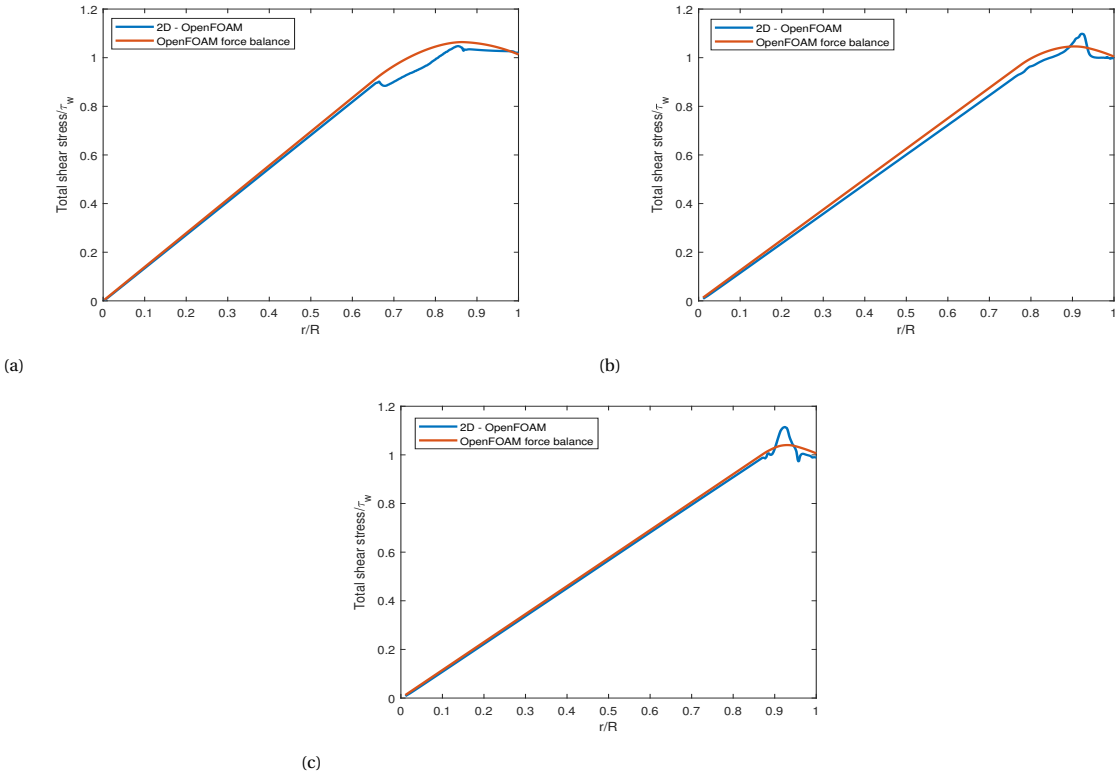

Figure 6.17: Comparison of total shear stress from the 2D OpenFOAM simulations and the OpenFOAM force balance from equation 6.3 for (a) $\varepsilon_o = 0.56$ (b) $\varepsilon_o = 0.71$ (c) $\varepsilon_o = 0.83$.

stress from equation 6.2.

The comparison between the scaled viscous, Reynolds and total shear stress for the simulations of different oil viscosities is shown in Figure 6.18. It can be seen that the viscous shear stress curves are identical for all the four cases. There is a slight difference in the Reynolds shear stress which can be attributed to the slightly different maximum turbulence viscosity ratio in the simulation domain as also shown in Table 5.7. Also, the averaging inaccuracy also plays a role here as was observed in the comparison of the total shear stress with the force balance for the 2D OpenFOAM simulations. The total shear stress is also identical in the region of the oil core while there is a slight difference in the water annulus. Thus, it can be concluded that in the range of high oil viscosities, there is no difference in the viscous shear stress when the oil viscosity is changed while there is a slight change in the Reynolds shear stress since the turbulence level changes slightly.

The comparison for the shear stresses between the 2D and 1D OpenFOAM simulations for the case with $\varepsilon_o = 0.71$ is shown in Figure 6.19. The curves for the viscous shear stress are identical except at and near the interface which can be attributed to the sudden jump in the volume fraction in the 1D simulations. There is a slight difference for the Reynolds shear stress. The total shear stress is identical in the oil core while there is a slight difference in the water annulus. Thus, it can be concluded that the turbulence is sufficiently resolved in the 1D simulations.

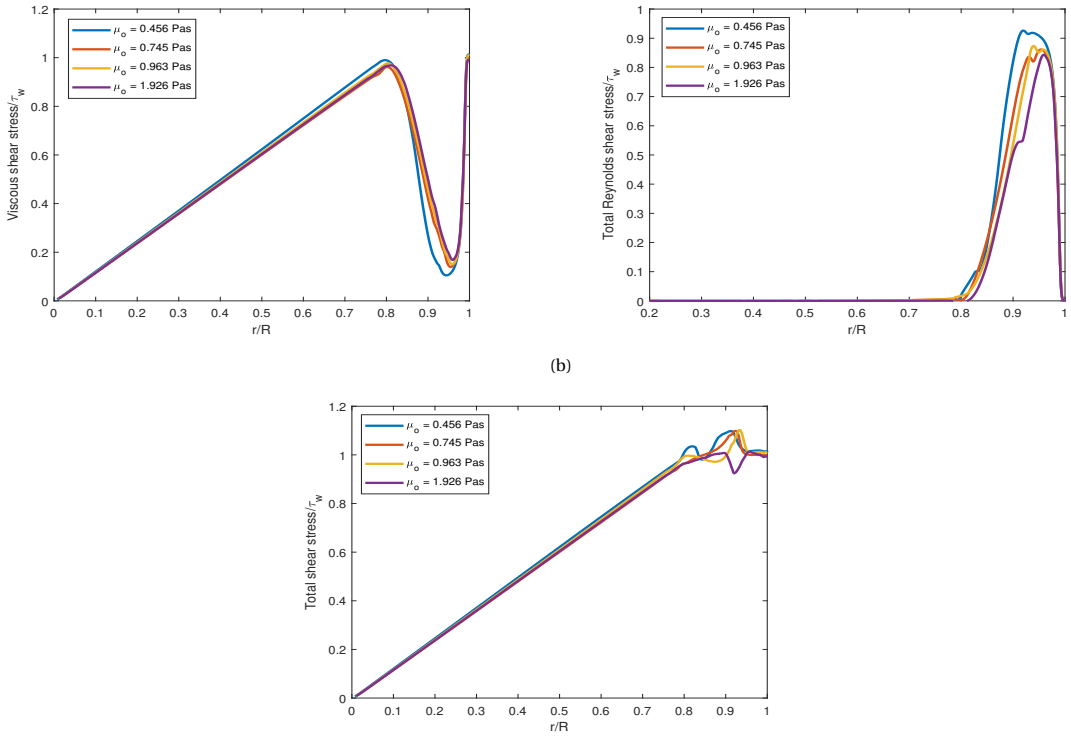

(a) (b)

(c)

Figure 6.18: Comparison of the scaled shear stresses for different oil viscosities (a) Viscous shear stress (b) Reynolds shear stress (c) Total shear stress.

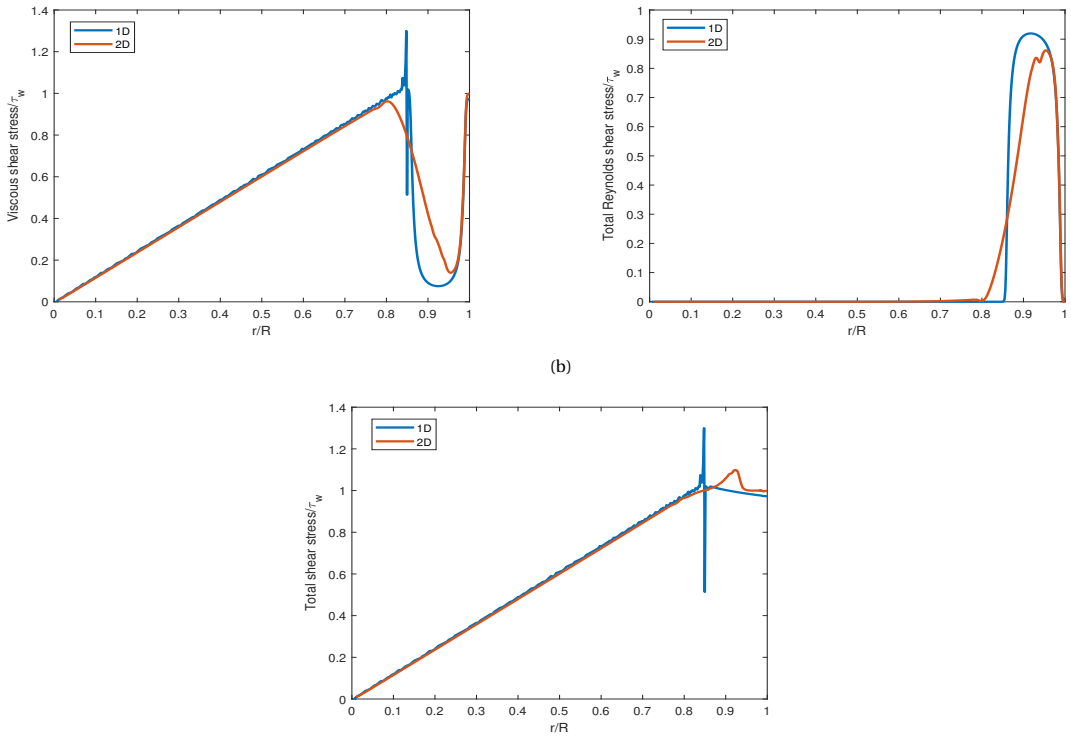

(a) (b)

(c)

Figure 6.19: Comparison of the scaled shear stresses for $\varepsilon_o = 0.71$ between 1D and 2D OpenFOAM simulations (a) Viscous shear stress (b) Reynolds shear stress (c) Total shear stress.

7

Conclusions and Recommendations

7.1. Conclusions

It has been observed that the simulations using Launder-Sharma low-Re k-ε model for core-annular flow of oil/water in a horizontal pipe provide results that have differences when compared with the experimental data. It is necessary to determine the impact of using the Launder-Sharma k-ε turbulence model, and in general the RANS approach, on the predictions of results for core-annular flow. This has been achieved in this thesis for vertical upward core-annular flow by comparing the results from the 1D and 2D OpenFOAM simulations using the Launder-Sharma low-Re k-ε turbulence model with the DNS results from Kim and Choi [15].

The CLSVOF method is used to track the interface in OpenFOAM because it combines the advantages of both the VOF and the LES method. Periodic boundary conditions are used to make the simulation domain shorter and reduce the computational time. The friction Reynolds number was fixed in this study and five cases of different oil holdups are compared. The input conditions were the imposed pressure drop and the oil holdup to use the advantage of periodic boundary conditions. The output gives the oil and water flow rates.

The 1D simulations for all the five cases as obtained with OpenFOAM are compared with the solutions for the same 1D model as calculated with MATLAB. The grid independence test is performed to validate the grids used in the 1D simulations. The agreement of the turbulence characteristics from the 1D OpenFAOM simulations and the 1D MATLAB model is excellent. The turbulence characteristics from the 1D OpenFOAM simulations for all five cases are compared with the asymptotic wall laws and excellent agreement was found for the region between $r^+ = 20$ and $r^+ = 100$, where the turbulence is expected to be present.

A base case is identified for the 2D simulations with an oil holdup fraction $\varepsilon_o = 0.71$ and it is used to validate the simulations by varying a single parameter and keeping the other parameters constant. The grid independence test is performed by varying the number of grid cells. Also, the comparison between the moving wall simulations and the stationary wall simulations is performed. It is concluded that the moving wall simulation with 200X100 grid gives a grid independent result and is the least computationally expensive. The dependence of the results on the streamwise domain length is analysed by varying the simulation domain length. It is observed that the domain length used for the base case (0.01656 m) gives results that do not depend on the streamwise domain length. The comparison between the simulations with and without gravity is also performed and it is concluded that for the fluid properties used in the simulations, the predictions do not change.

As fouling of the pipe wall was observed when the oil viscosity was used as the same in the DNS simulations, the oil viscosity used in this thesis is lower than the oil viscosity used in the DNS simulations. Thus, the simulations with different oil viscosities were analysed to understand the effect of the oil viscosity on the predictions. It is concluded that the flow rates do not change when the oil viscosity is changed but the wave characteristics and the turbulence inside the simulation domain varies slightly. Thus, the flow rates and the results obtained from the simulations with lower oil viscosity can be considered constant to compare it with the DNS results at higher oil viscosity. The turbulence characteristics for lower oil viscosity vary slightly with

change in oil viscosity and can also be used to compare with the DNS results at higher oil viscosity.

The comparison between the 2D OpenFOAM simulations and the DNS results is done for all the five cases presented by Kim and Choi [15]. It is observed that the differences between both the results depend on the turbulence levels inside the simulation domain. The difference in the total flow rate between the RANS predictions and the DNS data is about 10% for ε_o = 0.56, 0.62 and 0.71. The RANS friction factor is about 17% lower than the friction factor from the DNS data for the same three cases with oil holdup fraction of 0.56, 0.62 and 0.71. These simulations have significant turbulence levels and can be considered fully turbulent. The case with ε_o = 0.83 is observed to have lower turbulence levels and hence cannot be considered fully turbulent. The difference for the total flow rate increases to 16% for this case while the friction factor from the RANS simulation is 25% lower than the friction factor from the DNS results. The case with ε_o = 0.91 does not have any turbulence inside the domain and can be considered laminar. This case shows the difference to be 29% for the total flow rate and the friction factor from the RANS simulation is 39% lower than the friction factor from the DNS data. The difference for the holdup ratio (when comparing 2D OpenFOAM results with respect to DNS results) decreases first from 15% higher for ε_o = 0.56 to 8% higher for ε_o = 0.71 and then increases to 14% higher for ε_o = 0.91. The difference in the velocity predictions also follow the same trend of increasing with decreasing turbulence levels. The difference is less when significant turbulence levels are present in the simulation domain while the difference increases with the decrease in the turbulence levels. The difference in the turbulence characteristics also follow the same trend as observed for the difference in the flow characteristics. The comparison of the shear stresses is in agreement for the lower oil holdups while the difference increases as the oil holdup increases.

The comparison of the wave characteristics follows a different trend as compared to the flow characteristics. The wave characteristics have a good agreement for the case with ε_o = 0.91 while the agreement is worst for ε_o = 0.56. This can be attributed to the presence of a mixture of wavelengths in the DNS simulations at lower oil holdup which is seen from the broad peak of the probability distribution function for the radial location of the interface at low oil holdup. The 2D OpenFOAM simulations always have a sharper peak for the PDF and hence a dominant wavelength. Thus, it is concluded that the wave characteristics depends on the presence of a mixture of wavelengths. Hence, the comparison is accurate for the higher oil holdups while the difference increases as the oil holdup decreases.

Thus, it can be concluded that the flow rate predictions of the 2D OpenFOAM simulations are within 10% of the DNS results while the friction factor predictions are within 17% of the DNS results when the flow is fully turbulent. While the difference increases when the flow is transient or laminar. Still, care should be taken while using the comparison as the oil viscosity for the 2D OpenFOAM simulations and the DNS result is different. Hence, the objective of this thesis to determine the impact of using the Launder-Sharma low-Re k-ε turbulence model on the prediction of results for vertical core-annular flow configuration is achieved.

7.2. Recommendations

The first improvement that can be made to this thesis is to use a different numerical scheme to increase the oil viscosity to the value as used in the DNS results. This can be done by using a different interface tracking method or a different solver in OpenFOAM can be tried. The effect of eccentricity can be included by doing 3D RANS calculations and then comparing it with the DNS results for horizontal core-annular flow configuration.

To understand the flow physics and also to save computational time as compared to DNS, LES simulations can be performed. To understand the wave characteristics better, spectral analysis can also be performed. The parametric study for various properties like the surface tension, the water viscosity etc. can be performed to understand the influence of those parameters.

Appendices

A

Fouling in high oil viscosity simulation

The oil viscosity used in this thesis is lower than that used by Kim and Choi [15] because fouling was observed while simulating the flow with an oil viscosity of 17.6 Pa s. The waves continue to grow until the oil touches the pipe and fouling is observed. Once the oil touches the pipe, due to the no slip boundary condition, dispersion occurs and the simulation becomes very slow. The fouling inside the simulation domain can be seen in Figure A.1. Thus, it is not possible to continue the simulation and hence the oil viscosity was reduced to a value for which there was no fouling observed.

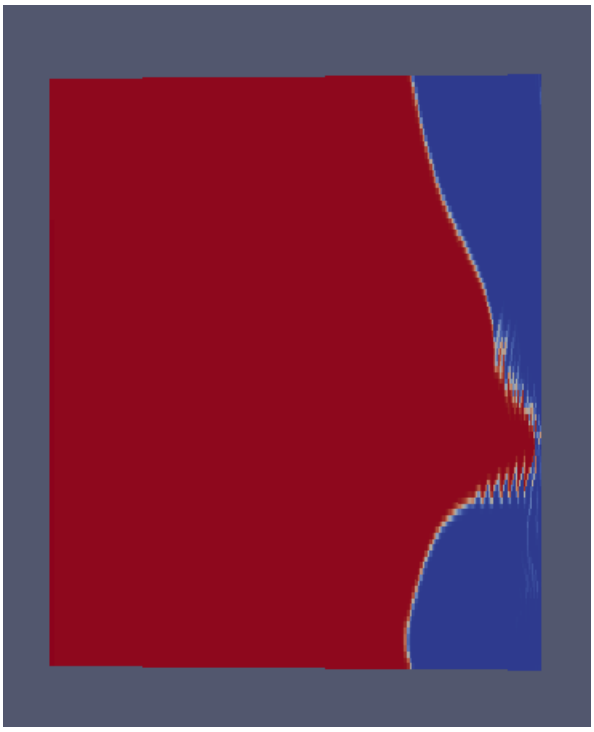

Figure A.1: Fouling of the pipe for the simulation with oil viscosity 17.6 Pa s.

Bibliography

[1] A. Albadawi, D. B. Donoghue, A. J. Robinson, D. B. Murray, and Y. M.C. Delauré. Influence of surface tension implementation in Volume of Fluid and coupled Volume of Fluid with Level Set methods for bubble growth and detachment. *International Journal of Multiphase Flow*, 53:11–28, july 2013.

[2] M.S. Arney, R. Bai, E. Guevara, D.D. Joseph, and K. Liu. Friction factor and holdup studies for lubricated pipelining-1. *International Journal Multiphase Flow*, 19(6):1061–1076, 1993.

[3] R Bai, K Chen, and D Joseph. Lubricated pipelining : stability of core-annular flow . Part 5 . Experiments and comparison with theory. *Journal of Fluid Mechanics*, 240:97–132, 1992.

[4] R. Bai, K. Kelkar, and D. Joseph. Direct simulation of interfacial waves in a high-viscosity-ratio and axisymmetric core-annular flow. *Journal of Fluid Mechanics*, 327:1–34, 1996.

[5] J Beerens. Lubricated transport of heavy oil. *Master Thesis, Delft University of Technology*, 2013.

[6] N. Brauner. Two-phase liquid-liquid annular flow. *International Journal of Multiphase Flow*, 17(1):59–76, 1991.

[7] S Deshpande, L Anumolu, and M Trujillo. Evaluating the performance of the two-phase flow solver interFoam. *Computational Science & Discovery*, 5:014016, 2012.

[8] S Ghosh, G Das, and P. K. Das. Simulation of core annular downflow through CFD-A comprehensive study. *Chemical Engineering and Processing: Process Intensification*, 49(11):1222–1228, 2010.

[9] R. A.W.M. Henkes. Scaling of the turbulent boundary layer along a flat plate according to different turbulence models. *International Journal of Heat and Fluid Flow*, 19(4):338–347, 1998.

[10] C. Hrenya, S. Miller, T. Mallo, and J. Sinclair. Comparison of low Reynolds number k-ϵ turbulence models in predicting heat transfer rates for pipe flow. *International Journal of Heat and Mass Transfer*, 41(11): 1543–1547, 1998.

[11] A. Huang, C. Christodoulou, and D. D. Joseph. Friction factor and holdup studies for lubricated pipelining-II . *International Journal of Multiphase Flow*, 20(3):481–491, 1994.

[12] W P Jones and B E Launder. The prediction of laminarization with a two-equation model of turbulence. *International Journal of Heat and Mass Transfer TA - TT -*, 15(2):301–314, 1972. ISSN 0017-9310.

[13] D Joseph, M Renardy, and Y Renardy. Instability of the flow of two immiscible liquids with different viscosities in a pipe. *Journal of Fluid Mechanics*, 141:309–317, 1984.

[14] D D Joseph, R Bai, and K P Chen. Core Annular Flows. *Annual Review of Fluid Mechanics*, 29:65–90, 1997.

[15] K. Kim and H. Choi. Direct numerical simulation of a turbulent core-annular flow with water-lubricated high viscosity oil in a vertical pipe. *Journal of Fluid Mechanics*, 849:419–447, 2018.

[16] T. Ko, H. G. Choi, R. Bai, and D. D. Joseph. Finite element method simulation of turbulent wavy core-annular flows using a k-ω turbulence model method. *International Journal of Multiphase Flow*, 28(7): 1205–1222, 2002.

[17] C. Kouris and J. Tsamopoulos. Core–annular flow in a periodically constricted circular tube. Part 1. Steady-state, linear stability and energy analysis. *Journal of Fluid Mechanics*, 432:31–68, 2001.

[18] Haoyu Li, M J B M Pourquie, G Ooms, and R A W M Henkes. Simulation of turbulent horizontal oil-water core-annular flow with a low-Reynolds number k – ε model. *International Journal of Multiphase Flow*, 142(May):103744, 2021.

[19] J. Li and Yuriko Renardy. Direct simulation of unsteady axisymmetric core–annular flow with high viscosity ratio. *Journal of Fluid Mechanics*, 391:123–149, 1999.

[20] R Martinuzzi and A Pollardt. Turbulent Pipe Flow Part I : Algebraic stress and $k-\varepsilon$ models. *American Institute of Aeronautics and Astronautics*, 27(1):29–36, 1989.

[21] A. Mathur and S. He. Performance and implementation of the Launder-Sharma low-Reynolds number turbulence model. *Computers and Fluids*, 79:134–139, 2013.

[22] R.V.A. Oliemans and Gijs Ooms. Core-annular flow of oil and water through a pipeline. *Multiphase Science and Technology*, 2:427–479, 1986.

[23] G Ooms, A Seoal, and A. van der Wees. A theoretical model for core-annular flow of a very viscous oil core and a water annulus through a horizontal pipe. *International Journal of Multiphase flow*, 10(I): 41–60, 1984.

[24] G Ooms, C Vuik, and P Poesio. Core-annular flow through a horizontal pipe : Hydrodynamic counterbalancing of buoyancy force on core. *Physics of Fluids*, 19:1–17, 2007.

[25] Jing Shi, Mustapha Gourma, and Hoi Yeung. CFD simulation of horizontal oil-water flow with matched density and medium viscosity ratio in different flow regimes. *Journal of Petroleum Science and Engineering*, 151:373–383, 2017.

[26] A. Ullmann and Brauner N. Closure relations for the shear stress in two-fluid models for core-annular flow. *Multiphase Science and Technology*, 16(4):355–387, 2004.

[27] J. Vanegas Prada and Antonio C Bannwart. Modeling of vertical core-annular flows and application to heavy oil production. *American Society of Mechanical Engineers*, 123, 2001.

[28] T. Yamamoto, Y. Okano, and S. Dost. Validation of the S-CLSVOF method with the density-scaled balanced continuum surface force model in multiphase systems coupled with thermocapillary flows. *International Journal for Numerical Methods in Fluids*, 83:223–244, 2017.

Nomenclature

$\frac{dP}{dx}$	Pressure gradient ($\mathrm{Pa\,m^{-1}}$)
μ_o	Oil viscosity (Pa s)
μ_t	Turbulent viscosity (Pa s)
μ_w	Water viscosity (Pa s)
ψ	Water volume fraction
ρ_o	Oil density ($\mathrm{kg\,m^{-3}}$)
ρ_w	Water density ($\mathrm{kg\,m^{-3}}$)
σ	Surface tension coefficient ($\mathrm{N\,m^{-1}}$)
τ_w	Wall shear stress (Pa)
ε	Turbulence dissipation rate ($\mathrm{m^2\,s^{-3}}$)
ε_o	Oil holdup fraction
k	Turbulent kinetic energy ($\mathrm{m^2\,s^{-2}}$)
L	Pipe length (m)
R	Pipe radius (m)
r	Radial coordinate (m)
u_τ	Friction velocity ($\mathrm{m\,s^{-1}}$)
V	Volume of the pipe ($\mathrm{m^3}$)
v_o	Superficial oil velocity ($\mathrm{m\,s^{-1}}$)
v_w	Superficial water velocity ($\mathrm{m\,s^{-1}}$)
x	Streamwise coordinate (m)